MASTERARBEIT | MASTER'S THESIS

Titel | Title

Spheroid co-culture model for human fibroblasts and triple-negative breast cancer cells

verfasst von | submitted by

Stella Neubauer BSc

angestrebter akademischer Grad | in partial fulfilment of the requirements for the degree of

Magistra pharmaciae (Mag. pharm.)

Wien | Vienna, 2026

Studienkennzahl lt. Studienblatt | Degree programme code as it appears on the student record sheet:	UA 066 605
Studienrichtung lt. Studienblatt | Degree programme as it appears on the student record sheet:	Masterstudium Pharmazie
Betreut von | Supervisor:	Univ.-Prof. Dipl.-Ing. Dr. Manfred Ogris
Mitbetreut von | Co-Supervisor:	Haider Sami Ph.D.

Acknowledgements

First, I would like to express my sincere gratitude to Prof. Dr. Manfred Ogris for the opportunity to carry out this thesis in the Laboratory of Macromolecular Cancer Therapeutics (MMCT).

I am especially grateful to my co-supervisor, Dr. Haider Sami, for his continuous support, constructive feedback and insightful discussions, that greatly contributed to the development of this work.

My special thanks go to Marlene Eder for her mentorship, hands-on guidance in the laboratory and continuous support throughout this project. I sincerely appreciate the trust she placed in me and the opportunity to be involved in her research.

I would also like to thank Elisa Kulterer and Christoph Kugler, as well as the other researchers in the lab for their support, helpful discussions and for contributing to a positive and enjoyable working environment.

I am also grateful to Susi Wiederkum for her technical support and willingness to help, which greatly facilitated the experimental work.

Another thanks goes to my fellow students Laura, Michi, Julija, Aki and Fabian, who shared the lab with me for half a year. Their support, collaboration and positive working atmosphere made these six months both productive (most of the time) and enjoyable (always). Beyond the lab, I particularly value the friendships that developed during this time and the many memorable moments we shared, both in and outside the lab.

I would also like to thank my friends for their understanding, support and patience, especially during times when I was less available. Their encouragement and continued presence have meant a great deal to me.

Finally, I would like to express my deepest gratitude to my parents, Scheyda and Gerhard, and my brother Sebi, for their unwavering support and for always being there for me, particularly during challenging and demanding times. I am also deeply grateful to my grandparents for their constant belief in me.

1 Abstract (English)

The development of *in vitro* models that accurately recapitulate the structural and functional characteristics of solid tumors remains a major challenge in cancer research. 3D spheroid models have emerged as a promising approach to better reflect tumor architecture and cellular interactions under physiologically more relevant conditions.

This study aimed to establish and characterize a multicellular spheroid culture model composed of human breast cancer cell line MDA-MB-231 genetically marked to express enhanced green fluorescent protein (eGFP) and human mammary fibroblasts (HMF3S cells) and to assess the impact of basement membrane matrix on these cultures. Seeding conditions were first optimized before spheroids were analyzed regarding growth, viability, necrotic core formation and morphology using metabolic activity assay, size measurements, live/dead staining and histological approaches. Immunohistochemistry (IHC) and flow cytometry were applied to assess marker expression (vimentin, alpha-smooth muscle actin, eGFP) to determine cellular composition.

Spheroid formation and stability were dependent on culture conditions as well as the culture ratio of the two cell lines. Matrix supplemented spheroids showed increased growth and exhibited greater variability. In contrast, cultures without matrix supplementation were more consistent concerning growth but displayed larger necrotic cores. IHC revealed limited specificity for the markers analyzed, while flow cytometry enabled the assessment of eGFP positive cancer cells but was influenced by potential microenvironmental effects on eGFP expression.

These findings provide a basis for the further development and optimization of 3D spheroid models that can be used to investigate tumor-stroma interactions.

2 Abstract (German)

Die Entwicklung von *in vitro* Modellen, die die strukturellen und funktionellen Eigenschaften solider Tumoren realitätsnah abbilden, stellt weiterhin eine große Herausforderung in der Krebsforschung dar. 3D Sphäroidmodelle haben sich als vielversprechender Ansatz etabliert, um die Tumorarchitektur und Zell-Zell-Interaktionen unter physiologisch relevanten Bedingungen besser zu reproduzieren.

Ziel dieser Arbeit war die Etablierung und Charakterisierung von multizellulären Sphäroidkulturen, bestehend aus der Brustkrebszelllinie MDA-MB-231, die genetisch zur Expression von Enhanced Green Fluorescent Protein (eGFP) markiert wurde, und humanen Brust-Fibroblasten (HMF3S Zellen), sowie die Untersuchung des Einflusses von Basalmembranmatrix auf die Kulturen. Zunächst wurden die Zellaussaat-Bedingungen optimiert, bevor die Sphäroide hinsichtlich ihres Wachstums, ihrer Viabilität, der Ausbildung eines nekrotischen Kerns und ihrer Morphologie mittels Assay zur Bestimmung der metabolischen Aktivität, Größenanalysen, Live/Dead-Färbungen sowie histologischer Verfahren untersucht wurden. Zur Analyse der Markerexpression (Vimentin, Alpha-Smooth-Muscle-Actin, eGFP) und zur Bestimmund der zellulären Zusammensetzung der Sphäroide wurden Immunhistochemie (IHC) und Durchflusszytometrie eingesetzt.

Die Bildung und Stabilität der Sphäroide waren sowohl von den Kulturbedingungen als auch vom Kultur-Verhältnis der beiden Zelllinien abhängig. Sphäroide kultiviert mit Matrix zeigten ein erhöhtes Wachstum und eine gesteigerte metabolische Aktivität, wiesen jedoch auch eine höhere Variabilität auf. Im Gegensatz dazu zeigten nicht supplementierte Kulturen ein einheitlicheres Wachstumsverhalten, wiesen jedoch größere nekrotische Kerne auf. Die IHC-Analysen zeigten eine eingeschränkte Spezifität der untersuchten Marker. Die Durchflusszytometrie ermöglichte hingegen die Analyse eGFP-positiver Krebszellen, war jedoch durch mögliche Effekte der Mikroumgebung auf die eGFP-Expression beeinflusst.

Die Ergebnisse dieser Arbeit bilden somit eine Grundlage für die Weiterentwicklung und Optimierung von 3D Sphäroidmodellen zur Untersuchung von Tumor-Stroma-Interaktionen.

Table of Contents

3 List of abbreviations

AB	antibody
AF647	Alexa Fluor™ 647
α-SMA	alpha smooth muscle actin
BMM	basement membrane matrix
CAA	cancer-associated fibroblast
CAF	cancer-associated adipocyte
CSC	cancer stem cell
DAPI	4’,6-Diamidino-2-phenylindole
DMEM	Dulbeccos’s modified eagle medium
ECM	extracellular matrix
EGF	epidermal growth factor
eGFP	enhanced green fluorescent protein
EMT	epithelial-mesenchymal transition
ER	estrogen receptor
EtOH	ethanol
FAP	fibroblast activation protein
FCS	fetal calf serum
FCM	flow cytometry
FGF	fibroblast growth factor
FITC	fluorescein isothiocyanate
FLM	fluorescence microscopy
FSC (A/H)	forward scatter (area/height)
H&E	hematoxylin and eosin
HER2	human epidermal growth factor receptor 2
HIF	hypoxia-inducible factor
HMF3S	human mammary fibroblast cell line
IGF	insulin-like growth factor
IHC	immunohistochemistry
IL	interleukin
MDA-MB-231	MD Anderson metastatic breast 231 cell line

MDSC	myeloid-derived suppressor cell
MHC	major histocompatibility complex
MMP	matrix metalloproteinase
OCT	optimal cutting temperature compound
PBS	phosphate-buffered saline
PDGFR	platelet-derived growth factor receptor
PFA	paraformaldehyde
PH	phase contrast
PI	propidium iodide
PR	progesterone receptor
SSC (A/H)	side scatter (area/height)
TAM	tumor-associated macrophage
TGF-β	transforming growth factor beta
TIL	tumor-infiltrating lymphocyte
TME	tumor microenvironment
TNBC	triple-negative breast cancer
VEGF	vascular endothelial growth factor

4 Introduction

Cancer is a heterogenous group of diseases characterized by uncontrolled cell proliferation and the ability of malignant cells to invade surrounding tissues and disseminate to distant sites. Despite considerable advances in diagnosis and treatment, cancer remains a major global health challenge.[1,2]

To describe the biological complexity of cancer, Hanahan and Weinberg introduced the paradigm of the “hallmarks of cancer”, which define key functional abilities acquired during tumor development. These include, among others, sustained proliferative signaling, resistance to cell death and the activation of invasion and metastasis. In addition, tumors dynamically interact with their surrounding microenvironment, which further contributes to disease progression. Together these hallmarks provide a conceptual framework for understanding tumor growth and metastatic dissemination.[3,4]

4.1 Breast cancer

Among all cancer types, breast cancer is one of the most frequently diagnosed malignancies worldwide and represents the leading cause of cancer-related mortality among women.[5] In 2022, approximately 2.3 million women were diagnosed and 670,000 deaths were attributed to breast cancer, highlighting its substantial clinical impact.[6] While increasing incidence rates are partly driven by demographic changes, longer life expectancy and lifestyle factors, disease progression and patient outcome are largely determined by the dissemination of tumor cells to distant organs. This metastatic spread remains the primary cause of breast cancer-related mortality.[5,7]

4.1.1 Subtypes of breast cancer

Based on the expression of the estrogen receptor (ER), progesterone receptor (PR), human epidermal growth factor receptor 2 (HER2) and the proliferation marker Ki-67, breast cancer comprises several molecular subtypes with distinct biological and clinical characteristics.

4.1.1.1 Luminal A and luminal B breast cancer

Luminal A tumors are defined by hormone receptor positivity (ER and/or PR), HER2 negativity and low proliferative activity (Ki-67 low). They represent the most common subtype and are associated with a favorable prognosis and strong responsiveness to endocrine therapy. In contrast, although also hormone receptor-positive, luminal B tumors display higher

proliferation rates, increased aggressiveness and poorer clinical outcomes. Furthermore, they show increased expression levels of growth receptor signaling genes and may either be HER2-positive or HER2-negative.[8-10]

4.1.1.2 HER2-positive breast cancer

HER2-positive breast cancers are characterized by amplification of the HER2 oncogene, absence of ER or PR expression and exhibit a highly proliferative and aggressive phenotype. Despite their poor prognosis, the introduction of HER2-targeted therapies (such as the monoclonal antibody trastuzumab) has significantly improved patient outcomes.[6,8]

4.1.1.3 Triple-negative breast cancer

Triple-negative breast cancer (TNBC), defined by the absence of ER, PR and HER2 expression, accounts for approximately 15-20 % of cases and represents the most aggressive subtype. It is associated with rapid progression, early metastasis and limited therapeutic options, as targeted endocrine and HER2-directed treatments are not applicable. Consequently, chemotherapy often remains the main treatment option.[8,11,12]

Importantly, TNBC tumors are characterized by cellular plasticity, high intratumoral heterogeneity and interactions with the tumor microenvironment (TME), which critically contribute to tumor progression and therapy resistance.[13-15]

4.1.1.3.1 MDA-MB-231

The MDA-MB-231 cell line, originally derived from the MD Anderson series, is a widely used *in vitro* model for TNBC. It lacks expression of ER, PR and HER2 and is classified as a claudin-low subtype, characterized by reduced cell-cell adhesion.[16] MDA-MB-231 cells exhibit epithelial-mesenchymal transition (EMT) features which are reflected by the loss of E-cadherin and increased expression of mesenchymal markers such as N-cadherin.[16-18] In 3D culture models, these features are further enhanced, with cells forming loosely cohesive, stellate or grape-like structures, which indicates an invasive growth pattern. Additionally, the formation of hypoxic and nutrient gradients in 3D models is thought to promote metastatic behavior and may contribute to increased resistance to chemotherapeutic agents such as doxorubicin or carboplatin.[16,19] In line with their aggressive phenotype, MDA-MB-231 cells secrete pro-inflammatory cytokines and factors, including IL-6, IL-8 and VEGF, which mediate interactions with the TME and promote angiogenesis.[20,21]

Collectively, these characteristics highlight the suitability of MDA-MB-231 cells as a TNBC model to investigate tumor behavior and microenvironmental interactions, particularly in 3D

culture systems.

4.2 Tumor microenvironment in breast cancer

The tumor microenvironment (TME) is a complex and dynamic ecosystem which surrounds and interacts closely with tumor cells. Rather than serving as a passive scaffold, it consists of a heterogenous network of non-malignant stromal cells, immune cells, extracellular matrix (ECM) components and soluble factors such as chemokines, cytokines and growth factors. The bidirectional crosstalk between tumor cells and the TME actively contributes to cancer progression, influencing processes such as angiogenesis, metastasis and therapy resistance. Within breast TME, several cell populations play important roles in orchestrating these processes.[22,23]

4.2.1 Fibroblasts

Among the stromal components of the breast TME, cancer-associated fibroblasts (CAFs) represent a major non-hematopoietic cell population. These activated, myofibroblast-like cells contribute to tumor progression by remodeling the ECM and secreting a variety of soluble factors. Through these functions, CAFs influence processes such as tumor cell invasion, EMT and immune modulation.[24] Given their multifaceted roles within the TME and their relevance to this work, CAFs will be discussed in more detail in section 4.3.

4.2.2 Extracellular matrix

The ECM is a non-cellular, macromolecular network that provides both structural support and biochemical signaling cues within the TME. It is primarily composed of fibrous proteins such as collagens, laminin and fibronectin, as well as glycoproteins, proteoglycans and polysaccharides including hyaluronan.[14,23,25]

In breast cancer, the ECM undergoes continuous remodeling, largely driven by stromal cells such as CAFs, leading to increased matrix protein deposition and cross-linking. This results in enhanced tissue stiffness, which in turn activates mechanotransduction pathways in tumor cells and promotes their invasive and migratory behavior. Increased ECM stiffness is commonly associated with a more aggressive tumor phenotype.[14,23,26]

4.2.3 Immune cells

The immune cell compartment within the TME is highly heterogenous and exhibits a dual role, with the capacity to either suppress or promote tumor progression. Cells of both the

innate and adaptive immune system are present, of which selected key populations are highlighted below.[23]

The innate immune system is largely dominated by myeloid cells, especially tumor-associated macrophages (TAMs). Although macrophages can theoretically eliminate cancer cells, they are frequently polarized into an M2-like phenotype within the breast TME. These M2-like TAMs are associated with the promotion of angiogenesis and metastatic dissemination, and contribute to immune suppression together with myeloid-derived suppressor cells (MDSCs). Consistently, increased infiltration of M2-like TAMs is linked to poor clinical outcomes and reduced treatment efficacy, with particularly elevated levels observed in TNBC compared to other subtypes.[23,27,28]

Components of the adaptive immune system, especially tumor-infiltrating lymphocytes (TILs) such as CD8+ cytotoxic T-cells, CD4+ helper T-cells or B-cells, can recognize and eliminate tumor cells and are often associated with a favorable clinical outcome. In line with this, a high infiltration with TILs has been correlated with improved responses to neoadjuvant chemotherapy. However, the TME can impair their function through the recruitment of immunosuppressive populations, including regulatory T-cells (Tregs). These cells secrete cytokines like IL-10 and TGF-β which inhibit anti-tumor activities. Consequently, high levels of Treg infiltration may be associated with poor clinical outcomes.[23,29,30]

4.2.4 Endothelial cells

In addition to immune and stromal components, endothelial cells play a central role in shaping the TME through their involvement in tumor angiogenesis. This process is essential to meet the increased metabolic, oxygen and nutrient demands of a growing tumor mass. Under hypoxic conditions, tumor cells and components of the TME stimulate the formation of new blood vessels from the existing vasculature, mediated by factors such as hypoxia-inducible factors (HIFs), VEGF and angiopoietins.[31]

However, tumor-associated vascularization is typically structurally and functionally abnormal. The newly formed vessels are characterized by excessive branching, poor pericyte coverage and increased permeability, contributing to the development of an acidic microenvironment, partly driven by HIF-mediated metabolic reprogramming, which can further promote tumor progression. In addition, the compromised integrity of these “leaky” vessels facilitates tumor cell intravasation into the bloodstream, thereby enabling metastatic dissemination to distant organs.[14,32,33]

4.2.5 Adipocytes

Adipocytes represent a specialized component of the breast TME, reflecting the fat-rich composition of the mammary gland. In response to tumor-derived signals, adipocytes can undergo transition into cancer-associated adipocytes (CAAs), which are characterized by increased lipolytic activity and a dysfunctional phenotype.[22,34]

CAAs secrete a range of factors, including hormones, adipokines such as leptin, free fatty acids and cytokines like IL-6. These factors contribute to tumor progression by supporting the metabolic demands of cancer cells, promoting cancer stem cell properties and enhancing invasive behavior.[22,34,35]

4.3 Cancer-associated fibroblasts

As briefly introduced in section 4.2.1, CAFs represent the most abundant mesenchymal cell population within the TME of breast cancer. They are typically defined as elongated cells that lack epithelial, endothelial and leukocyte markers. Rather than serving solely structural roles, CAFs actively shape the TME through dynamic interactions with tumor cells and other stromal components, thereby promoting tumor progression, metastasis and therapy resistance.[36-38]

4.3.1 Phenotypic and functional characteristics of CAFs

In contrast to normal fibroblasts, which maintain tissue homeostasis and are only transiently activated during wound healing, CAFs exhibit a constitutively activated phenotype. This is reflected by enhanced contractility and migratory capacity, as well as overexpression of markers such as α-smooth muscle actin (α-SMA), fibroblast activation protein (FAP) and platelet-derived growth factor receptor (PDGFR). However, expression of these markers is not exclusive to CAFs, as they may also be expressed by normal fibroblasts. Functionally, CAFs acquire a pro-tumorigenic role characterized by extensive ECM remodeling via matrix metalloproteinases (MMPs) and the secretion of cytokines and growth factors, including TGF-β, IL-6 and VEGF. Through these mechanisms, CAFs promote invasion, angiogenesis, metabolic reprogramming and immunosuppression within the TME.[24,25,36,39]

4.3.2 CAF heterogeneity

In the context of breast cancer, up to 80 % of resident fibroblasts acquire the activated CAF phenotype during disease progression. However, rather than representing a uniform cell

population, CAFs display pronounced heterogeneity, arising from diverse cellular origins, including mesenchymal stem cells, resident fibroblasts and adipocytes. Various attempts have been made to classify CAFs into different subtypes. One widely used distinction is between myofibroblastic (myCAFs), inflammatory (iCAFs) and antigen-presenting (apCAFs) CAFs. MyCAFs exhibit high contractility and are primarily involved in ECM organization, whereas iCAFs release many immunomodulatory molecules. In addition, apCAFs, characterized by the expression of MHC class II molecules, have been linked to the modulation of adaptive immune responses.[36,40-42]

Taken together, the complex and dynamic roles of CAFs in the TME highlight the need for experimental models that can accurately mimic tumor-stroma interactions.

4.3.3 HMF3S

The HMF3S cell line is a human fibroblast model derived from healthy mammary tissue which can be used to study stromal biology and TME-interactions.[43,44] In co-culture systems, HMF3S cells actively interact with breast cancer cells which promotes tumor cell invasion. In 3D co-culture models, HMF3S cells have been observed to adopt a more elongated morphology in response to tumor-derived signals. Furthermore, they exhibited secretion of various cytokines and matrix-remodeling factors, such as IL-6, IL-8, the metastasis-associated protein S100A4 or matrix metalloproteinase 2 (MMP-2), which facilitate ECM-remodeling and paracrine signaling within the TME.[44] Under certain stimuli, such as exposure to TGF-β1, HMF3S cells can acquire CAF-like characteristics, associated with the upregulation of markers including α-SMA, FAP and PDGFRβ.[45]

Overall, HMF3S cells represent a valuable tool to study fibroblast-mediated modulation of tumor behavior *in vitro*.

4.4 2D versus 3D models to study breast cancer

4.4.1 2D cell culture models

2D cell culture represents the traditional *in vitro* model for investigating cell biology, disease mechanisms and pharmacological responses. In this system, cells are cultured as a monolayer on rigid, flat surfaces such as plates or culture flasks, providing equal access to nutrients, oxygen or signaling molecules.[46,47] In breast cancer research, 2D cultures have long served as the standard preclinical method for applications including cytotoxicity testing, target validation and drug screening for novel anticancer therapeutics. A wide range

of established breast cancer cell lines is routinely used to reflect different molecular subtypes, including MDA-MB-231 to represent TNBCs.[48,49]

Despite their widespread use, 2D cell culture models present both advantages and limitations. Their simplicity, cost-effectiveness and high reproducibility make them highly accessible experimental systems. In addition, well-established protocols and compatibility with high-throughput screening enable rapid evaluation of drug candidates and functional assays. Cells cultured in 2D typically exhibit fast proliferation rates, which further facilitates efficient workflows.[46,47]

However, reliance on 2D models presents significant limitations. 2D systems fail to recapitulate the 3D architecture of solid tumors, resulting in altered cell morphology, disrupted polarity and a lack of critical cell-cell and cell-ECM interactions. Moreover, equal exposure to nutrients, oxygen and signaling molecules prevents the formation of physiologically relevant gradients.[46,50] Consequently, cells grown in 2D display altered gene expression and cellular behavior, which limits the predictive value of these models. In particular, drug responses may be misinterpreted, as 2D cultures tend to overestimate therapeutic efficacy and fail to capture key mechanisms of resistance observed *in vivo*.[51,52]

4.4.2 3D cell culture models

3D cell culture models have emerged as essential preclinical tools in cancer research, bridging the gap between highly simplified 2D monolayer cultures and complex *in vivo* models. By more accurately mimicking the spatial organization of tissues, 3D cultures restore crucial cell-cell and cell-ECM interactions, thereby influencing cellular morphology, behavior and also drug response.[53]

3D culture systems can be broadly classified into scaffold-based and scaffold-free approaches. Scaffold-based models utilize natural or synthetic matrices to provide structural support and mimic the ECM. Natural scaffolds include hydrogels such as collagen, or Matrigel®, whereas synthetic scaffolds are often represented by polycaprolactone (PCL), polyethylene glycol (PEG) or polylactic acid (PA). Scaffold-free systems, on the other hand, rely on the intrinsic ability of cells to self-organize into multicellular aggregates.[50,52]

Among scaffold-free approaches, multicellular tumor spheroids have become one of the most widely used and biologically relevant models in cancer research, particularly due to their ability to recapitulate key features of solid tumors *in vivo*, especially interactions within the TME.[52]

4.4.3 Tumor spheroids as a 3D cell culture model

Tumor spheroids are self-assembled, 3D multicellular aggregates that form in the absence of an external adherent substrate. Under these conditions, cells establish extensive cell-cell and cell-ECM interactions, primarily mediated by adhesion molecules such as cadherins and integrins. In contrast to 2D cultures, cells within spheroids can produce and deposit their own ECM components, including collagen, laminin and fibronectin. Thereby a more physiologically relevant microenvironment is created.[52,54]

The combination of tight cellular junctions and ECM deposition results in a dense structural network that limits the diffusion of oxygen, nutrients and metabolites. Consequently, spheroids develop distinct concentric zones that recreate key features of avascular tumors. These zones include an outer proliferative layer of actively dividing cells, an intermediate quiescent zone and an inner hypoxic and therefore necrotic core characterized by oxygen deprivation and acidic pH.[51,54]

Ultimately, spheroids mimic essential aspects of the TME through the restoration of the cell-cell and cell-ECM crosstalk within this 3D context. In breast cancer research, spheroids derived from different cell lines can further exhibit distinct morphological phenotypes (round, mass, stellate and grape-like), reflecting differences in cell-cell adhesion and invasive behavior.[51]

4.4.3.1 Generation of spheroids

Tumor spheroids are generated by promoting cell-cell and cell-ECM interactions while preventing cell attachment to a solid substrate. This can be achieved using scaffold-free culture techniques that keep cells in suspension and thereby facilitate their self-assembly into aggregates. Commonly used methods include the hanging drop technique, in which cells aggregate at the apex of a droplet due to gravity and ultra-low attachment systems, where cells are cultured in non-adherent plates that prevent surface attachment (also referred to as the liquid overlay technique). Additional approaches, such as dynamic suspension or pellet cultures, can further support spheroid formation by enhancing cell-cell contact through either continuous movement or centrifugation.[53,55]

4.4.3.2 Types of spheroids in breast cancer research

Several types of spheroid models are commonly used in breast cancer research, each addressing different biological questions.

Homotypic monoculture spheroids are formed from a single cancer cell type. Depending on

the cell line and method used for their generation, they can either form dense spheroids (e.g. T-47D using ultra-low attachment plates) or loose aggregates (e.g. MDA-MB-231 using ultra-low attachment plates). They are frequently applied for high-throughput drug screening approaches.[48,49]

In contrast, heterotypic or co-culture spheroids incorporate additional stromal cell types, such as CAFs, endothelial cells or immune cells, to better mimic the complexity of the TME. These models are especially interesting for studying mechanisms like epithelial-to-mesenchymal transition (EMT), drug resistance, tumor invasion and metastasis. By integrating multiple cellular compartments, co-culture spheroids provide a more physiologically relevant platform to study interactions of the tumor with its microenvironment and their impact on cancer behavior.[49,52]

A more specialized model is represented by tumorospheres, which in the context of breast cancer are referred to as mammospheres. They are generated under specific non-adherent conditions to enrich for cancer stem cells (CSCs) and are usually used to investigate stemness, self-renewal capacity and tumorigenic potential.[56,57]

4.4.3.3 Advantages and limitations of spheroid models

Taken together, tumor spheroid models offer several key advantages compared to conventional 2D cultures. Their 3D architecture promotes structural heterogeneity and the formation of physiological gradients, thereby more closely resembling *in vivo* tumor conditions and influencing cellular behavior.[52] Additionally, spheroids provide a more predictive platform for studying drug responses, as they enable the investigation of clinically relevant resistance mechanisms that are not adequately captured in 2D models.[58] Compared to other 3D systems (e.g. organoids), spheroids are relatively simple to generate, cost-effective and compatible with scalable and high-throughput experiments. Moreover, scaffold-free spheroid models have reduced variability associated with exogenous matrices.[47,49,55]

Despite these advantages, tumor spheroid models also present several limitations. From a biological perspective, spheroids often lack important systemic components of native tumors, such as vascularization, which restricts their applicability for studying complex *in vivo* processes. In addition, excessive spheroid growth can lead to the formation of large necrotic cores, which may influence experimental read-outs.[51,52,59] Furthermore, spheroid models pose experimental and analytical challenges. Variability in spheroid size and diameter can affect reproducibility, particularly in quantitative assays. Their dense 3D

structure may also limit imaging depth and complicate downstream analyses, often requiring disruptive processing steps (e.g. when using flow cytometry) that result in the loss of spatial information.[52,55,60]

5 Aim of this study

Understanding the complex interactions within the TME requires *in vitro* models that more closely mimic the structural and functional characteristics of tumors *in vivo*. While conventional 2D culture systems are limited in their ability to reflect spatial organization and cellular interactions, 3D spheroid models provide a more physiologically relevant platform to study tumor architecture and pathophysiology.

The overall aim of this study was to establish and characterize mono- and mulitcellular spheroid models composed of MDA-MB-231 and HMF3S cells. For this purpose, seeding conditions were optimized to enable the reproducible formation of stable spheroids or cell aggregates across different culture settings. In addition, matrix supplemented and un-supplemented conditions were compared to assess their impact on spheroid formation, growth behavior and cellular characteristics. Subsequent analyses focused on the assessment of spheroid growth and viability using a metabolic activity assay and size-based measurements. Furthermore, the development of necrotic cores as a key feature of tumor-like structures was evaluated by live/dead staining.

To further characterize structural and functional properties, spheroids or cell aggregates were subjected to histological and immunohistochemical analyses to assess overall morphology and marker expression. Finally, flow cytometry-based methods were employed to quantify the cellular composition and distribution within co-culture spheroids.

6 Materials

6.1 General laboratory materials

Table 1. General laboratory materials

Material	Supplier	Reference Number
15 mL tubes (CT-15)	Sarstedt	Ref: 62.554.502
50 mL tubes	Sarstedt	Ref: 62.548.004
Micro tubes 0.5 mL SafeSeal	Sarstedt	Ref: 72.704.400
Microcentrifuge tube PP, 1.5 mL	Nerbe Plus GmbH	Ref: 04-212-3000
Micro tubes 2.0 mL SafeSeal	Sarstedt	Ref: 72.695.400
T25 flask	Sarstedt	Ref: 83.3911.002
Serological pipettes 5 mL	Sarstedt	Ref: 86.1253.001
Serological pipettes 10 mL	Sarstedt	Ref: 86.1254.001
Serological pipettes 25 mL	Sarstedt	Ref: 86.1685.001
Pipetboy	Integra	Ref: 155022
Pipette tips 10 µL	Greiner Bio-One GmbH	Ref: 771351
Pipette tips 200 µL	Greiner Bio-One GmbH	Ref: 775351
Pipette tips 1000 µL	Greiner Bio-One GmbH	Ref: 777351
Pipettes (2.5, 10, 200, 1000 µL)	Eppendorf/Starlab	
ultra-low attachment 96-well plate, surface: BIOFLOAT™, round base	Sarstedt	Ref: 83.3925.400
Nunclon™ Delta Surface, flat-bottom 96-well plate	Thermo Fisher Scientific™	Ref: 167008
Syringe Inject® Luer Solo 10 mL	Henke Sass Wolf	Ref: 4606108V
Syringe filter, Filtropur S PES, pore size: 0.2 µL	Sarstedt	Ref: 83.1826.001

Disposable base molds	Electron Microscopy Sciences	Ref: 62352-07
Tissue-Tek® O.C.T. Compound	Sakura	Ref: 4583
Superfrost™ Plus Adhesion Microscope Slides	Thermo Fisher Scientific	Ref: 11959657
Cover Slips, 24 x 50 mm #1	Thermo Fisher Scientific	Ref: 12-518-105EP
PAP Pen	Sigma-Aldrich	Ref: Z377821

6.2 Cell lines

Table 2. Cell lines

Cell line	**Supplier**
HMF3S	Professor Mike O'Hare (Ludwig Institut)
MDA-MB-231	ATCC (HTB-26)
MDA-MB-231 PGK eGFP Luc	Modified acc. to Billerhart et al.[61]

6.3 Medium

Table 3. Medium

Material	**Supplier**	**Reference/LOT-Number**
Dulbecco's Modified Eagle's Medium (DMEM) - high glucose	Sigma-Aldrich	Ref: D5671 LOT: RNBN1156

6.4 Powders and liquids

Table 4. Powders and liquids

Material	Supplier	Reference/LOT-Number
TrypLE™ express enzyme without phenol red	Gibco	Ref: 12604021
Dulbecco's Phosphate Buffered Saline (PBS)	Sigma-Aldrich	Ref: D8537
Fetal Calf Serum (FCS), heat inactivated	BioWest	Ref: S181H-500,
L-Glutamine solution, 200 mM	Sigma-Aldrich	Ref: G7513
Penicillin-Streptomycin	Sigma-Aldrich	Ref: P0781
4 % PFA in HBS buffer pH 7.4	BioChemica	Ref: A3813 LOT: 7E011523
Sucrose	Sigma-Aldrich	Ref: 83100-250G
Resazurin, sodium salt, pure	Thermo Fisher Scientific™	Ref: 418900050 LOT: A0464132
Basement Membrane Matrix (BMM), growth factor reduced (GFR)	MedChemExpress	Ref: HY-K6004 LOT: 659197
bis-Benzimide H-33342 trihydrochloride trihydrate, 98 % (Hoechst)	Thermo Fisher Scientific™	Ref: J62134 LOT: U12G033
Propidium iodide (PI) solution	Sigma-Aldrich	Ref: P4864 LOT: SHBP1046
DAPI	Sigma-Aldrich	Ref: D9542 LOT: 0000157172
SmartBlock™ blocking buffer	Candor Bioscience GmbH	Ref: 113 500 LOT: 113E040г
Hematoxylin solution acc. to Harris	Carl Roth GmbH + Co. KG	Ref: X903.2 LOT: 344360081

Eosin Y solution	Sigma-Aldrich	Ref: 318906 LOT: MKCL4995
Ammonium hydroxide solution	Sigma-Aldrich	Ref: 221228-25ML-A LOT: SZBD3180V
Vectashield ® Plus Antifade Mounting Medium	Vector Laboratories, Inc.	Ref: H-1900 LOT: ZK1017
Entellan™ new, rapid mounting medium for microscopy	Sigma-Aldrich	Ref: 1.07961.0500 LOT: HX90832861
CellTrace™ CFSE cell proliferation Kit	Thermo Fisher Scientific™	Ref: C34570 LOT: 2528095

6.5 Antibodies

Table 5. Antibodies

Antibody	**Supplier**	**Reference/LOT-Number**
Rabbit IgG Iso-Antibody, 5 mg/mL	Thermo Fisher Scientific	Ref: 02-6102 LOT: XK366556
Ki-67 Recombinant Rabbit Monoclonal Antibody, 0.031 mg/mL	Thermo Fisher Scientific™	Ref: MA-5-14520 LOT: ZG4360031
Vimentin Rabbit Polyclonal Antibody, 0.5 mg/mL	Proteintech	Ref: 10366-1-AP LOT: 00132436
Alpha smooth muscle actin Rabbit Polyclonal Antibody, 0.75 mg/mL	Proteintech	Ref: 14395-1-AP LOT: 00170559
Nano-Secondary ® anti-rabbit IgG, AF647, 0.5 g/L	Proteintech	Ref: SrbAF647-01 LOT: 110082-01

6.6 Devices

Table 6. Devices

Device	Supplier	Specification
Waterbath	Memmert	WNB29
Centrifuge	Thermo Fisher Scientific™	Heraeus Megafuge 16R Centrifuge
Centrifuge	Starlab	Mini fuge plus
Microscope	Olympus	IX73
Microscope	Olympus	BX53F
Sterile Hood	Thermo Fisher Scientific™	HerasafeTM KS (NSF) Class II, Type A2 Biological Safety Cabinet
Incubator	Thermo Fisher Scientific™	HeracellTM 150i CO2 Incubator
Vortex	Starlab	Serial number: VB201AL0000198
Scale	Kern	ABP 100-5DM
Plate Reader	Tecan	Infinite 200Pro
Counting Chamber	Marienfeld Brand GmbH	0.0025mm2, 0.1mm depth
Cryostat	SLEE medical GmbH	Type MNT
MACSQuant®	Miltenyi Biotec	

6.7 Software

Table 7. Software

Software	Usage
cellSens 2.2, Olympus	Phase contrast (PH) / Fluorescence microscopy (FLM)
cellSens, Olympus	Haematoxylin/Eosin (H/E) imaging
ImageJ	Size analysis of spheroids

7 Methods

7.1 Preparation of solutions

DMEM - high glucose medium complete (10 % FCS, 1 % L-Gln, 1 % P/S)

- 450 mL DMEM – high glucose medium
- 50 mL Fetal Calf Serum (FCS)
- 5 mL L-Glutamine (L-Gln)
- 5 mL Penicillin/Streptomycin (P/S)

DMEM - high glucose medium complete with Basement Membrane Matrix (BMM)

- DMEM – high glucose medium complete with 8 % BMM
    - 9.2 mL DMEM high glucose medium complete
    - 0.8 mL BMM (v/v)
- DMEM – high glucose medium complete with 2 % BMM
    - 1.25 mL DMEM – high glucose medium complete with 8 % BMM
    - 3.75 mL DMEM high glucose medium complete

Resazurin 0.1 mg/mL

- Resazurin 1 mg/mL
    - 5 mg Resazurin powder
    - 5 mL PBS
- Resazurin 0.1 mg/mL
    - 0.5 mL Resazurin 1 mg/mL
    - 4.5 mL PBS

The prepared solution was aliquoted into 200 µL stocks and stored in the freezer at -20 °C. The same batch was used for the entire duration of each experiment in which a metabolic activity assay was performed.

Hoechst 320 µg/mL

- 16 µL Hoechst 10 mg/mL stock solution
- 484 µL PBS

Propidium Iodide (PI)

- PI 250 µg/mL (1:4)
    - 125 µL Propidium Iodide 1 mg/mL stock solution
    - 375 µL PBS
- PI 500 µg/mL (1:2)
    - 250 µL Propidium Iodide 1 mg/mL stock solution
    - 250 µL PBS

Unless stated otherwise, the 1:2 dilution of PI was used.

Rabbit IgG Iso-Antibody 1 µg/mL (Iso-IgG, primary AB)

- Iso-IgG 5 µg/mL (1:1000)
    - 0.5 µL Iso-IgG 5 mg/mL stock solution
    - 499.5 µL SmartBlock™ blocking buffer
- Iso-IgG 1 µg/mL (1:5000)
    - 200 µL Iso-IgG 5 µg/mL
    - 800 µL SmartBlock™ blocking buffer

Ki-67 recombinant rabbit monoclonal antibody 1:200 [0.155 µg/mL] (anti-Ki-67, primary AB)

- 5 µL anti-Ki-67 stock solution 0.031 mg/mL
- 995 µL SmartBlock™ blocking buffer

Vimentin rabbit polyclonal antibody 1:2000 [0.25 µg/mL] (anti-Vimentin, primary AB)

- 0.5 µL anti-Vimentin stock solution 0.5 mg/mL
- 999.5 µL SmartBlock™ blocking buffer

Alpha smooth muscle actin rabbit polyclonal antibody 1:500 [1.5 µg/mL] (anti-α-SMA, primary AB)

- 2 µL anti-α-SMA stock solution 0.750 mg/mL
- 998 µL SmartBlock™ blocking buffer

Alexa Fluor® 647-labelled anti-rabbit IgG 1:1000 [0.5 µg/mL] (secondary AB)

- 1 µL secondary antibody AF647 stock solution 0.5 mg/mL
- 999 µL SmartBlock™ blocking buffer

DAPI

- DAPI 1 µg/mL (used for staining of frozen cryosections)
    - 1 µL DAPI stock solution 1 mg/mL
    - 999 µL SmartBlock™ blocking buffer
- DAPI 10 µg/mL (used for flow cytometry)
    - 5 µL DAPI stock solution 1 mg/mL
    - 495 µL PBS

4 % Paraformaldehyde (PFA)

- Paraformaldehyde (PFA) 4 % (w/v)
- HEPES-buffered saline (HBS), pH 7.4
    - HEPES 20 mM
    - NaCl 150 mM
    - MilliQ-Water
    - NaOH for pH adjustment

30 % Sucrose

- Sucrose 30 % (w/v)
- PBS

7.2 General cell culture procedures

7.2.1 Maintaining cells

MDA-MB-231 cells were obtained from ATCC and modified with eGFP Luc label as described in Billerhart et al.[61] The human fibroblast cell line HMF3S, established from healthy mammary tissue, was a generous gift from Professor Mike O'Hare (Ludwig Institute, London, UK).[43] All used cell lines were cultured in T25 flasks and stored in the incubator at 37 °C and 5 % CO_2 (standard culture conditions). They were passaged twice a week (usually on Mondays and Fridays) or when a confluency of 75-95 % was reached. The incubation time

for detachment using TrypLE™ was 2.5 minutes for HMF3S cells and 4 minutes for MDA-MB-231 (including MDA-MB-231 PGK eGFP Luc) cells, respectively. Dependent on the cell line and confluency, a splitting ratio of 1:5-1:15 for both MDA cell lines and 1:15-1:30 for HMF3S were used.

7.2.2 Cell harvesting and counting

For cell harvesting, cells were detached from the flask and prewarmed medium was added to neutralize TrypLE , the suspension was transferred to a tube and centrifuged at 200 g for 5 minutes. Supernatant was removed and the cell pellet was resuspended in 1 mL fresh, prewarmed medium (referred to as “original cell suspension”).

Based on this original cell suspension, an appropriate dilution (usually 1:5-1:10) was prepared for counting. 10 µL of this dilution were transferred to both chambers of a Neubauer improved counting chamber and cells were counted using an Olympus IX73 microscope.

The number of cells counted in the two compartments was added up and multiplied by the respective dilution factor (i.e. 5 for a 1:5 dilution) to determine the cell concentration (cells/µL) of the original cell suspension. Based on this, the required volume per well containing the desired number of cells was calculated for seeding (see below), using the following formula:

$$N = D/Z * C$$

N… required volume per well
D… desired cell count per well
Z… number of cells per µL in the original cell suspension
C… required dilution factor to reach a pipetting volume of at least 20 µL

7.3 Generation of spheroids and their handling

7.3.1 Standard seeding procedure

To allow spheroid formation, an ultra-low attachment 96-well-plate with a round base (BIOFLOAT™, Sarstedt) was used. First, wells were filled with fresh, prewarmed medium before the desired amount of cell suspension was added working with a total volume of 200 µL per well . Experiments which required the addition of Basement Membrane Matrix (BMM)

were initially seeded in a total volume of 150 µL per well and 50 µL of medium with 8 % BMM (not prewarmed) were added to reach a final concentration of 2 % BMM. To the outermost wells of the plate 200 µL of PBS were added in order to enable the same conditions for all spheroids. Unless stated otherwise, the plate was centrifuged for 3 minutes at 300 g and stored in the incubator until further use.
The day on which the seeding was performed was defined as day 0 (D0).

7.3.2 Change of medium

During each experiment, the culture medium in the plate was replaced several times, starting no earlier than day 3. Medium changes were subsequently performed every second day during the week. For this purpose, 100 µL of old medium were carefully removed from each well and replaced with 100 µL of fresh, prewarmed medium. Depending on the experimental condition, either DMEM high glucose complete medium supplemented with 2 % BMM or without supplementation was used.

7.3.3 Phase contrast microscopy

Phase contrast microscopy was used to monitor spheroid formation and morphology throughout experiments. Images were acquired with an Olympus IX73 microscope at a 10x magnification, using cellSens standard software from Olympus.

7.4 Optimization of seeding conditions

To evaluate optimal conditions for spheroid formation, different ratios of MDA-MB-231 and HMF3S cells were tested for their suitability to form stable spheroids. Three different co-culture ratios were investigated: 1:4 (MDA-MB-231 to HMF3S), 1:3 and 1:2. Additionally, two monoculture controls were seeded containing only MDA-MB-231 or HMF3S cells, respectively. For the exact cell counts, see **Table 8** below.

Table 8. Seeding cell counts for optimization of seeding conditions.

	monoculture		**co-culture**		
	HMF3S	**MDA-MB-231**	**1:4 (MDA:HMF3S)**	**1:3 (MDA:HMF3S)**	**1:2 (MDA:HMF3S)**
cell count per well	3000	2000	1000 MDA-MB-231 + 3000 HMF3S	1000 MDA-MB-231 + 2000 HMF3S	2000 MDA-MB-231 + 2000 HMF3S

Seeding was carried out based on the procedure described in section 7.3.1. Two distinct approaches were applied for seeding initially: In one half of the 96-well plate, both cell lines were seeded on the same day (day 0), with one cell line added shortly after the other into the respective wells, resulting in a total volume of 200 µL per well. In the other half of the plate, MDA-MB-231 cells were seeded on day 0 in a total volume of 100 µL per well. On day 1, HMF3S cells were added together with the corresponding amount of culture medium, resulting in a final volume of 200 µL per well. For the exact seeding scheme, see **Figure 1**.

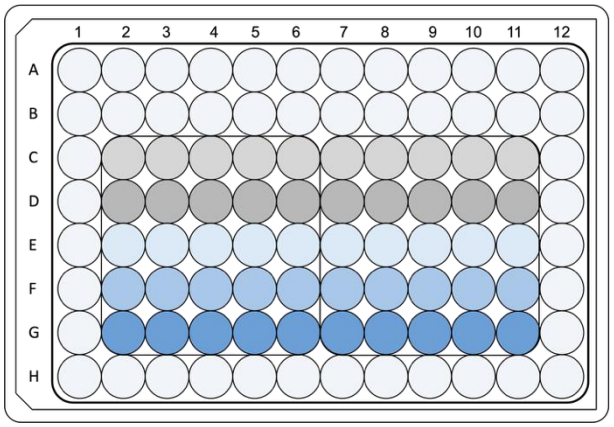

Figure 1. Seeding Scheme used for optimization of seeding conditions. *Gray shades indicate monoculture conditions (light gray: MDA-MB-231; dark gray: HMF3S) while blue shades represent co-cultures at different ratios (light blue: 1:4; medium blue: 1:3; dark blue: 1:2). Outermost wells are filled with PBS. Wells on the left side were seeded on day 0, whereas wells on the right side were seeded sequentially on day 0 and day 1.*

The plate was imaged using phase contrast microscopy as described in section 7.3.3. Images were acquired on day 1 (D1), D4, D5, D6, D8, D11, D12 and D13.

7.5 Growth and Viability Assessment

The aim of the following experiments was to evaluate spheroid growth by assessing both

metabolic activity as a measure of viability, as well as spheroid size. For this purpose, spheroids were generated based on the procedure described in section 7.3.1. In the first experiment (E02), cells were seeded sequentially. For co-culture spheroids, HMF3S cells were first seeded in 100 µL of culture medium per well. Subsequently, MDA-MB-231 cells were labelled with CellTrace™ CFSE according to the manufacturer and added to the corresponding wells. For monoculture controls, 10 wells for each were seeded containing only MDA-MB-231 or HMF3S, respectively. For exact cell counts, see **Table 9** below.

Table 9. Seeding cell counts for growth assessment experiments.

	monoculture		**co-culture**	
	HMF3S	**MDA-MB-231 (PGK eGFP Luc)**	**1:4 (MDA:HMF3S)**	**1:3 (MDA:HMF3S)**
cell count per well	3000	3000	750 MDA + 2250 HMF3S	1000 MDA + 2000 HMF3S

In this setup, the total medium volume was adjusted to 200 µL per well on the left half of the plate. Wells on the right half initially contained 150 µL of medium, followed by the addition of 50 µL of 8 % BMM in culture medium. After seeding, plates were centrifuged to promote spheroid formation. For the exact seeding scheme of this experiment, see **Figure 2**A.
In the second experiment (E06, seeding scheme see **Figure 2**B), MDA-MB-231 PGK eGFP Luc cells were used instead of MDA-MB-231. The required volumes of both cell suspensions (MDA and HMF3S) were mixed in a tube prior to seeding, allowing for simultaneous seeding of both cell lines into the respective wells. The seeding procedure was otherwise performed as described above.

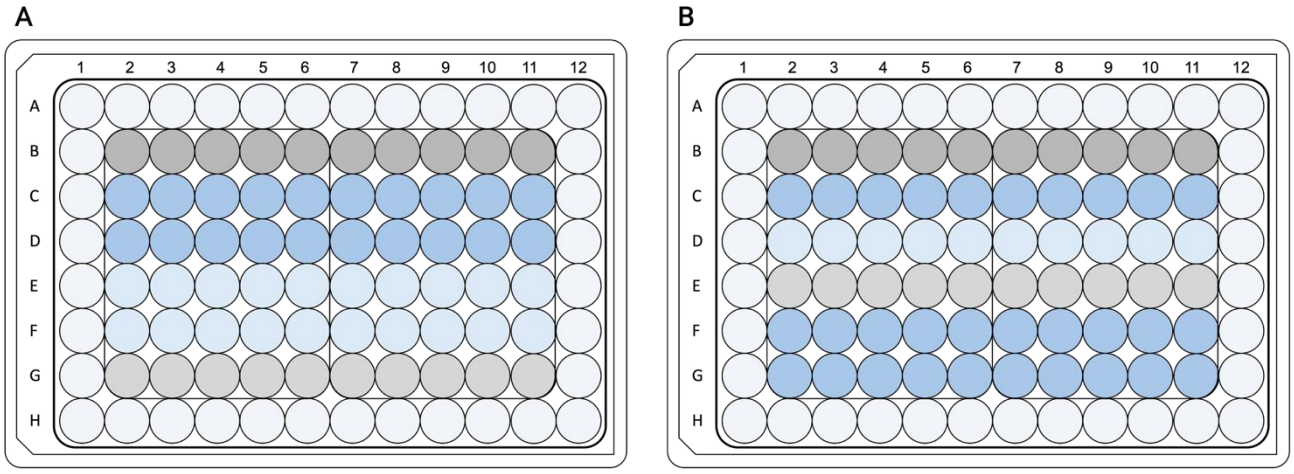

Figure 2. Seeding schemes A (E02) and B (E06). *Gray shades indicate monoculture conditions (light gray: MDA-MB-231 (PGK eGFP Luc); dark gray: HMF3S) while blue shades represent co-cultures at different ratios (light blue: 1:4; medium blue: 1:3). Outermost wells are filled with PBS. Wells on the right half of each plate contain BMM in the culture medium, whereas wells on the left half do not.*

7.5.1 Metabolic activity assay

The assay was carried out with minimal exposure to light. Resazurin solution was prepared as mentioned in section 7.1. First, 120 µL of old medium were removed from the respective spheroid-containing wells and temporarily transferred to a flat-bottom 96-well plate. Subsequently, the remaining medium was removed and 108 µL of fresh prewarmed medium and 12 µL of Resazurin solution were added to each respective well (final volume 120 µL per well). Furthermore, three of the PBS-filled wells were used as blanks. Therefore, PBS was completely removed and replaced with 108 µL of fresh medium and 12 µL of Resazurin solution per well. The plate was incubated for 4 hours under standard culture conditions.

After incubation, 100 µL of the Resazurin-containing supernatant from each well were transferred to a fresh flat-bottom 96-well plate and set aside protected from light for measurement. The remaining supernatant was carefully removed and 100 µL of the previously collected old medium were returned to each spheroid-containing well, to maintain the standard culture conditions. Fresh medium (100 µL) was added to respective wells on the left half (- BMM) of the plate, while wells on the right half (+ BMM) received 100 µL of fresh medium supplemented with 2 % BMM, resulting again in a final volume of 200 µL per well. Blank wells were refilled with PBS.

The assay was performed on D3, D7 and D10. For measurement, a Tecan® infinite M200Pro plate reader was used with the settings described in **Table 10**.

Table 10. Settings of the Tecan® infinite M200Pro plate reader *for the measurement of the metabolic activity assay.*

Parameter	Setting
Mode	Fluorescence bottom reading
Excitation wavelength	560 nm
Emission wavelength	590 nm
Excitation bandwidth	9 nm
Emission bandwidth	20 nm
Gain	170
Number of flashes	25
Integration time	20 µs

The analysis was done with Microsoft Excel. All measured values within an experiment were normalized to the average value of HMF3S monoculture spheroids (- BMM) on D3: First, the average of the blank replicates was subtracted from every single measured value. Each of these new values were then divided by the average of the replicates of HMF3S monoculture spheroids (- BMM) on D3. Lastly, the average and standard deviation (SD) were calculated for each replicate. This was carried out for all spheroid types (monoculture spheroids, ratio 1:3 and 1:4 of co-culture spheroids) and conditions (- / + BMM) for each day (D3, D7 and D10).

7.5.2 Size analysis

To assess the size of the spheroids, images were acquired on D3, D7 and D10 of experiments E02 and E06 using phase contrast microscopy as described in section 7.3.3 above. Based on these images, the area of each spheroid was calculated using the software ImageJ. The values were further analyzed with Microsoft Excel. Therefore, the mean and standard deviation (SD) of the replicates were calculated. In addition, the values were normalized to those of HMF3S monoculture spheroids (- BMM) on D3 as a baseline, similar to metabolic activity analysis. For each spheroid type (monoculture spheroids, ratio 1:3 and 1:4 of co-culture spheroids), the two conditions (- / + BMM) were tested with a t-test with unequal variances (Welch's t-test), since the variances were found to be different for most groups.

7.6 Necrotic core assessment

To evaluate necrotic core formation, spheroids were analyzed by live/dead staining and fluorescence microscopy.

Spheroids were generated according to section 7.3.1. For seeding of co-culture spheroids, cell suspensions of HMF3S and MDA-MB-231 PGK eGFP Luc were mixed in a tube prior to seeding to ensure simultaneous seeding into wells and 8 % BMM in culture medium was added to one half of the plate as described in section 7.3.1. Exact cell counts are depicted in **Table 9** above. **Figure 3**A shows the seeding schemes of experiment E03 for the assessment of necrotic core formation at co-culture ratio 1:4, whereas **Figure 3**B depicts the seeding scheme of experiment E06 in which the analysis was conducted at co-culture ratio 1:3. Each experiment was performed twice.

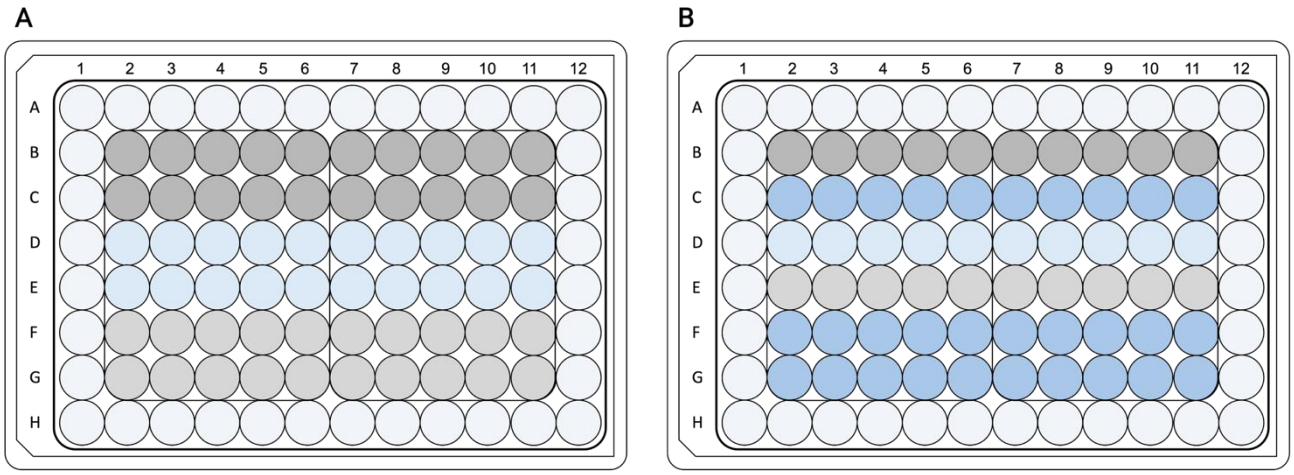

Figure 3. Seeding schemes A (E03) and B (E06). *Gray shades indicate monoculture conditions (light gray: MDA-MB-231 PGK eGFP Luc; dark gray: HMF3S) while blue shades represent co-cultures at different ratios (light blue: 1:4; medium blue: 1:3). Outermost wells are filled with PBS. Wells on the right half of each plate contain BMM in the culture medium, whereas wells on the left half do not.*

7.6.1 Live/Dead staining

Hoechst was used as it labels the DNA of all cell nuclei irrespective of cell viability. It exhibits an excitation maximum at approx. 350 nm and an emission maximum at approx. 461 nm. PI selectively stains non-viable cells due to its inability to penetrate intact cell membranes and was therefore used to detect the necrotic core. PI has an excitation maximum at approx. 493 nm and an emission maximum at approx. 636 nm.[62]

Hoechst and propidium iodide (PI) solutions were prepared as described in section 7.1. For the first run of E03, the PI concentration used was 250 µg/mL, while the twofold

concentration (500 µg/mL) was used in the repeated run and in E06.
For the staining procedure, 20 µL of old culture medium were removed from each respective well. Subsequently, 10 µL of Hoechst solution and 10 µL of PI solution were added to each well under light-protected conditions to restore a final volume of 200 µL. The plate was then incubated for 2 hours under standard culture conditions.
After incubation, spheroids were washed with PBS by carefully removing 160 µL of supernatant (to minimize spheroid loss) and adding an equal volume of PBS. This washing procedure was performed well by well and repeated twice, resulting in a total of three washing steps.

7.6.2 Fluorescence microscopy

After washing the spheroids with PBS as described above, fluorescence imaging was performed using an Olympus IX73 inverted microscope and a 10x objective (gain set to 4). Hoechst staining was visualized using a DAPI filter, while PI fluorescence was detected using a Cy3 filter. The corresponding settings are summarized in **Table 11**.

Table 11. Fluorescence microscopy settings for live/dead staining.

Filter	**Exposure [ms]**
DAPI (Ex 325-375, DC 400, Em 435-485)	20
Cy3 (Ex 545/30, DC 570, Em 620/60)	5
phase contrast	10

Images from the middle of the spheroid and additionally z-stacks with 41 sections (10 µm step size) were acquired and processed using the cellSens standard software from Olympus. Live/Dead staining and subsequent fluorescence microscopy were performed on D1, D3, D7 and D10 of respective experiments.

7.7 Histological assessment

To gain deeper insight into the structural and cellular characteristics of the generated spheroids, a histological and immunohistochemical (IHC) evaluation was carried out. The analysis focused on the morphology, density and structural organization within the spheroids. Furthermore, specific markers were assessed to evaluate proliferative activity, mesenchymal transition and fibroblast activation.

In general, spheroids were generated according to the procedure described in section 7.3.1 above. For histological assessment by Hematoxylin and Eosin (H&E) staining, spheroids of experiment E02 (described in section 7.5 (see **Figure 2**A for the seeding scheme and **Table 9** for exact seeding cell counts)) and E03 (outlined in section 7.6 (see **Figure 3**A for the seeding scheme and **Table 9** for exact seeding cell counts)) were analyzed.
For the immunohistochemical evaluation, spheroids from E03 were used.

7.7.1 Harvesting and embedding of spheroids

For harvesting, the culture medium was completely removed from the respective well. In E02, spheroids were washed with PBS prior to further processing. Spheroids from E03 were harvested directly after live/dead staining and FLM imaging, therefore no additional PBS washing step was required.
Subsequently, spheroids were carefully aspirated using a 1000 µL pipette set to 200 µL uptake volume and transferred into 0.5 mL tubes.
For E02, spheroids were then fixed and cryoprotected. For this, PBS was completely removed from the tubes, leaving only the spheroid, and 200 µL of 4% PFA in HBS (pH 7.4) were added. Samples were incubated at room temperature for 1 h. After fixation, the PFA solution was removed, replaced with 200 µL of 30 % sucrose in PBS and again incubated at room temperature for 1-3 h until the spheroids had sunk to the ground of the tube (typically 1-1.5 h were sufficient). Each spheroid was then transferred onto a prepared casting mold containing a drop of OCT compound (Tissue-Tek®), frozen on dry ice, covered with additional OCT and stored at -20°C until sectioning.
In experiment E03, spheroids were embedded in OCT immediately after harvesting, without prior fixation or sucrose incubation. Samples were placed onto casting molds containing OCT as described above, frozen on dry ice and stored at -20°C until sectioning.

7.7.2 Sectioning of spheroids

Sections were made using a cryostat offset to -20°C. Sectioning of embedded spheroids was performed at a thickness of 6 µm, with a trimming thickness of 20 µm. The generated sections were picked up onto glass slides (maximum of eight sections per slide) and stored at -20°C until further processing.

7.7.3 Hematoxylin and Eosin staining

For H&E staining, the frozen spheroid areas on the slides were circled using a PAP pen to

create a hydrophobic barrier. Sections were covered with 4 % PFA for 7 minutes at room temperature. After fixation, PFA was removed and the slides were rinsed twice in PBS for 3 minutes each to remove residual OCT compound and PFA, followed by washing in running tap water for 1 minute.

For the first staining step, the slides were placed in Hematoxylin solution for 30 seconds. After washing remaining dye off in tap water for 20 seconds, sections were incubated in ammonia water (NH_4OH) for 20 seconds, followed by an additional rinse in tap water for 1 minute. For the second staining step, slides were placed in Eosin solution for 45 seconds and briefly rinsed in tap water for 10 seconds, to remove excess dye. The fixation and staining procedures are summarized in **Table 12** below.

For dehydration, sections were passed through an ascending ethanol series (3 x 70 %, 3 x 96 % and 3 x 100 %, 1 second per dip each), followed by incubation in xylene two times for 1 minute each. An overview of the dehydration series is provided in **Table 13** below. After this step, sections were mounted in Entellan™ mounting medium for preservation and light microscopy.

Table 12. H&E staining protocol *including fixation and staining steps with corresponding incubation times.*

fixation		**staining**						
4% PFA	PBS	tap water	Hema-toxylin	tap water	NH_4OH	tap water	Eosin	tap water
7’	2 x 3’	1’	30’’	20’’	20’’	1’	45’’	10’’

Table 13. Dehydration series following H&E staining.

dehydration			
70% EtOH	96% EtOH	100% EtOH	Xylene
3 x 1’’	3 x 1’’	3 x 1’’	2 x 1’

Images of the stained sections were acquired using bright field microscopy on an Olympus BX53 light microscope at a 20x magnification. The cellSens standard software from Olympus was used for image acquisition.

7.7.4 Immunohistochemical (IHC) staining

For IHC staining, frozen tissue sections were circled using a hydrophobic barrier pen (PAP

pen). Sections were immediately fixed with 4 % PFA for 7 minutes at room temperature. Excess fixative was removed and slides were rinsed twice with PBS for 3 minutes each to eliminate residual embedding compound and PFA.

Following fixation, slides were placed in a humid chamber and incubated with SmartBlock™ blocking buffer (25 µL per section) for 60 minutes at room temperature. After removal of the blocking buffer, sections were incubated with the respective primary antibody (anti-Ki-67, anti-Vimentin and anti-α-SMA, preparation see section 7.1) or isotype control antibody (iso-IgG) as illustrated in **Figure 4**. 25 µL of the respective antibody solution were pipetted onto each section. Primary antibody incubation was either carried out for 120 minutes at room temperature or overnight at 4°C.

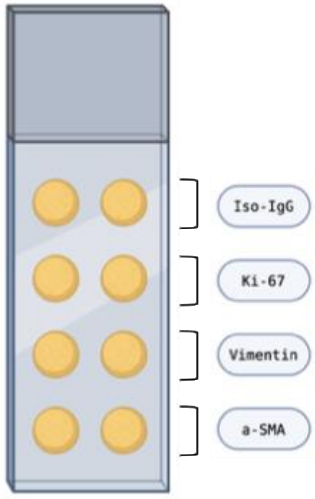

Figure 4. Schematic overview of slide layout showing primary antibody and isotype control allocation. *Two sections per slide were incubated with the same primary antibody or isotype control, respectively. Created with BioRender.*

Subsequently, sections were washed twice with PBS for 3 minutes each and incubated with AF647-labelled secondary antibody (25 µL per section, preparation see section 7.1) for 120 minutes at room temperature in the dark. Afterwards, slides were washed twice with PBS for 3 minutes each and incubated with DAPI (1 µg/mL and 25 µL per section, see section 7.1) for 20 minutes at room temperature under light protection for nuclear counterstaining.

Slides were washed again twice with PBS for 3 minutes each. Finally, sections were mounted using Vectashield PLUS® mounting medium (approximately 25 µL per slide) and coverslips were sealed with nail polish. For the detailed IHC staining procedure, see **Table 14** below.

Table 14. IHC staining protocol *including nuclear counterstaining with DAPI. RT = room temperature, AB = antibody.*

fixation		staining						
4% PFA	PBS	blocking buffer	prim. AB	PBS	sec. AB	PBS	DAPI	PBS
7’	2 x 3’	60’	120’ (RT) or overnight (4°C)	2 x 3’	120’ (RT)	2 x 3’	20’	2 x 3’

7.7.4.1 Fluorescence microscopy of IHC stained sections

Fluorescence imaging was performed using an Olympus IX73 inverted microscope and a 20x objective. The gain was set to 0. Different filters were used for detection. The detailed settings, including filters and corresponding exposure times, are provided in **Table 15**. Images were acquired using the cellSens standard software from Olympus.

Table 15. Fluorescence microscopy settings for IHC stained sections.

Target detected	Filter	Exposure [ms]
Ki-67, Vimentin or α-SMA [Alexa Fluor ® 647 (sec. AB)]	Cy5 (Ex 620/60, DC 660, Em 700/75)	300
MDA-MB-231 PGK eGFP Luc cells [eGFP]	FITC (Ex 470/40, DC 495, Em 525/50)	400
cell nuclei [DAPI]	DAPI (Ex 325-375, DC 400, Em 435-485;)	300
cell morphology	phase contrast	100

7.8 Evaluation of spheroid composition

To assess the distribution of MDA-MB-231 PGK eGFP Luc and HMF3S cells within co-culture spheroids, flow cytometry (FCM) was performed to determine the relative proportions of each cell population.

In contrast to experiments described above, cell numbers were determined using a MACSQuant® flow cytometer. Based on the “original cell suspension” obtained after cell harvesting (see section 7.2.2), a 1:10 dilution was prepared separately for each cell line. For

each diluted sample, three measurements of 50 µL each were carried out. The mean cell count was calculated and multiplied by 10 (dilution factor) to determine the number of cells per µL of the original cell suspension.

Spheroids were subsequently generated as described in section 7.3.1. For co-culture conditions, cell suspensions of HMF3S and MDA-MB-231 PGK eGFP Luc were mixed in a tube prior to seeding to ensure simultaneous seeding into respective wells. Co-culture spheroids were established at ratios of 1:4 and 1:3. In addition, monoculture spheroids of HMF3S and MDA-MB-231 PGK eGFP Luc were generated as controls, as illustrated in the seeding scheme below (**Figure 5**). For exact cell counts, see **Table 9** in section 7.5 above. In contrast to most experiments described above, no basement membrane matrix (BMM) was used in the experiments presented in this section. The experiment was repeated twice, resulting in three independent replicates.

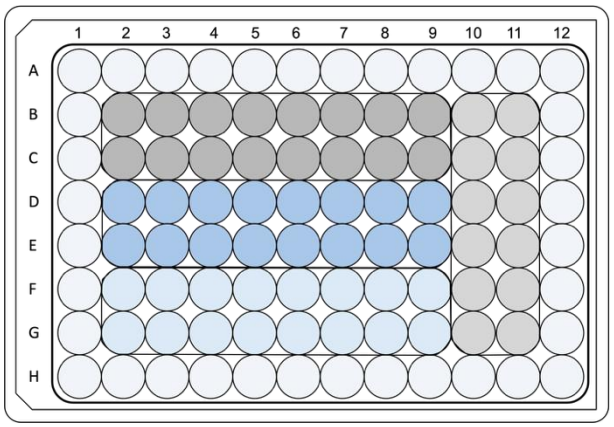

Figure 5. Seeding Scheme used for flow cytometry experiments. *Gray shades indicate monoculture conditions (light gray: MDA-MB-231 PGK eGFP Luc; dark gray: HMF3S) while blue shades represent co-cultures at different ratios (light blue: 1:4; medium blue: 1:3). Outermost wells are filled with PBS.*

7.8.1 Disintegration of spheroids for flow cytometric analysis

Flow cytometry read-out was performed on D3 and D7 for each independent experiment. Spheroids were washed once with PBS and two spheroids per condition (MDA monoculture, HMF3S monoculture, co-culture 1:4 or co-culture 1:3) were transferred into a 1.5 mL tube to generate one sample.

For HMF3S monoculture and co-culture spheroids, residual PBS was carefully removed prior to enzymatic dissociation. Subsequently, 100 µL of TrypLE™ were added to each tube and samples were incubated for 4 minutes at room temperature. This incubation step was followed by mechanical disruption through repetitive pipetting (10 times up and down). This

cycle of incubation and pipetting was repeated until complete dissociation was achieved and no intact spheroid structures were visible (typically 3-4 cycles). After complete dissociation, 200 µL PBS were added to minimize the enzymatic reaction by dilution.
In contrast, MDA-MB-231 PGK eGFP Luc monocultures did not form stable spheroids. Therefore, enzymatic dissociation was not required and dissociation was achieved by gently resuspending the cells in PBS several times without addition of TrypLE™.
Subsequently, all samples were centrifuged at 200 g for 5 minutes. For enzymatically dissociated samples, 280 µL of the supernatant were carefully discarded to remove the diluted TrypLE and the remaining cell pellet was resuspended in 70 µL PBS, resulting in a final volume of 90 µL. Briefly before flow cytometric measurement, 10 µL of DAPI (10 µg/mL in PBS, see section 7.1) were added to each sample to enable exclusion of non-viable cells. A MACSQuant® flow cytometer was used for FCM measurement. V1 (showing DAPI) and B1 (showing eGFP) channels were adjusted prior with respective negative and positive samples and saved as instrument settings. These were used for all three experiments.

7.8.2 Gating strategy for flow cytometric (FCM) analysis

Data was analyzed using FlowJo software (v.10.8) with a sequential gating strategy as follows. First, the total cell population was identified by plotting side scatter area (SSC-A) versus forward scatter area (FSC-A), and debris was excluded by gating the main cell population. Subsequently, single cells were selected by plotting FSC-A versus FSC-H (forward scatter height) to exclude doublets. Viable cells were then identified by excluding DAPI-positive events in a plot of Vioblue (V1) versus FSC-A. Within the viable single-cell population, eGFP-positive and eGFP-negative cells were distinguished based on FITC-A (B1) fluorescence intensity plotted against FSC-A. For visualization of eGFP distribution, a histogram of FITC-A was generated, showing a maximum of two distinct peaks corresponding to the two cell populations (eGFP-positive and eGFP-negative).
Gates were initially set using HMF3S monoculture samples from Day 3 (first read-out day) as a control and subsequently copied to all other monoculture and co-culture samples from D3 and D7 read-outs. This gating strategy was also applied for the analysis of counted cells (before seeding).

7.9 Declaration on the use of AI tools

In the preparation of this thesis, AI-based tools were used in a supportive manner.

NotebookLM (https://notebooklm.google.com) was employed to assist with the organization, navigation and summarization of academic sources. Additionally, ChatGPT (https://chatgpt.com) and Gemini (https://gemini.google.com) were used exclusively to improve the clarity, structure and linguistic quality of text based on my original drafts. No confidential research data were processed using these tools. AI tools were not used to generate original scientific content, research data, hypotheses, interpretations or conclusions. All AI-assisted outputs were carefully reviewed and proofread before inclusion to ensure accuracy and compliance with scientific standards. Schematic figures were created using BioRender (https://biorender.com).

8 Results and Discussion

8.1 Optimization of seeding conditions

To determine optimal seeding conditions for spheroid formation, three different co-culture ratios of MDA-MB-231 and HMF3S cells (1:2, 1:3 and 1:4) were evaluated. In addition to varying cell ratios, two seeding strategies were compared. In the first approach, both cell lines were seeded on the same day (day 0 = D0), with one cell line added shortly after the other into respective wells. In the second approach, MDA-MB-231 cells were seeded on D0 and HMF3S cells were added on D1. Phase contrast images were acquired on D1, D4, D5, D6, D8, D11, D12 and D13 to monitor spheroid formation and morphological development over time.

As shown in **Figure 6** (same-day seeding, D0) and **Figure 7** (sequential seeding, D0/D1) below, both approaches supported the formation of spheroids. Given the comparable outcomes, same-day seeding was chosen for subsequent experiments due to its simplified experimental workflow.

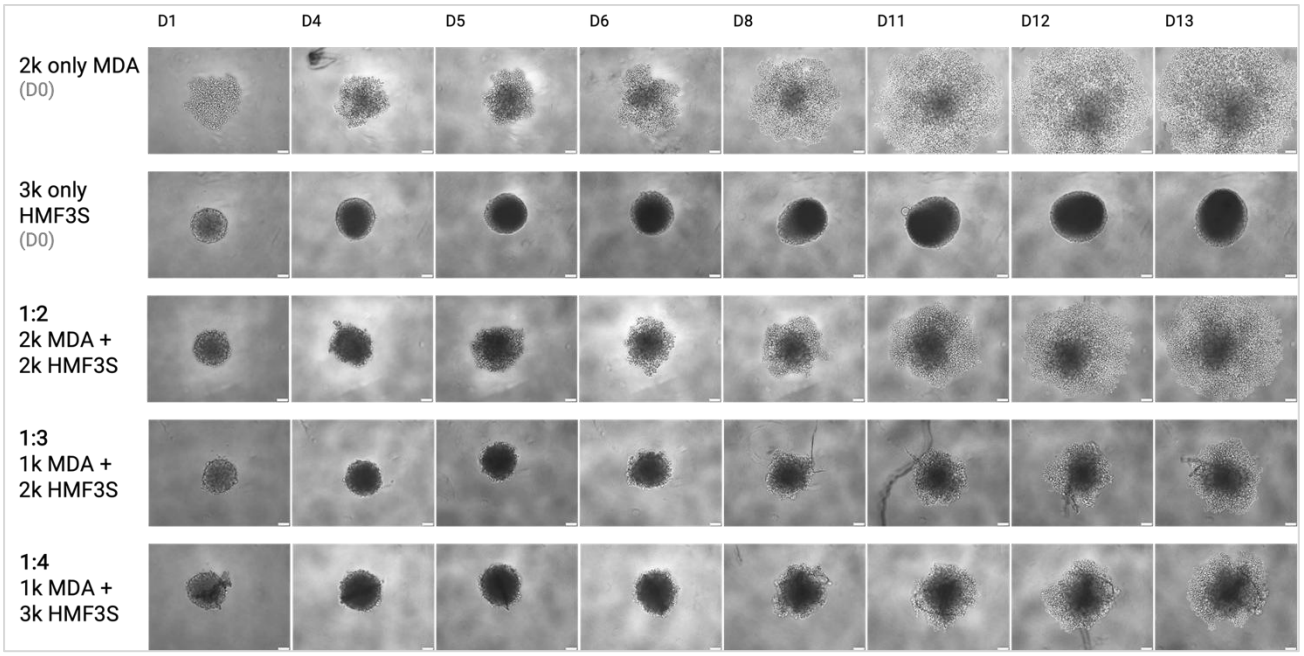

Figure 6. Phase contrast microscopy images of whole spheroids and cellular aggregates for same-day seeding (day 0). *Representative phase contrast images of MDA-MB-231 and HMF3S monocultures as well as co-cultures of the ratio 1:2, 1:3 and 1:4 generated by seeding on Day 0. Depending on the culture ratio and time point, morphologies range from loose cell aggregates to fully formed spheroids. Images were acquired using a 10x objective on days 1, 4, 5, 6, 8, 11, 12 and 13 to monitor spheroid formation and structural changes over time. Scale bar = 100 µm.*

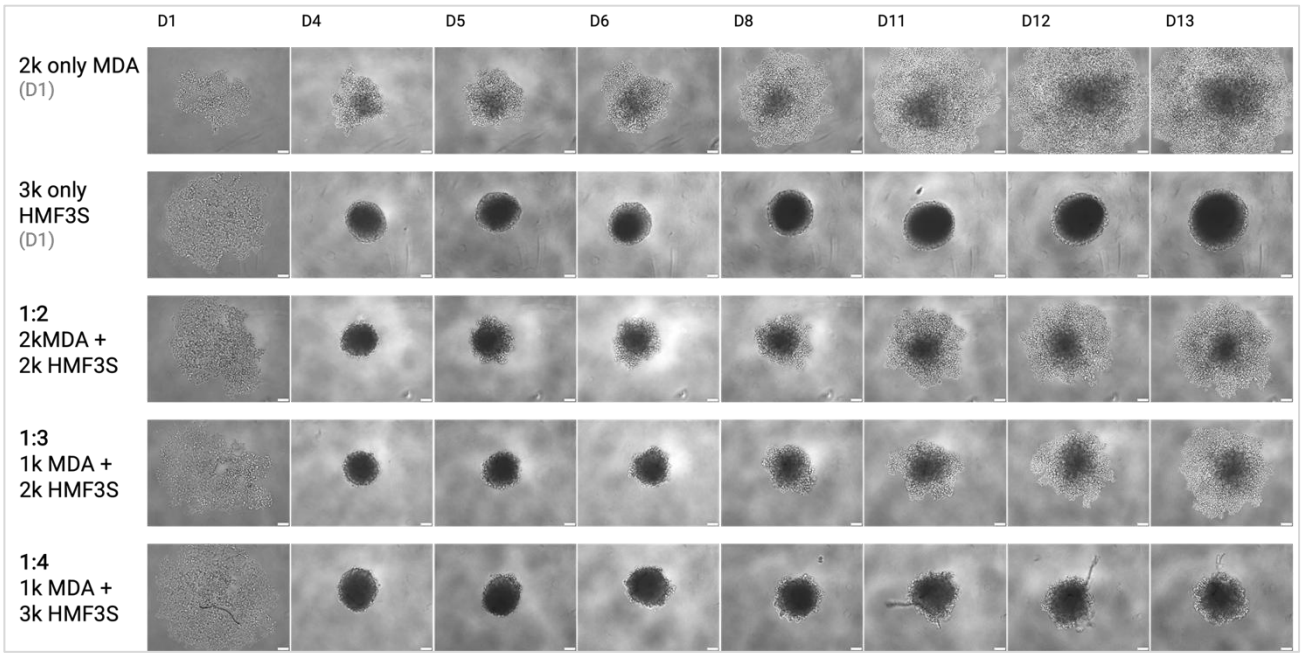

Figure 7. Phase contrast microscopy images of whole spheroids and cellular aggregates for sequential seeding (day 0/day 1). *Representative phase contrast images of MDA-MB-231 and HMF3S monocultures as well as co-cultures of the ratio 1:2, 1:3 and 1:4 generated by seeding MDA-MB-231 cells on Day 0 and adding HMF3S cells on Day 1. Depending on the culture ratio and time point, morphologies range from loose cell aggregates to fully formed spheroids. Images were acquired using a 10x objective on days 1, 4, 5, 6, 8, 11, 12 and 13 to monitor spheroid formation and structural changes over time. Scale bar = 100 µm.*

MDA-MB-231 monocultures did not form compact spheroids but rather loosely organized cell aggregates, coinciding with previous reported results.[63,64] In contrast, HMF3S monocultures consistently developed dense and well-defined spheroids. This difference may be attributed to altered cell-cell adhesion properties of malignant cells such as MDA-MB-231, which are frequently characterized by reduced E-cadherin expression and impaired intercellular junction formation.[65]

The co-culture ratios 1:3 and 1:4 resulted in the most structurally stable formation of spheroids and were therefore selected for subsequent experiments. A higher proportion of fibroblasts has been reported to correlate with accelerated spheroid formation and increased stability in 3D co-culture systems. This effect is primarily mediated by an enhanced deposition of extracellular matrix (ECM) proteins produced by fibroblasts, which function as a “glue” and promote cohesion of tumor cells that otherwise exhibit a tendency toward dissociation.[12,66,67] However, from D6 onwards, co-culture spheroids from every ratio exhibited structural instability, leading to partial outgrowth in some samples. This was also seen during harvesting, which was occasionally impaired due to reduced compactness of the outgrowth and only the remaining compact inner core was harvestable.

This observed peripheral outgrowth pattern suggests that MDA-MB-231 cells may preferentially localize and expand at the spheroid margin. This spatial organization may reflect differences in proliferation rates or adhesive properties between the two cell populations. If the malignant and less adhesive MDA-MB-231 cells proliferate more rapidly than the structurally stabilizing HMF3S cells, the resulting imbalance could contribute to reduced overall compactness of the aggregates, leading to their loose appearance.[65,68] Furthermore, depletion of nutrients and oxygen within spheroids represent physiological stressors that can promote invasive behavior and induce malignant cells to detach and migrate toward regions with higher nutrient availability, thereby contributing to the expansion of MDA-MB-231 cells at the spheroid margin.[12] However, mechanically induced stress by pipetting during medium exchange can also lead to extensive outgrowth, as observed in later experiments.

8.2 Growth assessment

This section discusses the evaluation of spheroid growth, assessed by measuring spheroid size as well as metabolic activity. MDA-MB-231 (PGK eGFP Luc) and HMF3S monocultures were analyzed alongside co-cultures at ratio 1:3 and 1:4. Furthermore, the impact of BMM supplementation on spheroid size and metabolic activity was investigated in comparison to untreated conditions.

8.2.1 Metabolic activity

Metabolic activity was assessed on Days 3, 7 and 10 to monitor spheroid viability over time. Across mono- and co-culture conditions, a time-dependent increase in metabolic activity was observed (see **Figure 8**), suggesting spheroid growth and enhanced cellular activity throughout the cultivation period.

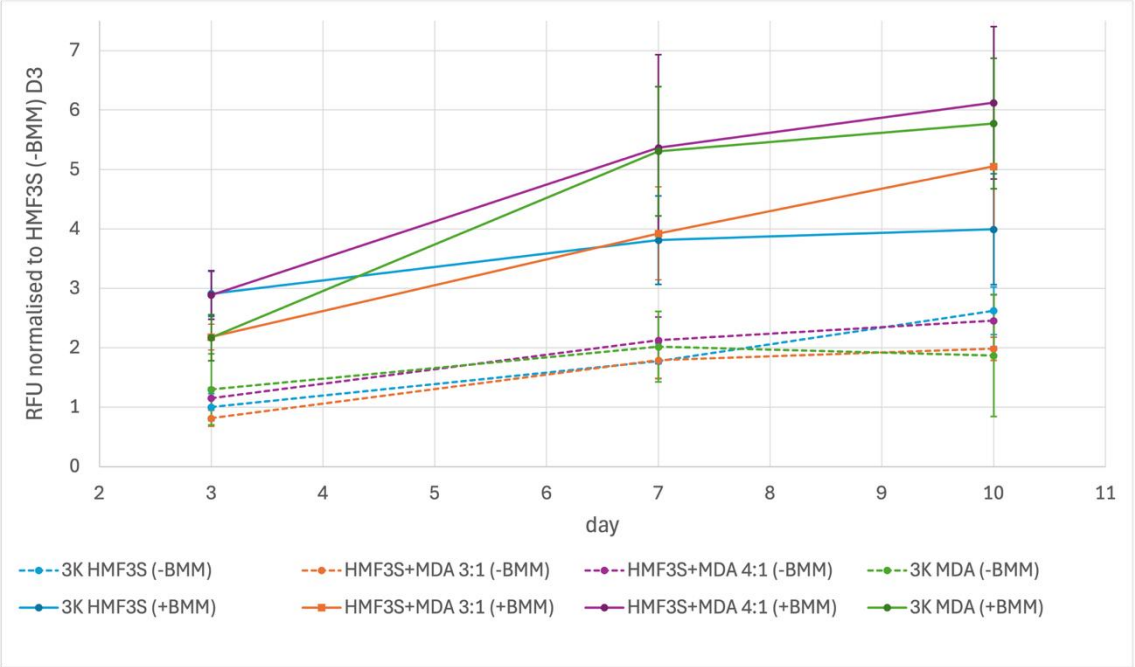

Figure 8. Time-dependent changes in metabolic activity of mono- and co-cultures from Resazurin viability assay. *Metabolic activity was assessed on days 3, 7 and 10 and is presented as fold change to HMF3S (-BMM) D3 (relative fluorescence units (RFU) normalized to HMF3S (-BMM) D3). Data represent mean ± SD of at least n=7 replicates per condition. Exact n-values are provided in the Appendix (**Table 16**).*

Notably, spheroids cultured in the presence of BMM consistently exhibited significantly higher metabolic activity compared to non-supplemented controls at all assessed time points with a strong increase in viability up to D10. This indicates that BMM supplementation may promote cellular viability and proliferation within the 3D structures. A possible explanation lies in its ability to mimic key aspects of the tumor microenvironment (TME). BMM is a basement membrane extract derived from mouse tumors and is enriched in extracellular matrix (ECM) components such as laminin, collagen-IV, entactin as well as growth factors including IGF-1, TGF-β, VEGF, EGF and b-FGF. These components are known to activate signaling pathways, which regulate cell cycle progression and inhibit apoptosis.[47,69-71]

In contrast, BMM-free conditions resulted in overall lower variability, still showing a moderate increase in viability during the culture period. Additionally, reduced standard deviations (see **Figure 9**) suggest enhanced reproducibility of the experimental system. Conversely, although BMM supported spheroid formation in MDA-MB-231 monocultures, this condition was associated with greater dispersion of measured values, indicating increased heterogeneity and limited experimental reproducibility.

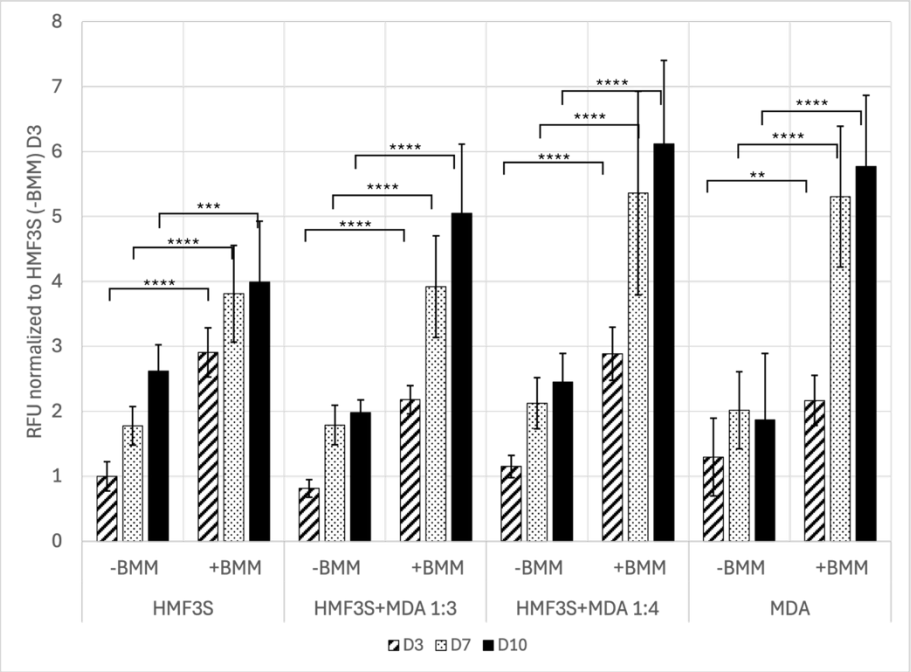

Figure 9. Comparison of metabolic activity between mono- and co-cultures from Resazurin viability assay at days 3, 7 and 10. *Data are presented as fold change to HMF3S (-BMM) D3 (RFU normalized to HMF3S (-BMM) D3; mean ± SD). Exact n-values are provided in the Appendix (**Table 16**). Statistical analysis was performed using Welch's t-Test. * p<0.05, ** p<0.01, *** p<0.001, **** p<0.0001.*

While BMM supplementation was associated with increased metabolic activity, this finding may be interpreted with caution, as assay-specific limitations can influence the read-out. BMM provides ECM cues that promote the formation of highly compact spheroids, potentially creating a physical barrier that limits the diffusion of resazurin, as previously described by Walzl et al.[72] As this assay relies on passive probe penetration, limited diffusion can lead to a read-out that predominantly reflects the activity of cells in outer spheroid layers rather than the entire cellular mass. Consequently, significant inter-sample variability may potentially be caused by inconsistent penetration.[11,72,73]

8.2.2 Size analysis

To complement the metabolic activity data, spheroid growth was evaluated by quantitative size analysis of whole spheroids. Spheroid area was calculated from phase contrast images using Fiji software, allowing assessment of structural development across the different culture conditions.

Quantitative size analysis revealed that cultures with the addition of BMM exhibited significantly larger spheroid areas compared to cultures without BMM across most experimental conditions (see **Figure 10**). This difference reached statistical significance at all assessed time points, with the exception of HMF3S monocultures on day 10 and MDA-

MB-231 monocultures on day 3, where no significant differences were observed. The overall increase in size in BMM-supplemented conditions is consistent with the viability data obtained from the metabolic activity assay, suggesting enhanced proliferative capacity under these conditions. The alignment between functional and morphological parameters supports the reliability of the observed growth phenotype.

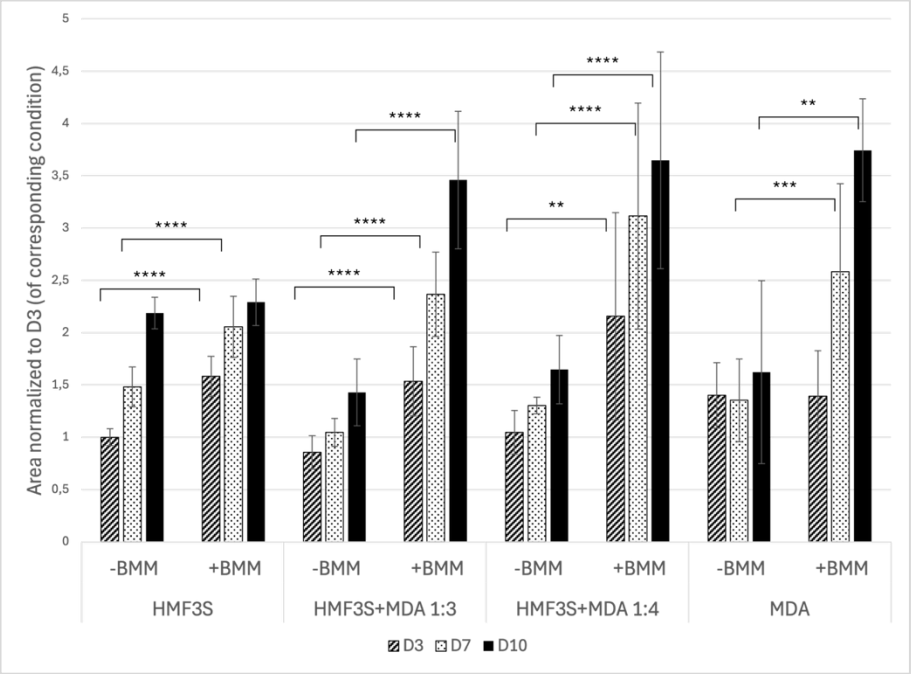

Figure 10. Image analysis based comparison of spheroid size between mono- and co-cultures at days 3, 7 and 10. *Spheroid area was normalized to day 3 HMF3S -BMM and is presented as mean ± SD. Statistical analysis was performed using Welch's t-Test. Exact n-values are provided in the Appendix (Table 17). * p<0.05, ** p<0.01, *** p<0.001, **** p<0.0001.*

8.3 Necrotic core assessment

To evaluate necrotic core formation, live/dead staining was performed on days 1, 3, 7 and 10 in monocultures of HMF3S and MDA-MB-231 PGK eGFP Luc as well as in co-cultures at ratio 1:3 and 1:4. In addition, the influence of BMM supplementation on necrotic core size was assessed to determine its impact on spheroid viability and spatial distribution of dead cells.

Generally, a larger necrotic core was observed in cultures without BMM supplementation (see **Figure 11** and **Figure 12**).

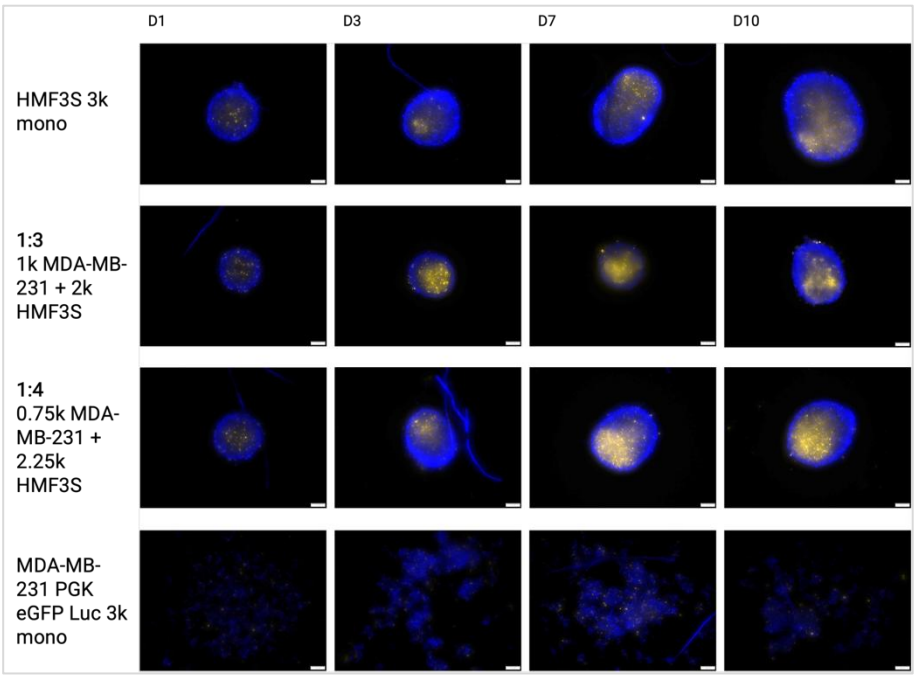

Figure 11. Representative fluorescence microscopy images of live/dead stained whole mono- and co-culture spheroids and cellular aggregates <u>without BMM supplementation</u> *at days 1, 3, 7 and 10. Nuclei of all cells are shown in blue (Hoechst, exposure time = 20 ms), whereas dead cells are visualized in yellow (PI, exposure time = 5 ms). Images were acquired with a 10x objective and show one out of n=4 spheroids each. Scale bar = 100 µm.*

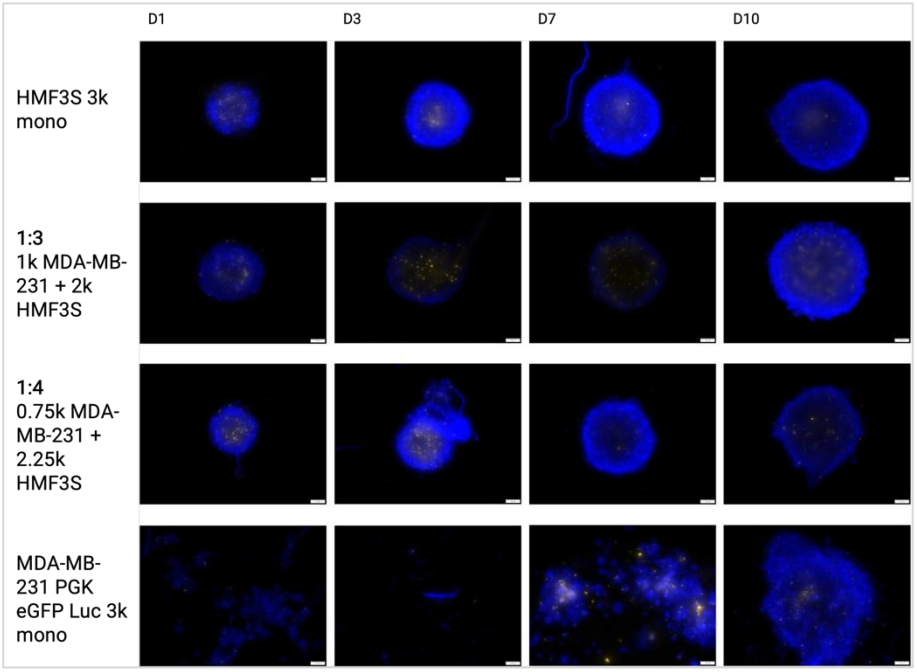

Figure 12. Representative fluorescence microscopy images of live/dead stained whole mono- and co-culture spheroids and cellular aggregates <u>with BMM supplementation</u> *at days 1, 3, 7 and 10. Nuclei of all cells are shown in blue (Hoechst, exposure time = 20 ms), whereas dead cells are visualized in yellow (PI, exposure time = 5 ms). Images were acquired with a 10x objective and show one out of n=4 spheroids each. Scale bar = 100 µm.*

Notably, this difference was maintained throughout all subsequent time points and remained consistently evident across all cultures of this condition. The reduced necrotic core size in

cultures with BMM-addition may further support the assumption that BMM promotes improved cell survival, potentially by enhancing oxygen and nutrient availability within the spheroid structure. Previous findings by Badea et al. suggest that the presence of Matrigel® may enhance proliferation due to its high protein and growth factor content, thereby promoting ECM conditions comparable to those observed *in vivo*. However, this did not correspond with a reduction in necrotic core formation, indicating that enhanced proliferation does not automatically translate into lower hypoxic conditions in dense spheroid structures.[74]

Nevertheless, the presence of a larger necrotic core in cultures without BMM supplementation might not necessarily be interpreted as a disadvantage. Solid tumors *in vivo* frequently develop central necrotic regions due to diffusion limitations and metabolic gradients.[75]

Therefore, the formation of a larger necrotic core may indicate a structural and physiological resemblance to native tumor tissue.

8.4 Histological and immunohistochemical characterization

This section presents the evaluation of the overall morphology in mono- and co-cultures, assessed by hematoxylin and eosin (H&E) staining. In addition, the expression and localization of specific markers were analyzed by immunohistochemical (IHC) staining.

8.4.1 Assessment of morphology by H&E staining

To investigate morphology by H&E staining, two experimental approaches were performed. In the first, samples from almost all culture conditions (monocultures of MDA-MB-231 (PGK eGFP Luc) and HMF3S; co-cultures at ratio 1:3 and 1:4; with and without BMM supplementation) were harvested at multiple time points, fixed, cryoprotected and subsequently embedded for sectioning.

In the second experimental setup, samples were harvested immediately after the live/dead staining and directly embedded in OCT compound without prior fixation or cryoprotection. Due to the experimental design, this approach included monocultures of MDA-MB-231 PGK eGFP Luc and HMF3S as well as co-cultures at ratio 1:4 only (with and without BMM supplementation).

It should be noted that harvesting of the MDA-monoculture condition (without BMM) was attempted only at day 6 (see fixed and cryoprotected samples **Figure 14**). As the cultures

formed merely loose cellular aggregates rather than stable, compact spheroids, the sample material was not suitable for collection and further processing. Therefore, this condition was not included in subsequent harvesting time points.

Histological analysis of fixed and cryoprotected samples suggested that supplementation with BMM (see **Figure 13**) resulted in a less densely packed tissue architecture compared to cultures without BMM (see **Figure 14**).

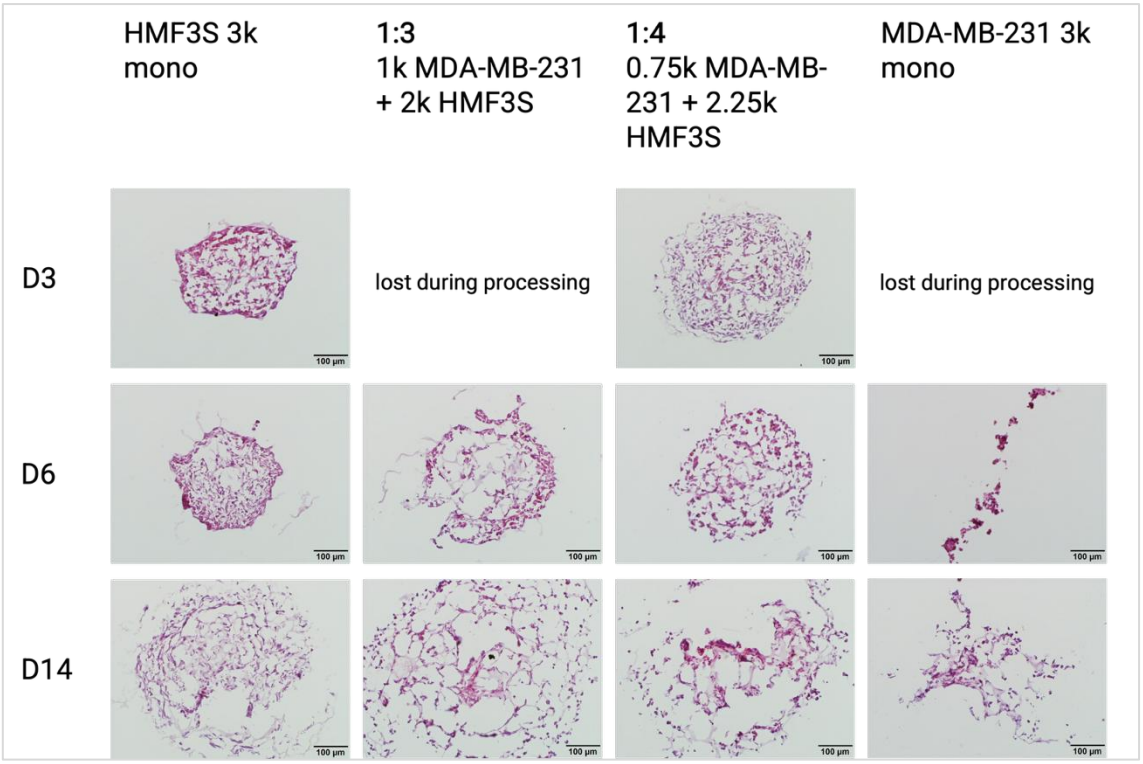

Figure 13. Representative brightfield microscopy images of H&E-stained sections from fixed and cryoprotected samples *derived from mono- and co-cultures with BMM supplementation at days 3, 6 and 14. Nuclei are shown in blue (hematoxylin), whereas cytoplasmic structures are visualized in pink (eosin). Panels without images indicate samples that were lost during processing. Images were acquired using a 20x objective. Scale bar = 100 µm.*

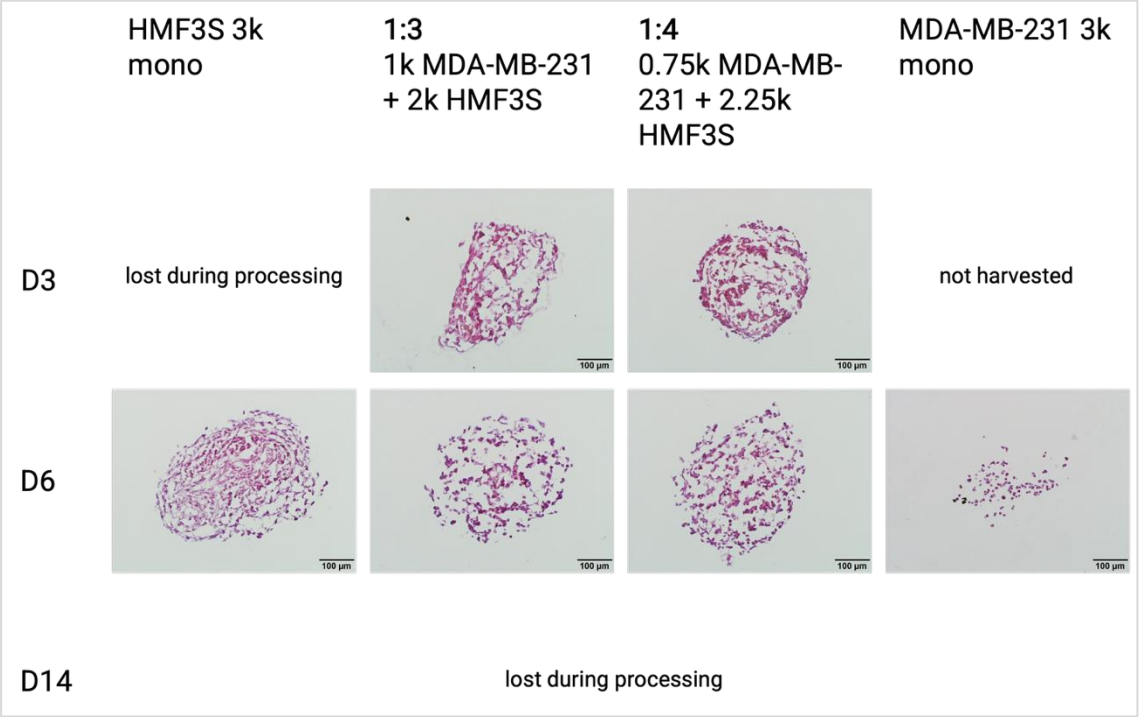

Figure 14. Representative brightfield microscopy images of H&E-stained sections from fixed and cryoprotected samples *derived from mono- and co-cultures without BMM supplementation at days 3, 6 and 14. Nuclei are shown in blue (hematoxylin), whereas cytoplasmic structures are visualized in pink (eosin). Panels without images indicate samples that were not harvested or were lost during processing. Images were acquired using a 20x objective. Scale bar = 100 µm.*

However, the overall structural preservation appeared compromised, as the sections exhibited features which indicate a reduced cellular integrity. A possible explanation may be prolonged exposure of the samples to PBS prior to initiation of the fixation procedure, which could have negatively affected tissue morphology. Therefore, conclusions drawn from these images should be interpreted with caution.

In contrast to the fixed and cryoprotected sections, samples that were directly embedded in OCT without prior fixation exhibited improved structural preservation. Similar to the observations described above, sections from cultures supplemented with BMM (see **Figure 15**) displayed a less densely packed architecture compared to non-supplemented conditions (see **Figure 16**).

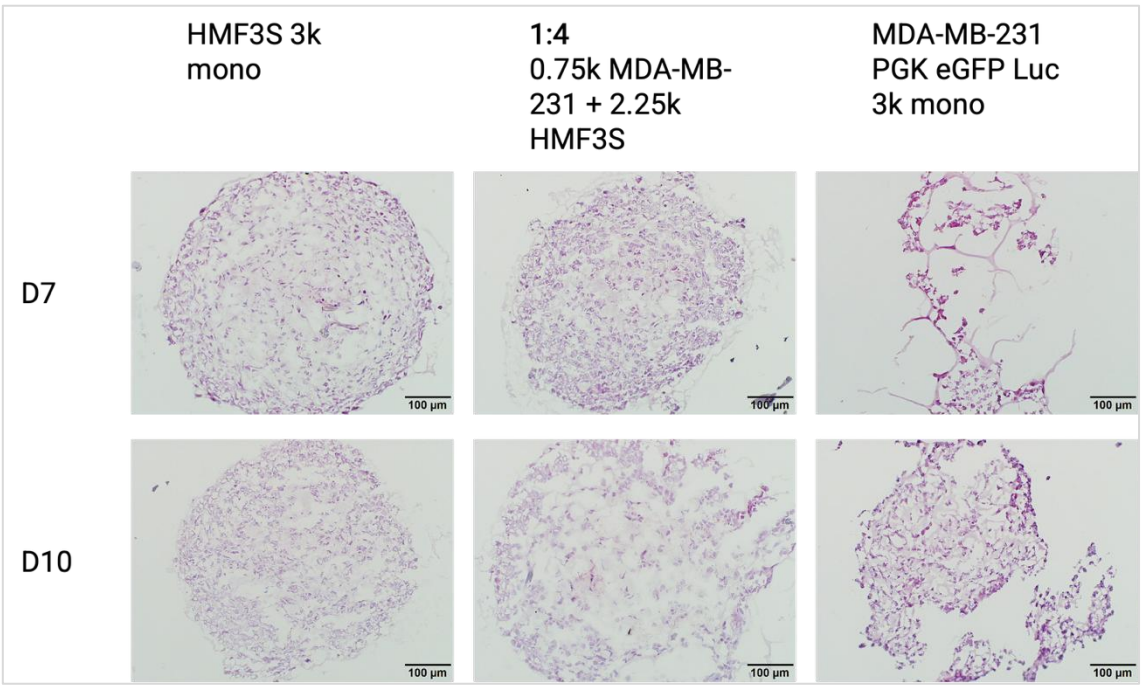

Figure 15. Representative brightfield microscopy images of H&E-stained sections from samples directly embedded in OCT *without prior fixation or cryoprotection. Samples were derived from mono- and co-cultures (at ratio 1:4) with BMM supplementation at days 7 and 10. Nuclei are shown in blue (hematoxylin), whereas cytoplasmic structures are visualized in pink (eosin). Images were acquired using a 20x objective. Scale bar = 100 µm.*

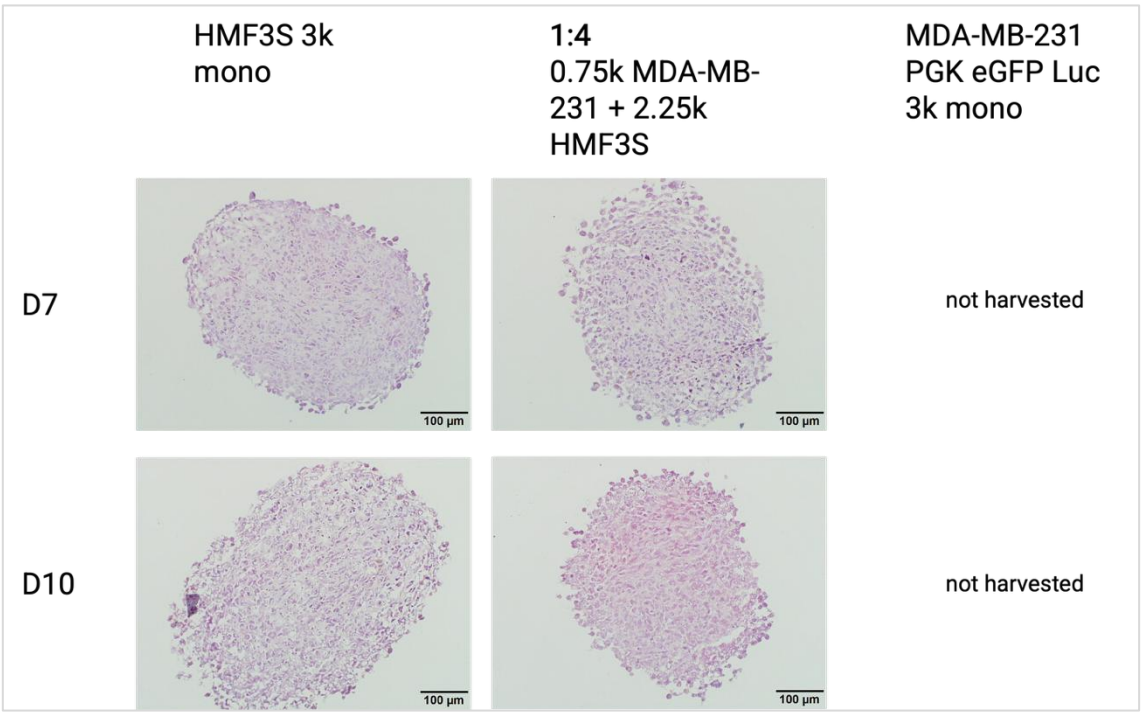

Figure 16. Representative brightfield microscopy images of H&E-stained sections from samples directly embedded in OCT *without prior fixation or cryoprotection. Samples were derived from mono- and co-cultures (at ratio 1:4) without BMM supplementation at days 7 and 10. Nuclei are shown in blue (hematoxylin), whereas cytoplasmic structures are visualized in pink (eosin). Panels without images indicate samples that were not harvested. Images were acquired using a 20x objective. Scale bar = 100 µm.*

Notably, BMM-supplemented samples appeared structurally more fragile, as indicated by the presence of porous, sponge-like regions within the tissue. The faint pink eosinophilic staining of the highlighted areas is suggestive for a net-like integrated BMM.

Interestingly, the comparatively less compact morphology of BMM-supplemented cultures lies in contrast to the findings from previous chapters, which suggested that the supplementation promotes the formation of highly compact spheroids that may in some cases even act as diffusion barriers. One possible explanation for this apparent discrepancy is that in scaffold-free cultures cellular agglomeration is primarily driven by direct cell-cell adhesion, resulting in a tightly packed microscopic architecture.[76] In contrast, additives, such as BMM, may occupy interstitial space and mechanically separate adjacent cells, thereby increasing extracellular volume and reducing apparent cellular density in tissue sections.[47]

8.4.2 Immunohistochemical analysis of marker expression

To further characterize the generated spheroids, IHC staining was performed. Selected markers were used to assess proliferation (Ki-67), spatial distribution of both cell lines (eGFP and Vimentin) and fibroblast activation (α-SMA), with the aim to provide additional insight into the functional and structural properties of the cultures. Staining was carried out on spheroids harvested on day 7 and 10 from monocultures of HMF3S and MDA-MB-231 PGK eGFP Luc as well as co-cultures of ratio 1:4, each generated with and without BMM supplementation.

DAPI was applied as a nuclear counterstain in all IHC stainings. However, no sufficient signal was observed at the time of fluorescence imaging. This may be attributable to fluorescence fading during the interval between staining and image acquisition. Consequently, nuclear localization could not be reliably assessed. While this limits the interpretability regarding precise spatial relationships and cellular distribution, marker-associated fluorescence signals were clearly detectable and were therefore analyzed qualitatively.

8.4.2.1 eGFP from MDA-MB-231 PGK eGFP Luc cells

In contrast to the antibody-based stainings described below, this analysis focused on the fluorescence of eGFP, which is selectively expressed by MDA-MB-231 PGK eGFP Luc cells but not in HMF3S cells. This approach was intended to enable discrimination between both cell populations within co-culture spheroids.

As shown in Figure 17, a weak fluorescence signal was detectable in the MDA-MB-231 PGK

eGFP Luc monoculture (+ BMM). In contrast, no sufficient signal was observed in the remaining culture conditions. The absence of fluorescence in HMF3S monocultures was expected, as these cells do not express the reporter protein. Nevertheless, signal intensity was insufficient to allow reliable spatial discrimination between both cell lines within the co-culture spheroids.

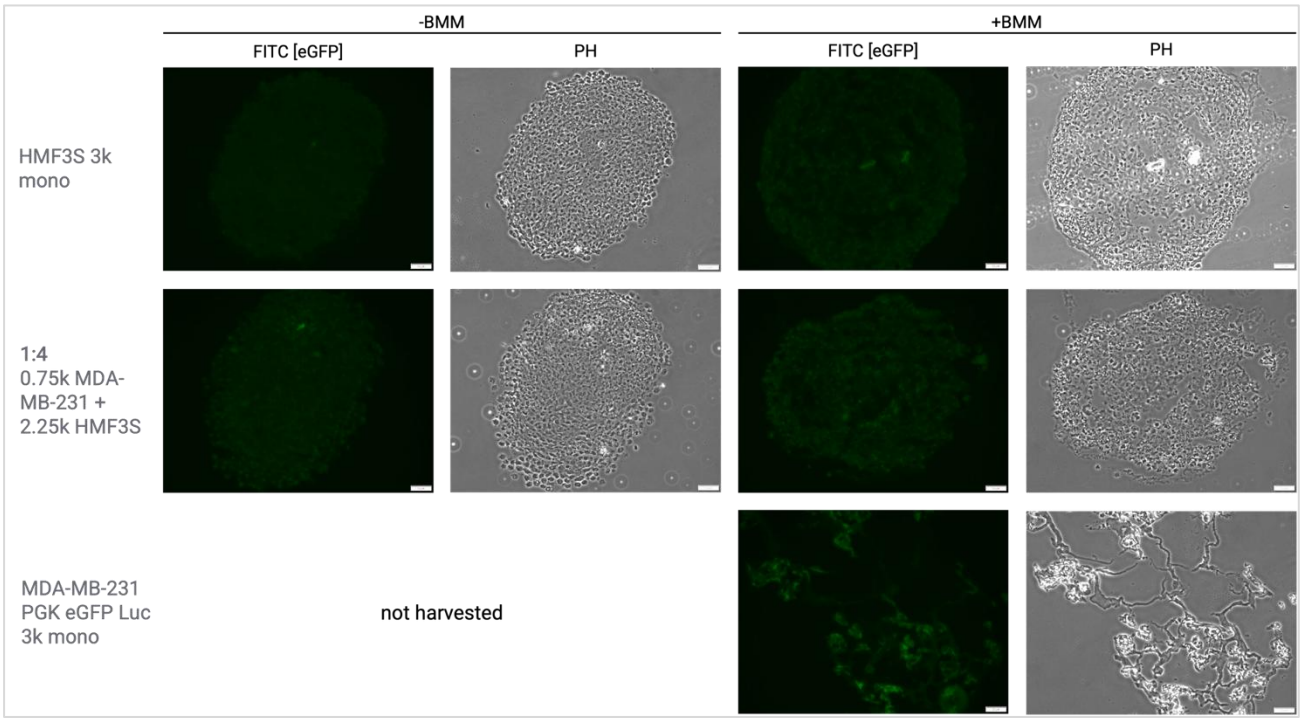

Figure 17. Fluorescence of eGFP in sections of mono- and co-cultures. *Representative fluorescence microscopy (FLM) images and corresponding phase contrast (PH) images of mono- and co-cultures (at ratio 1:4) with and without BMM supplementation on day 7. Panels without images indicate samples that were not harvested. A FITC filter set was used to visualize eGFP and images were acquired using a 20x objective. Scale bar = 50 µm.*

The reduced fluorescence intensity may be attributable to signal attenuation during fixation and processing, as fluorescent reporter proteins can be sensitive to chemical fixation. However, a more biologically plausible explanation might be oxygen deprivation within the spheroid microenvironment. Chromophore maturation of eGFP is oxygen-dependent. Thus, reduced oxygen availability, as commonly observed in 3D spheroid models due to diffusion gradients, may impair proper fluorophore formation and consequently diminish detectable fluorescence. Furthermore, severe oxygen limitation can suppress overall translational activity, potentially leading to reduced eGFP synthesis.[77] Additionally, as eGFP is cytoplasmic and therefore unbound, the protein could be washed out during the staining process, explaining the faint and heterogeneous signal.

8.4.2.2 Ki-67

To assess cellular proliferation within the spheroid cultures, IHC staining for Ki-67 was performed. This marker is commonly used to identify proliferating cells and thus allows evaluation of proliferative activity within the different culture conditions.

As shown in **Figure 18** and **Figure 19**, staining was observed in HMF3S monocultures and co-cultures at ratio 1:4. In contrast, almost no signal was detected in MDA-MB-231 PGK eGFP monocultures (+ BMM) on both day 7 and day 10. Furthermore, no significant difference was visible between cultures with and without BMM supplementation as well as between day 7 and day 10.

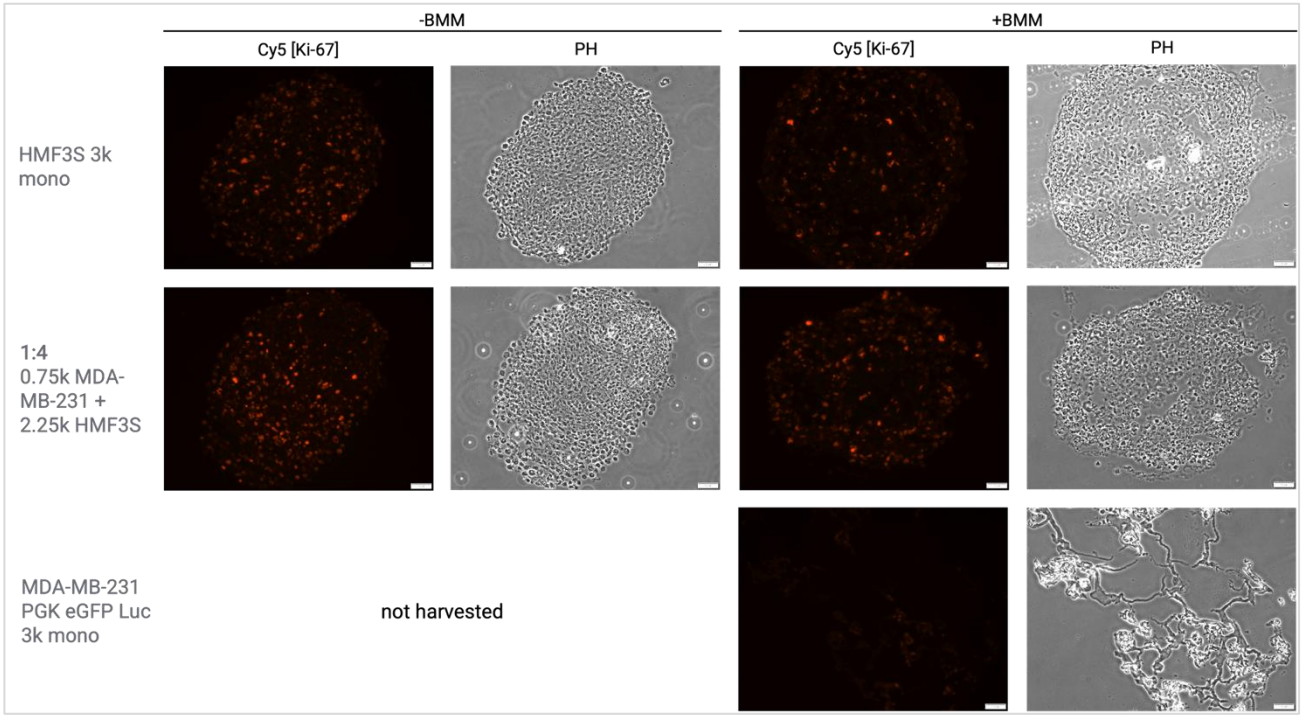

Figure 18. IHC staining of Ki-67 in sections of spheroids harvested on day 7. *Representative fluorescence microscopy (FLM) images and corresponding phase contrast (PH) images of mono- and co-cultures (at ratio 1:4) with and without BMM supplementation. Panels without images indicate samples that were not harvested. A Cy5 filter set was used to visualize Ki-67 and images were acquired using a 20x objective. Scale bar = 50 µm.*

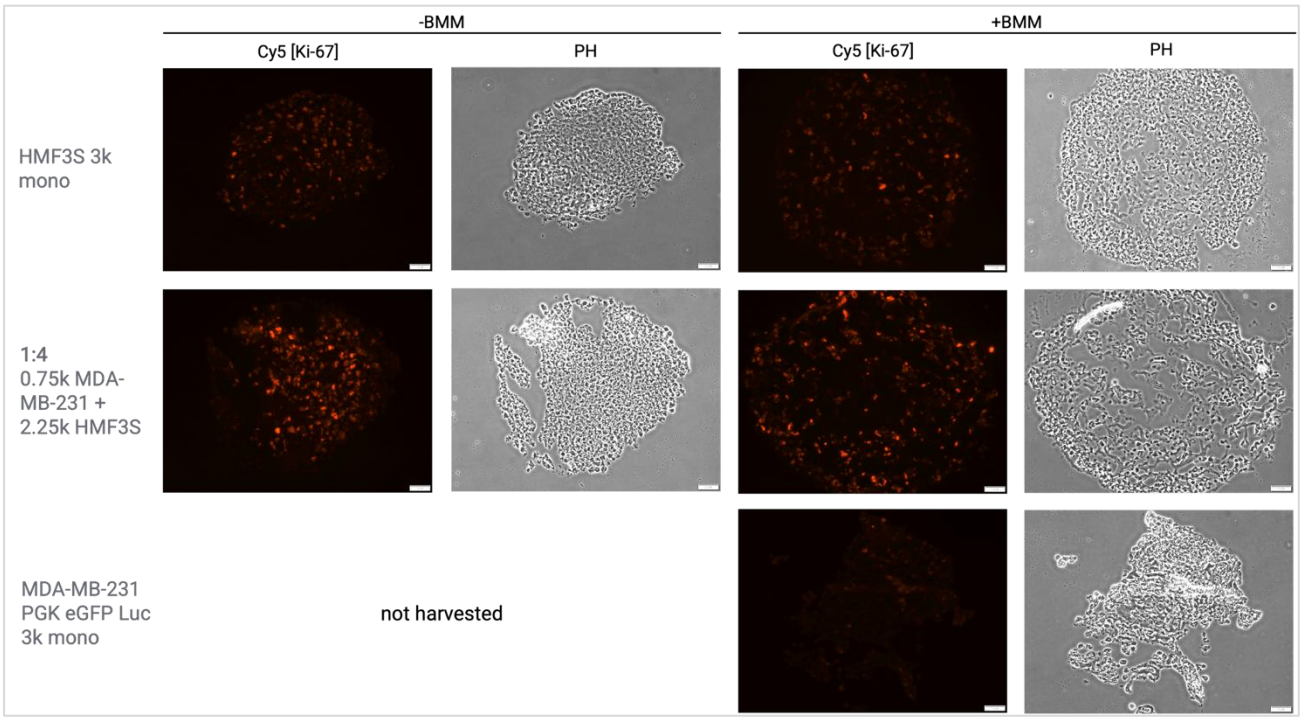

Figure 19. IHC staining of Ki-67 in sections of spheroids harvested on day 10. *Representative fluorescence microscopy (FLM) images and corresponding phase contrast (PH) images of mono- and co-cultures (at ratio 1:4) with and without BMM supplementation. Panels without images indicate samples that were not harvested. A Cy5 filter set was used to visualize Ki-67 and images were acquired using a 20x objective. Scale bar = 50 µm.*

Interestingly, Ki-67 positive cells were also detected in regions corresponding to the inner parts of the spheroid sections, where necrotic areas were observed in previous experiments. This apparent overlap may reflect the spatial heterogeneity that is typical of 3D spheroid models. Necrotic regions are often irregularly distributed and viable cells can still be present in adjacent areas.[19,74] Furthermore, histological sections represent only a 2D picture of a 3D structure, which may lead to apparent co-localization of proliferative and necrotic regions.

One possible explanation for the low signal observed in MDA-MB-231 PKG eGFP Luc monocultures could be their time-dependent proliferative capacity. Previous studies have reported a significant decline in the number of Ki-67 positive cells in MDA-MB-231 spheroids between culture days 7 and 14.[19,70] Moreover, in monoculture, MDA-MB-231 cells lack interactions with stromal cells, particularly fibroblasts, which normally secrete mitogenic paracrine factors such as IL-6, EGF or TGF-β. Consequently, key proliferative and survival pathways (e.g., STAT3 and PI3K/AKT) may be less strongly activated, potentially resulting in reduced baseline proliferation compared to co-culture models.[12,67,78]

8.4.2.3 Vimentin

To evaluate epithelial-mesenchymal transition (EMT) and to distinguish between the TNBC

and fibroblast populations within the spheroids, IHC staining for vimentin was performed. Clear vimentin staining was observed in HMF3S monocultures as well as in co-cultures at ratio 1:4 (both + / - BMM) on day 7 and day 10. Likewise, a vimentin signal was detected in monocultures of MDA-MB-231 PGK eGFP Luc under both conditions and at both time points (see Figure 20 and Figure 21). Consequently, IHC staining for vimentin did not allow a clear distinction between the two cell lines within the spheroid sections.

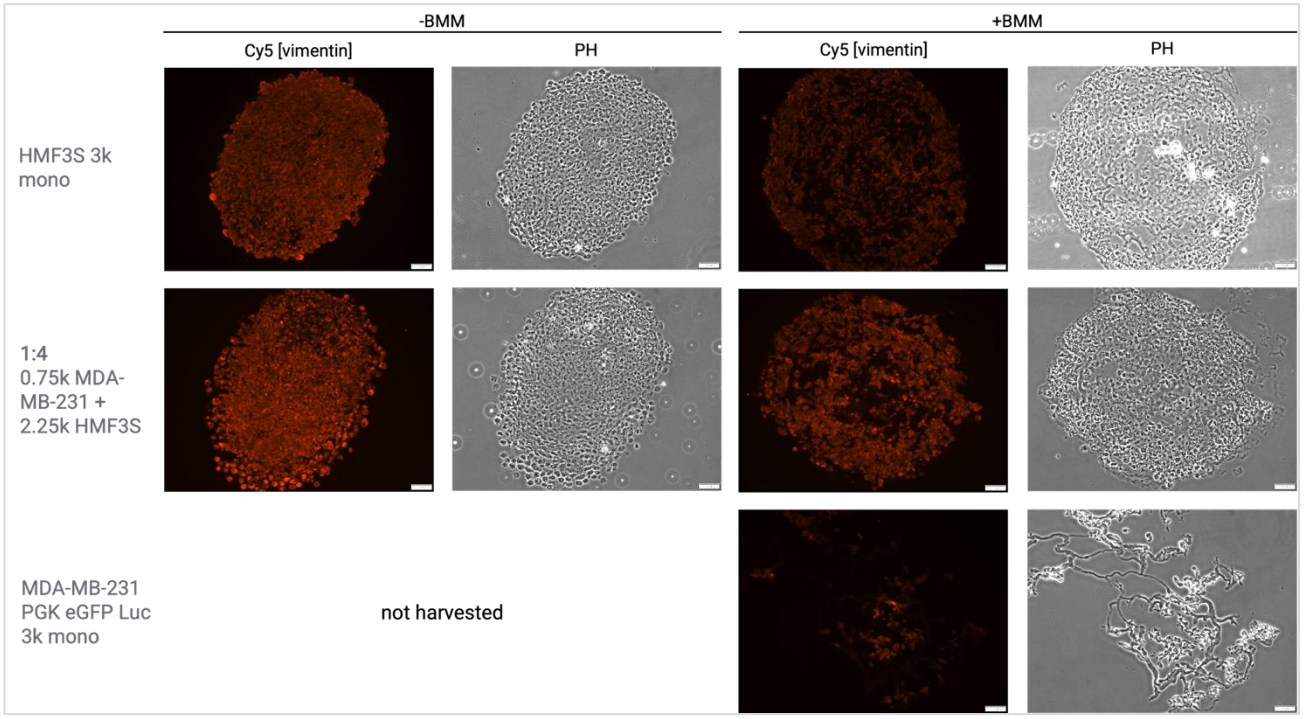

Figure 20. IHC staining of vimentin in sections of spheroids harvested on day 7. *Representative fluorescence microscopy (FLM) images and corresponding phase contrast (PH) images of mono- and co-cultures (at ratio 1:4) with and without BMM supplementation. Panels without images indicate samples that were not harvested. A Cy5 filter set was used to visualize vimentin and images were acquired using a 20x objective. Scale bar = 50 µm.*

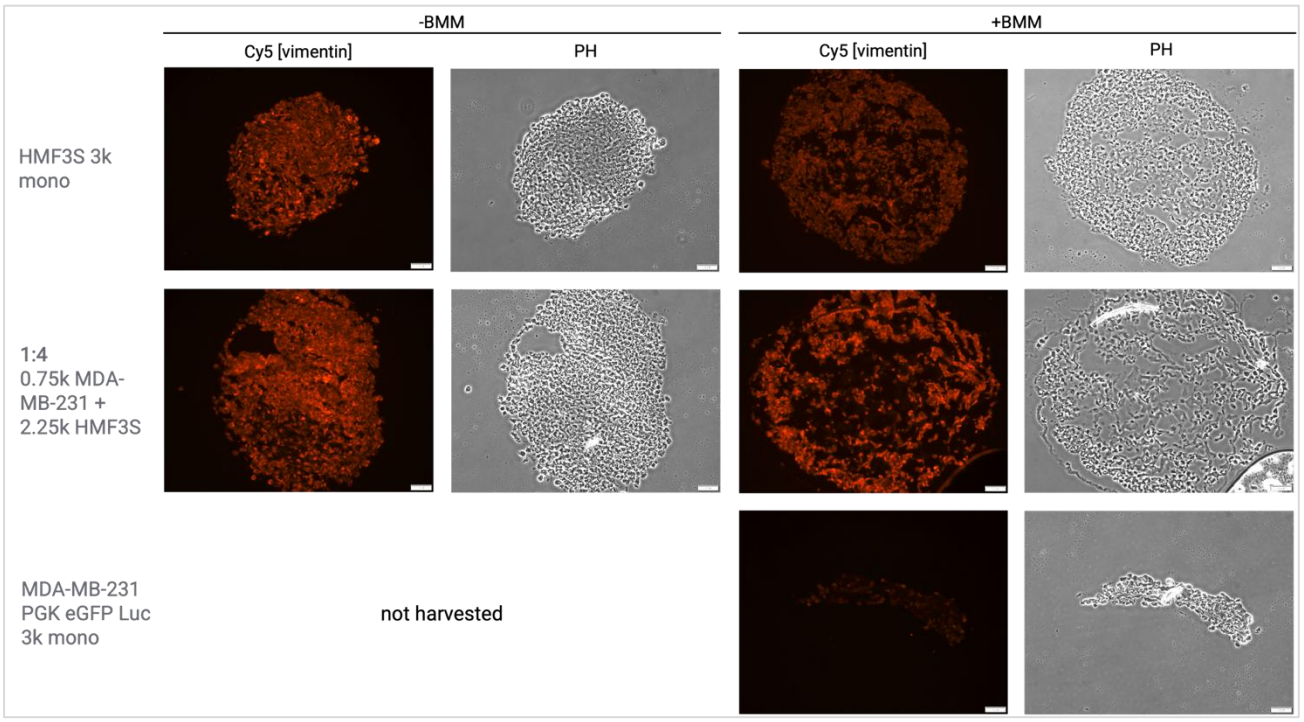

Figure 21. IHC staining of vimentin in sections of spheroids harvested on day 10. *Representative fluorescence microscopy (FLM) images and corresponding phase contrast (PH) images of mono- and co-cultures (at ratio 1:4) with and without BMM supplementation. Panels without images indicate samples that were not harvested. A Cy5 filter set was used to visualize vimentin and images were acquired using a 20x objective. Scale bar = 50 µm.*

Vimentin is a type III intermediate filament protein that is commonly associated with EMT and frequently used as a marker for mesenchymal cells such as fibroblasts. EMT represents a key biological process underlying tumor progression and metastasis and is characterized by the acquisition of a mesenchymal phenotype, which correlates with enhanced cellular motility and invasive potential.[79,80] The detection of vimentin across all culture conditions therefore suggests that its expression is not restricted to HMF3S cells in this model. This observation is consistent with previous studies reporting vimentin expression in MDA-MB-231 cells.[81,82] For example, Liu et al. demonstrated that MDA-MB-231 cells lose epithelial markers such as E-cadherin while exhibiting increased expression of mesenchymal markers including vimentin.[82] Additionally, this observation - the loss of E-cadherin and strong vimentin expression - supports the inability of MDA-MB-231 cells to form stable aggregates. Thus, while IHC staining for vimentin confirmed the presence of EMT-associated characteristics, it was not suitable for distinguishing between the two cell populations in this model.

8.4.2.4 Alpha smooth muscle actin (α-SMA)

To evaluate whether HMF3S cells acquire a CAF-like phenotype, IHC staining for α-SMA was

performed, as this marker is commonly associated with CAF activation. However, no distinct α-SMA signal could be detected in any of the analyzed cultures (**Figure 22** and **Figure 23**).

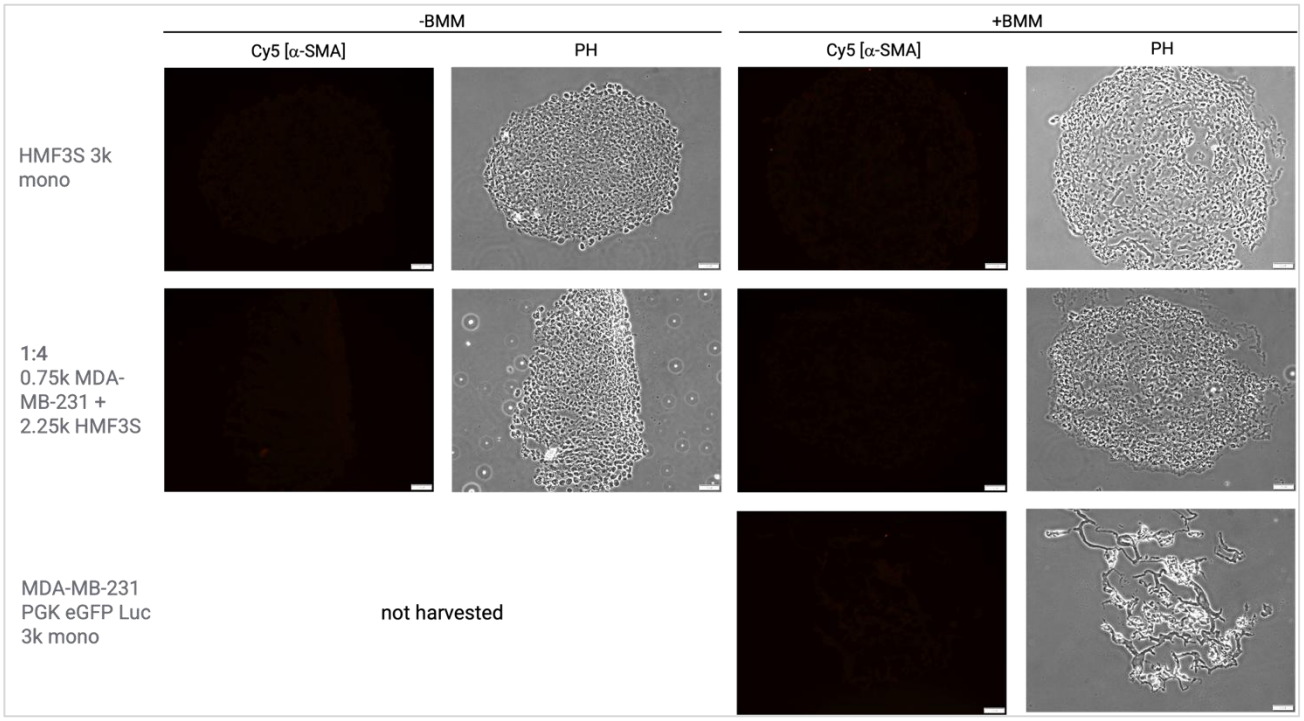

Figure 22. IHC staining of α-SMA in sections of spheroids harvested on day 7. *Representative fluorescence microscopy (FLM) images and corresponding phase contrast (PH) images of mono- and co-cultures (at ratio 1:4) with and without BMM supplementation. Panels without images indicate samples that were not harvested. A Cy5 filter set was used to visualize α-SMA and images were acquired using a 20x objective. Scale bar = 50 µm.*

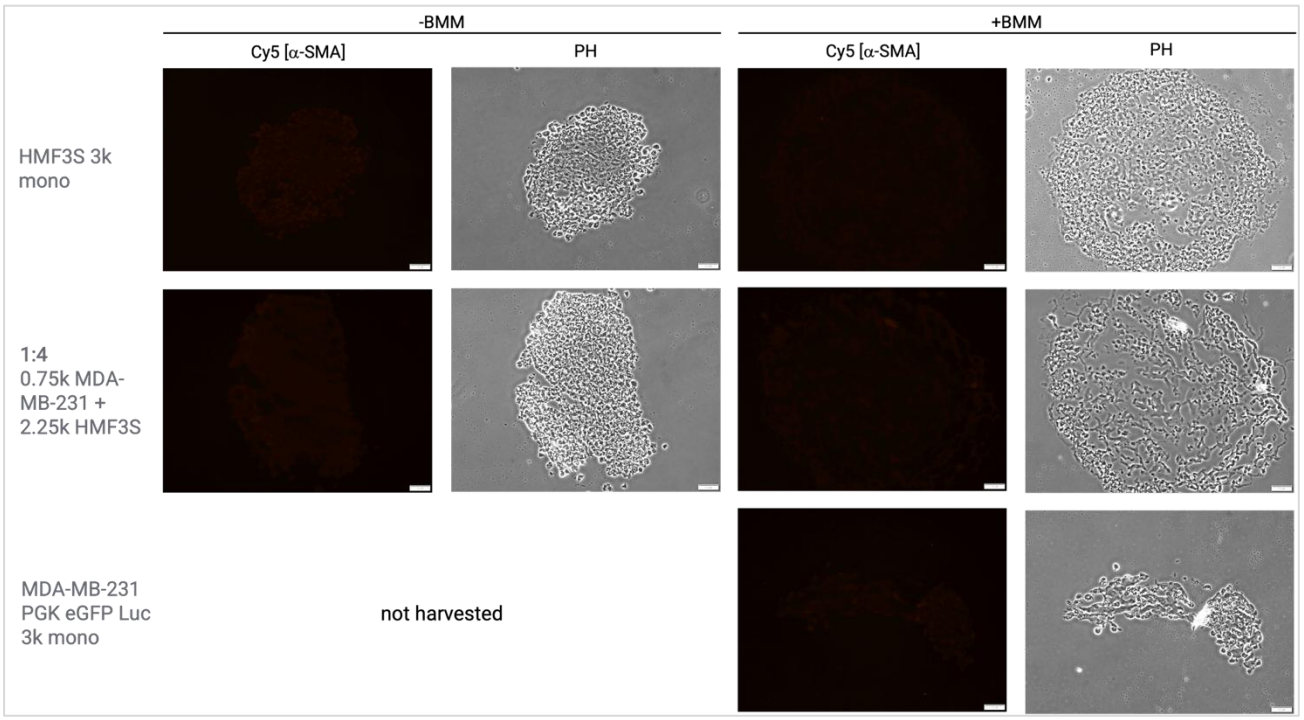

Figure 23. IHC staining of α-SMA in sections of spheroids harvested on day 10. *Representative fluorescence microscopy (FLM) images and corresponding phase contrast (PH) images of mono- and co-cultures (at ratio 1:4) with and without BMM supplementation. Panels without images indicate samples that were not harvested. A Cy5 filter set was used to visualize α-SMA and images were acquired using a 20x objective. Scale bar = 50 µm.*

The absence of a detectable α-SMA expression does not necessarily indicate that fibroblast activation did not occur. CAFs represent a highly heterogenous population and no single marker is universally expressed across all CAF subtypes.[83] A previous study has further suggested that the expression of α-SMA may depend on specific microenvironmental factors (such as TGF-β) that promote fibroblast activation.[45] Although TGF-β was supplemented in the culture medium, its effective concentration may not have been sufficient to fully induce fibroblast differentiation into CAFs, which could potentially explain the lack of detectable marker expression. Furthermore, CAF activation is a dynamic process and may decrease during prolonged culture periods in 3D models, potentially leading to reduced marker expression at later time points, as previously described by Romano et al.[84] Additionally, this antibody was purchased for this purpose and no positive control was available. Therefore, one must assure first the proper working of this antibody before final conclusions can be drawn.

8.5 Evaluation of spheroid composition

To evaluate the distribution of the two cell lines MDA-MB-231 PGK eGFP Luc and HMF3S

within multicellular spheroids, flow cytometry analysis was performed at two designated time points (day 3 and day 7). Alongside the co-culture conditions (ratio 1:3 and 1:4), monocultures of both cell lines were analyzed as controls. In contrast to previous experiments, only culture conditions without BMM supplementation were investigated. Representative phase contrast images of mono- and co-cultures from one out of three experiments are shown in **Figure 24** to illustrate the morphology of the different culture conditions prior to dissociation and subsequent FCM analysis, while images from additional replicates are provided in the Appendix (Figure 31 and Figure 32).

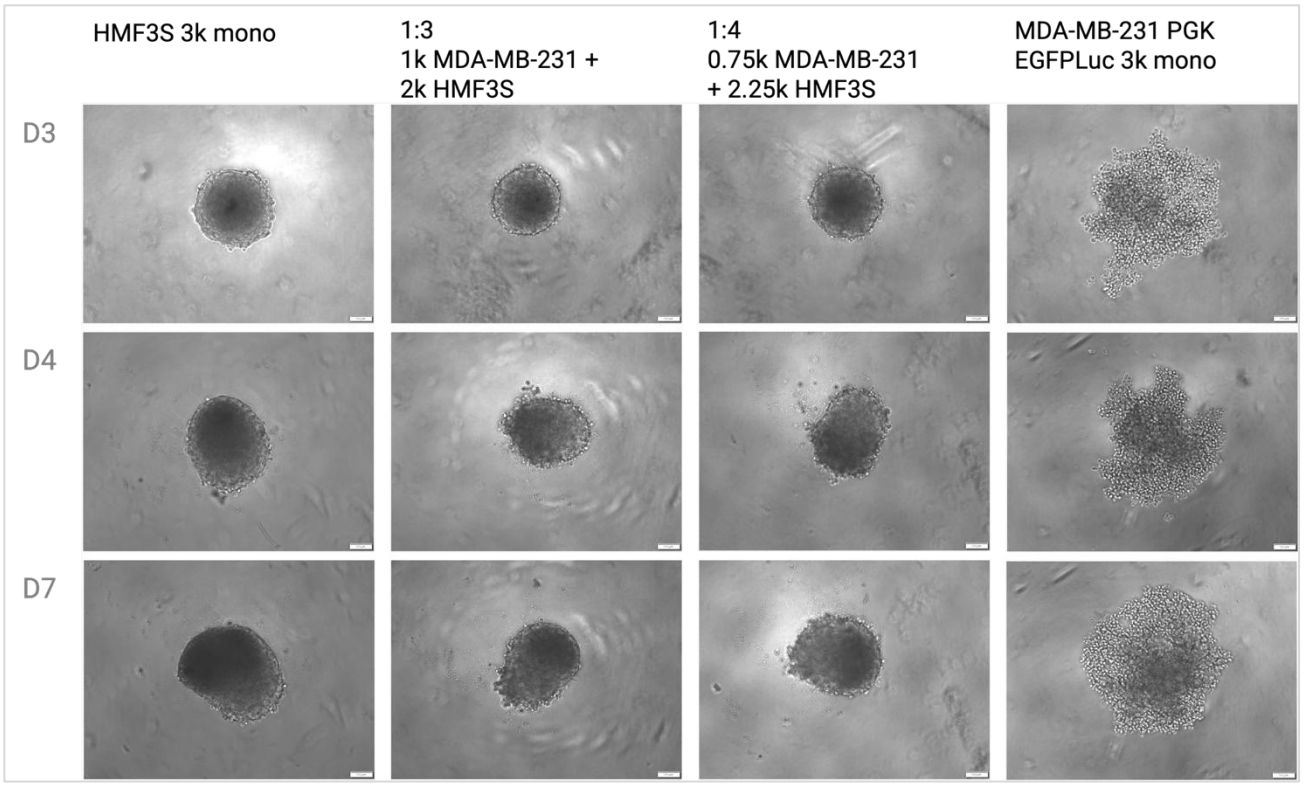

Figure 24. Representative phase contrast microscopy images of whole mono- and co-culture (ratio 1:3 and 1:4) spheroids and cellular aggregates *of MDA-MB-231 PGK eGFP Luc and HMF3S cells. Images are shown from the third independent experiment, while additional replicates are provided In the Appendix. Images were acquired at days 3, 4 and 7 using a 10x objective. Scale bar = 100 µm.*

The gating strategy applied for the analysis of counted cells at the seeding day is shown in Figure 25 and demonstrates the clear separation of eGFP+ and eGFP- cell populations. Across three independent experiments, each performed in triplicate, the proportion of eGFP+ MDA-MB-231 PGK eGFP Luc cells remained consistent, resulting in an average of 94.6 % eGFP positive MDA-MB-231 cells (n = 9). This value closely matched the proportion observed with the MDA-MB-231 monoculture at day 3 (live/MDA (eGFP+) = 94 %; Figure 30), indicating

a valid baseline control and supporting the reliability of the FCM-based analysis.

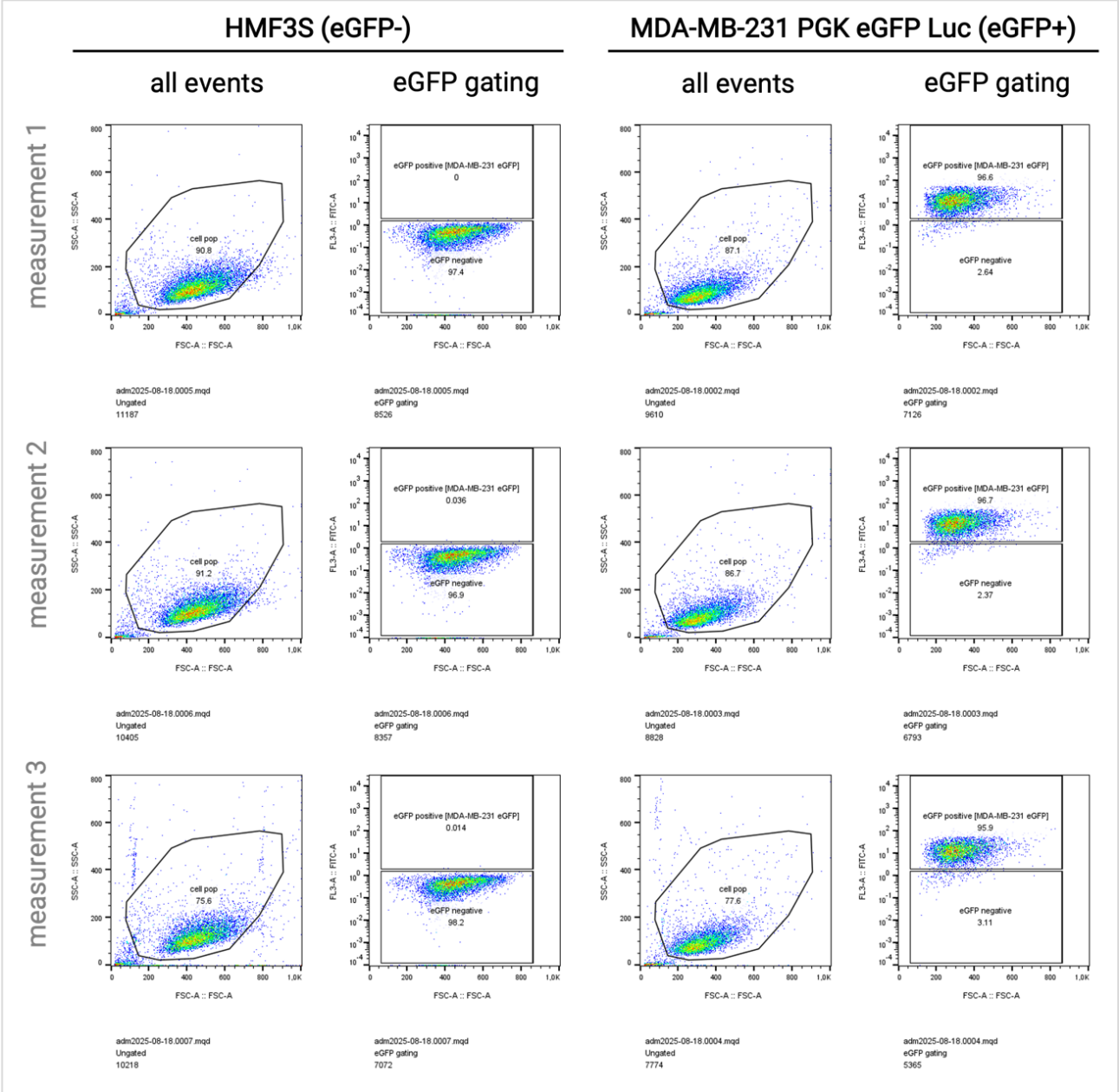

Figure 25. Gating strategy for the analysis of counted cells at the seeding day. *Representative plots of one of the three experiments illustrating the identification of eGFP+ and eGFP- cell populations in HMF3S and MDA-MB-231 PGK eGFP Luc cells at the seeding day.*

The gating strategy used for the analysis of mono- and co-culture samples at day 3 and 7 is shown in **Figure 26** and **Figure 27**, respectively. These plots illustrate the sequential gating approach, including the identification of live cells and the discrimination between eGFP+ and eGFP- populations. The same gating strategy was consistently applied to all experimental conditions.

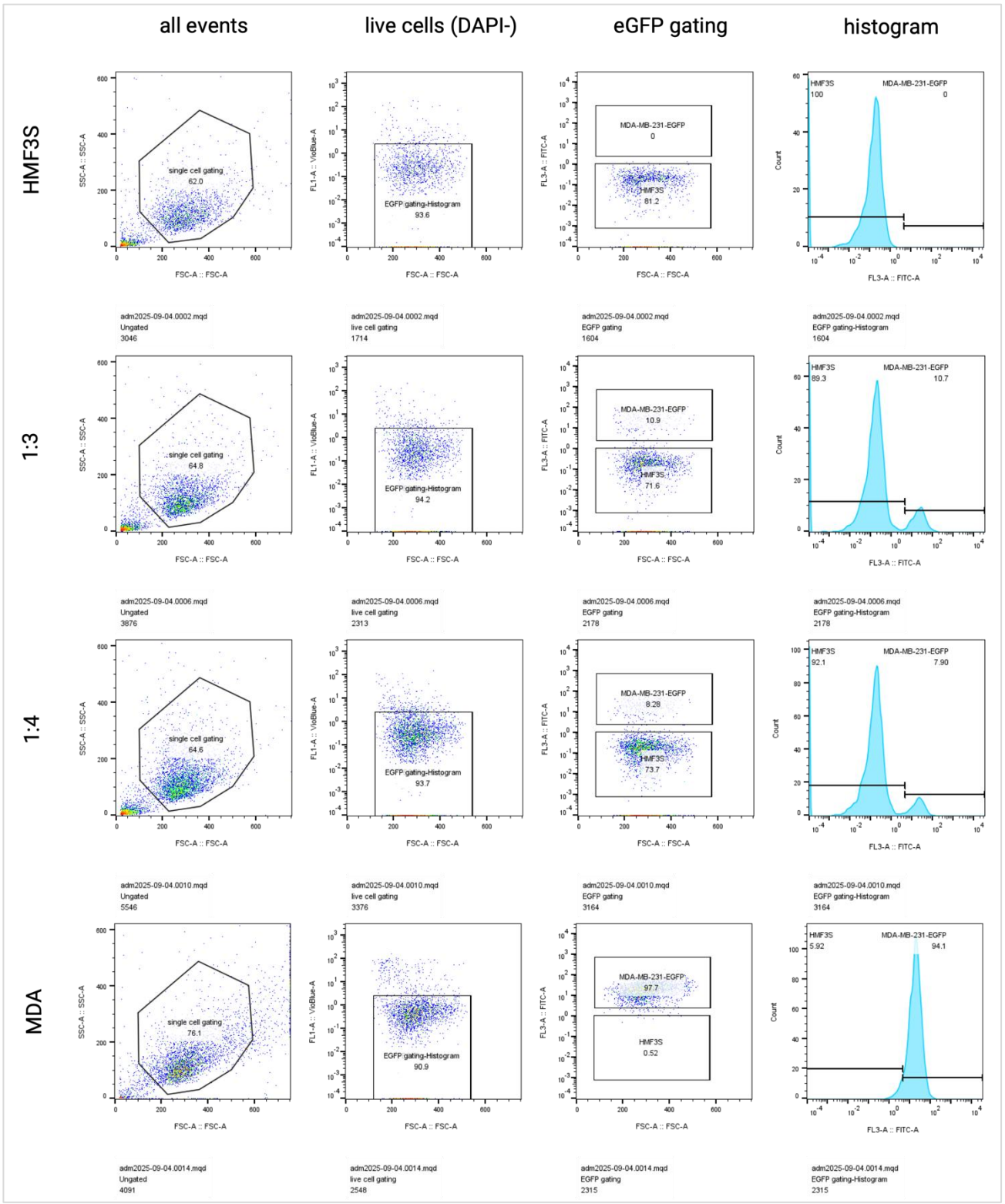

Figure 26. Sequential gating strategy applied to mono- and co-culture samples at day 3. *Representative plots of one of the three experiments include exclusion of debris (all events), identification of live cells (DAPI-) and discrimination between eGFP+ (upper gate) and eGFP- (lower gate) cells. The histogram further shows the distribution of eGFP+ and eGFP- populations, with distinct peaks corresponding to each population.*

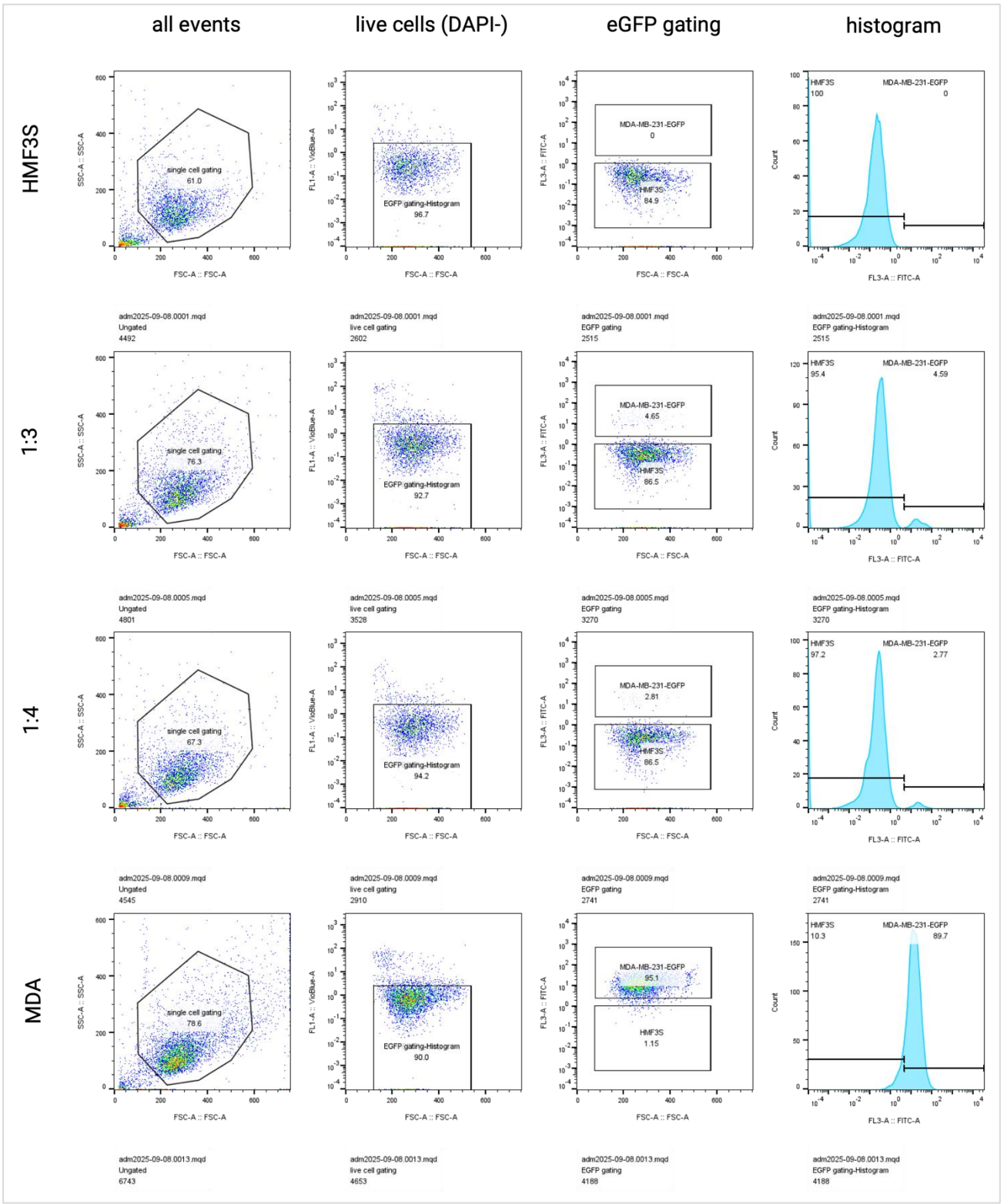

Figure 27. Sequential gating strategy applied to mono- and co-culture samples at day 7. *Representative plots of one of the three experiments include exclusion of debris (all events), identification of live cells (DAPI-) and discrimination between eGFP+ (upper gate) and eGFP- (lower gate) cells. The histogram further shows the distribution of eGFP+ and eGFP- populations, with distinct peaks corresponding to each population.*

Overlay histograms combining all experiments are shown in **Figure 28** and **Figure 29** and further confirm stable eGFP expression of MDA-MB-231 PGK eGFP Luc cells between the

seeding day and day 3. This supports the use of eGFP expression as a reliable parameter for distinguishing between the two cell lines and provides a valid baseline control for subsequent analyses. However, while eGFP expression remained stable at earlier timepoints, changes became apparent at the later read-out (day 7). Individual overlay histograms for each experiment are provided in the Appendix (**Figure 33**, **Figure 34** and **Figure 35**).

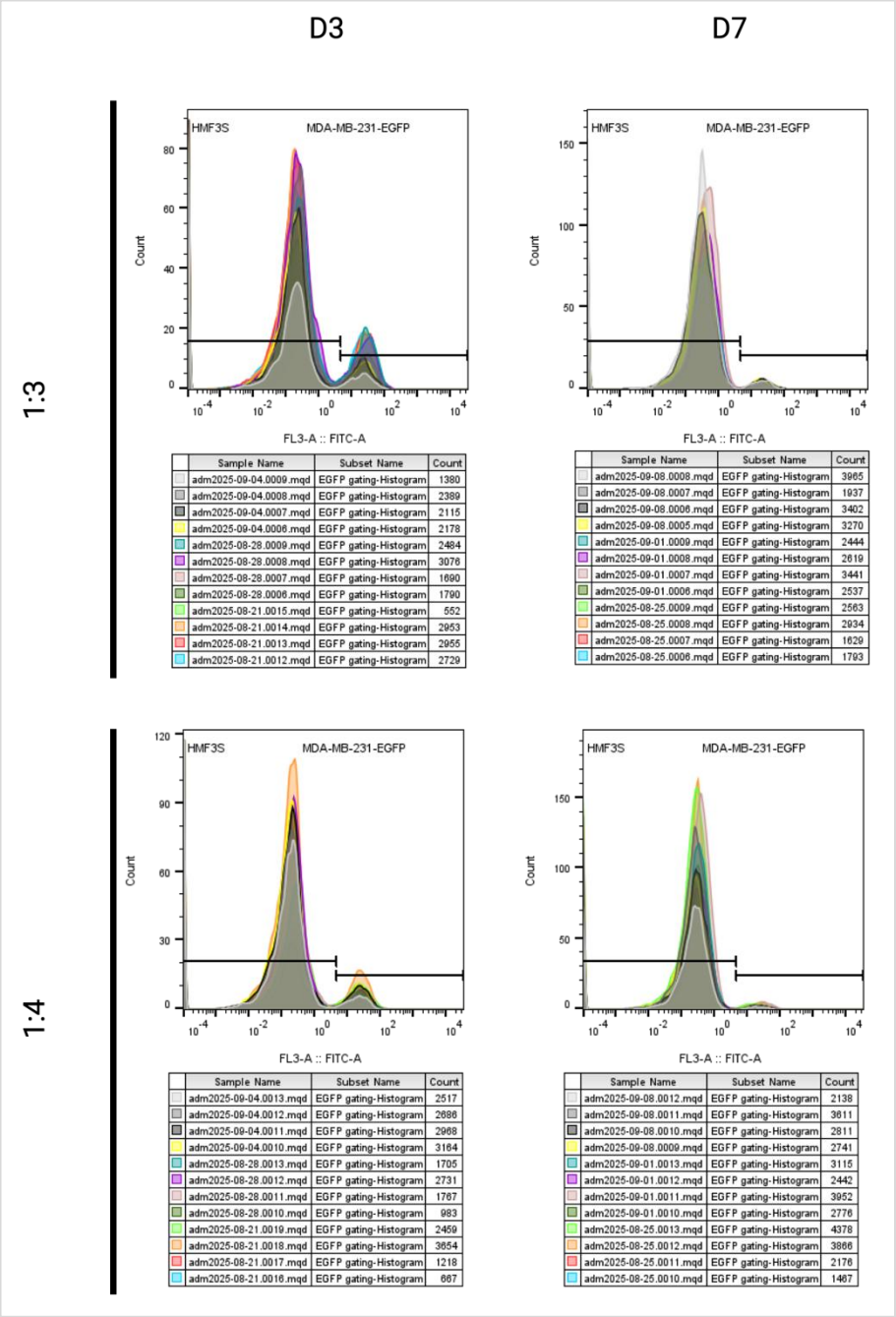

Figure 28. Histogram overlay of eGFP+ and eGFP- events in co-cultures of MDA-MB-231 PGK and HMF3S eGFP Luc *across all experiments and time points (days 3 and 7). Distinct peaks in co-cultures (1:3 and 1:4) represent eGFP+ (lower intensity) and eGFP- (higher intensity) cell populations. Data represent measurements with n = 12 for co-cultures at ratio 1:3 and 1:4 for each time point, respectively.*

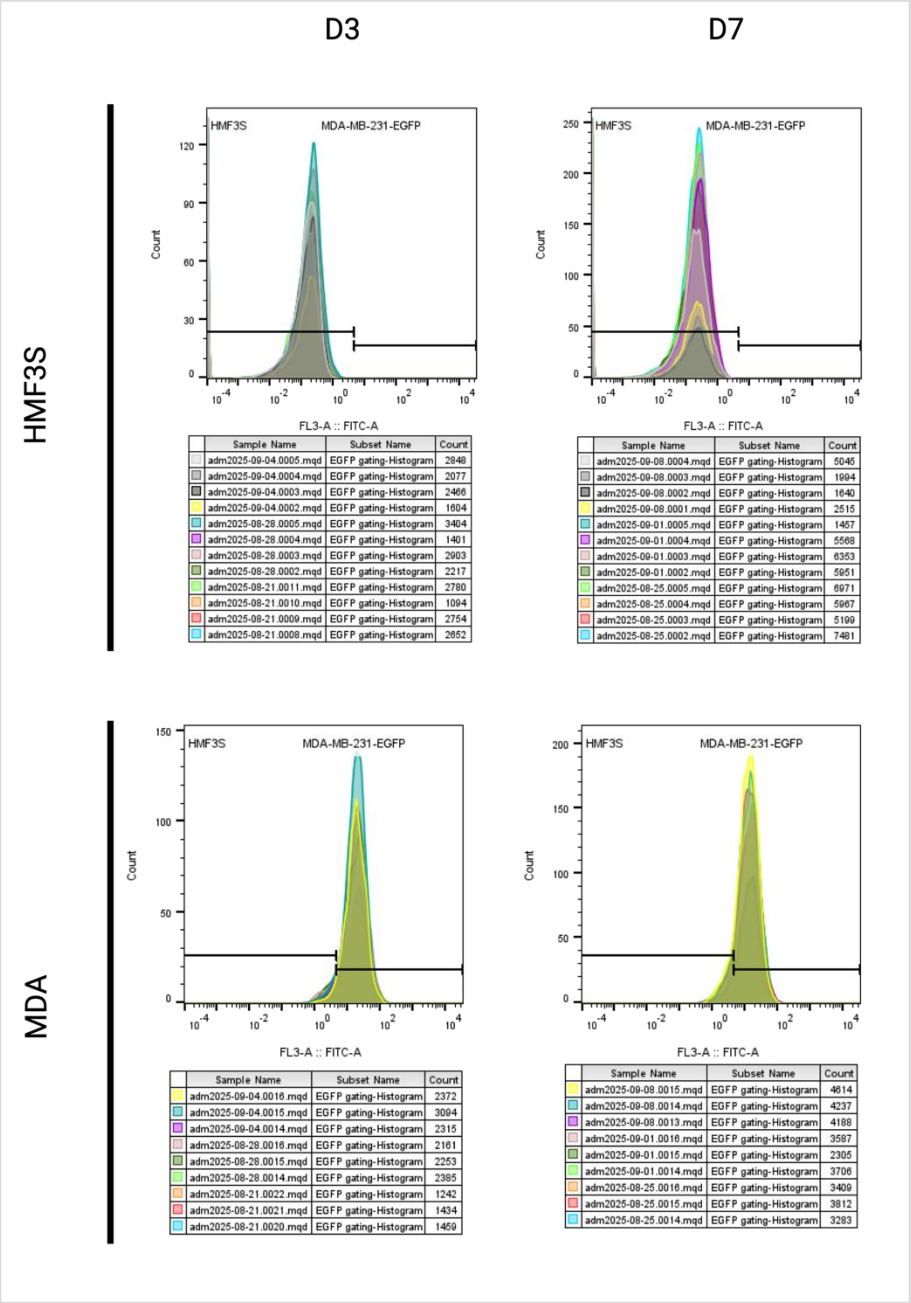

Figure 29. Histogram overlay of eGFP+ and eGFP- events in monocultures of HMF3S and MDA-MB-231 PGF eGFP Luc *across all experiments and time points (days 3 and 7). Data represent measurements with n = 12 (for HMF3S) and n = 9 (for MDA-MB-231 PGK eGFP Luc) for each time point, respectively.*

As mentioned above, at day 7, a decrease in the proportion of live MDA-MB-231 PGK eGFP Luc cells expressing eGFP was observed Figure 30. This may reflect an influence of the spheroid microenvironment on eGFP expression or changes in the proportion of MDA-MB-231 PGK eGFP Luc cells over time. As discussed in section **Fehler! Verweisquelle konnte nicht gefunden werden.**, one possible explanation for the reduced eGFP signal might be oxygen deprivation within the spheroid microenvironment, as chromophore formation is oxygen-dependent. In addition, limited oxygen availability may suppress overall translational

activity, leading to reduced synthesis of eGFP.[77] Therefore, a lower eGFP signal does not necessarily indicate a reduced number of MDA-MB-231 PGK eGFP Luc cells within the spheroid, especially considering that also with the MDA-MB-231 monoculture, which does not form stable spheroids, a decrease in eGFP positive cells could be observed.

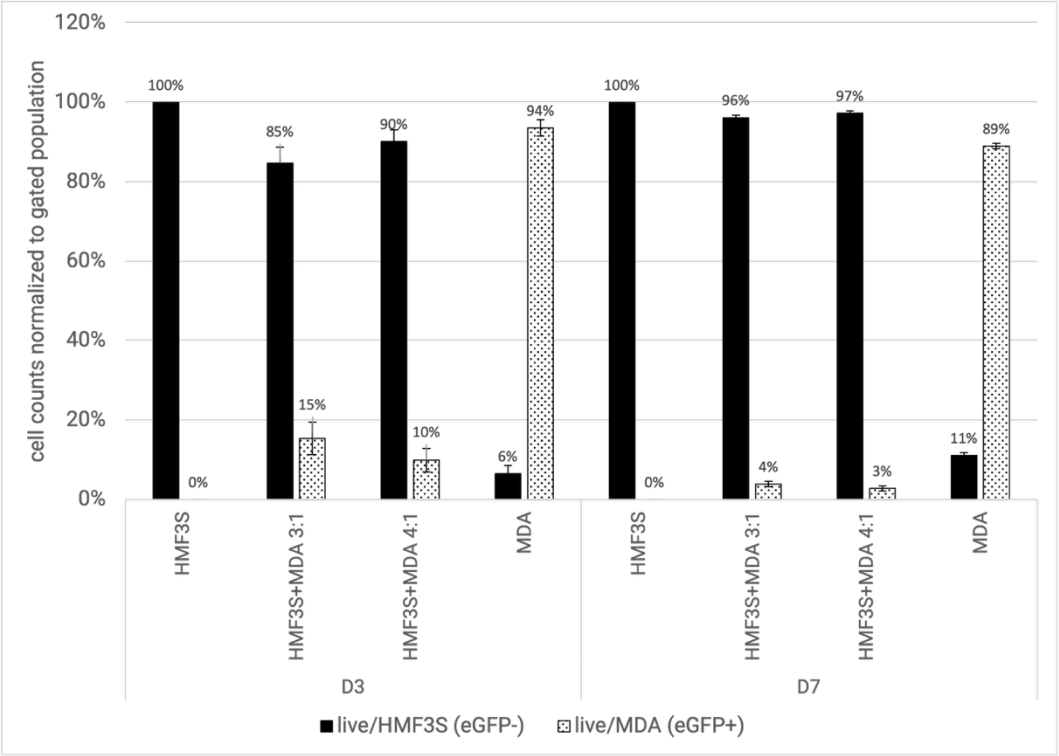

Figure 30. Flow cytometry based quantification of eGFP+ and eGFP- live cells at the respective read-out time points *(day 3 and day 7). Data are presented as the percentage of cells normalized to the gated population. Bars represent mean values ± standard deviation (SD) with n = 12 (for HMF3S, co-cultures at ratio 1:3 and 1:4) and n = 9 (for MDA-MB-231 PGK eGFP Luc), respectively.*

Additional supporting data, including analyses of cell populations and total live cell counts, are provided in the Appendix (Figure 36 and Figure 37). Overall, these results suggest that flow cytometry is a suitable method to assess the distribution eGFP+ and eGFP- populations within co-culture spheroids and reveal temporal changes in eGFP expression of MDA-MB-231 PGK eGFP Luc cells. However, while eGFP+ and eGFP- populations can be distinguished, interpretation about precise proportional changes between the two cell lines (HMF3S and MDA-MB-231 PGK eGFP Luc) should be made with caution, as eGFP expression is oxygen-dependent and therefore does not necessarily reflect an actual decrease of MDA-MB-231 PGK eGFP Luc cells.

9 Conclusion

The present study aimed to establish and characterize multicellular spheroids of MDA-MB-231 and HMF3S cells as physiologically relevant in vitro models for TNBC.

Overall, the results demonstrate that the choice of seeding conditions and medium supplementation with BMM critically influences spheroid formation, growth behavior and structural organization. While spheroids cultured in the presence of BMM exhibited increased metabolic activity and growth dynamics, they were also associated with higher variability and limited reproducibility in the metabolic activity assay, especially MDA-MB-231 monocultures supplemented with BMM. Notably, monocultures of MDA-MB-231 cells did not form stable spheroids under the tested conditions, neither with nor without BMM supplementation in the medium.

Importantly, the observation of more pronounced necrotic cores and densely packed structures in mono- and co-cultures without BMM supplementation may not represent a disadvantage but rather a physiologically relevant feature, as central necrosis is a hallmark of solid tumors in vivo.

IHC analyses provided insights into spheroid characteristics but were limited in their ability to reliably distinguish between MDA-MB-231 and HMF3S cell populations. While Ki-67 enabled the assessment of proliferative activity, eGFP showed insufficient signal intensity and vimentin lacked specificity, as it was expressed across both cell lines. The absence of detectable α-SMA expression might not necessarily indicate a lack of HMF3S activation into CAFs but may instead be due to context-dependent marker expression and technical limitations. Further experiments testing the reliability of the used antibody would be needed. In addition, the lack of a consistent DAPI signal as a nuclear counterstain restricted precise spatial interpretation, although qualitative evaluation of marker-associated fluorescence remained mostly feasible.

Flow cytometry-based analysis proved to be a suitable approach for assessing the distribution of eGFP+ and eGFP- populations within co-culture spheroids and for detecting temporal changes in eGFP expression. However, interpretation regarding a precise discrimination between MDA-MB-231 and HMF3S cells should be made with caution, as the oxygen-dependent expression of eGFP may not necessarily reflect actual changes in the composition of the two cell lines. Despite this limitation, flow cytometry provides a solid basis for future studies, particularly for investigating changes in cell populations under

varying experimental conditions.

Taken together, the results of this study suggest that balancing physiological relevance and experimental reproducibility is an important consideration in the development of spheroid models. Future work should focus on further optimization of co-culture stability, refining marker selection and integrating complementary analytical approaches to enable a more precise characterization of co-culture spheroids.

10 Appendix

10.1 Growth assessment

10.1.1 Metabolic activity assay

Table 16. Number of replicates (n) per experimental condition in the metabolic activity assay.

	monoculture		**co-culture**
	3k HMF3S (-BMM/+BMM)	**3k MDA-MB-231 (-BMM/+BMM)**	**1:3 and 1:4 MDA:HMF3S (-BMM/+BMM)**
Day 3 (D3)	8	7 / 8	10
Day 7 (D7)	15	11 / 15	15
Day 10 (D10)	15	7 / 15	15

10.1.2 Size analysis

Table 17. Number of replicates (n) per experimental condition included in the size analysis.

	monoculture		**co-culture**
	3k HMF3S (-BMM/+BMM)	**3k MDA-MB-231 (-BMM/+BMM)**	**1:3 and 1:4 MDA:HMF3S (-BMM/+BMM)**
Day 3 (D3)	14	14 / 13	14
Day 7 (D7)	13	8 / 14	14
Day 10 (D10)	13 / 12	6 / 13	14

10.2 Evaluation of spheroid composition

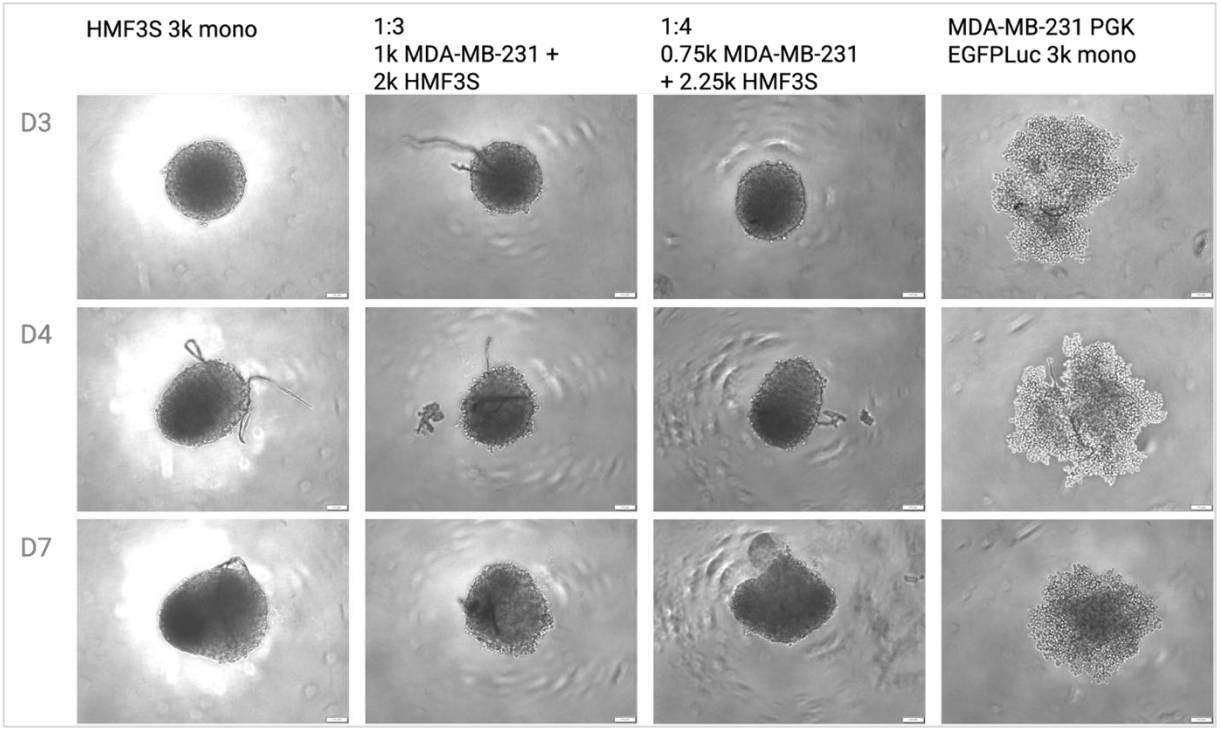

Figure 31. Representative phase contrast microscopy images of whole mono- and co-culture (ratio 1:3 and 1:4) spheroids and cellular aggregates *of MDA-MB-231 PGK eGFP Luc and HMF3S cells. Images are shown from the first independent experiment and were acquired at days 3, 4 and 7 using a 10x objective. Scale bar = 100 µm.*

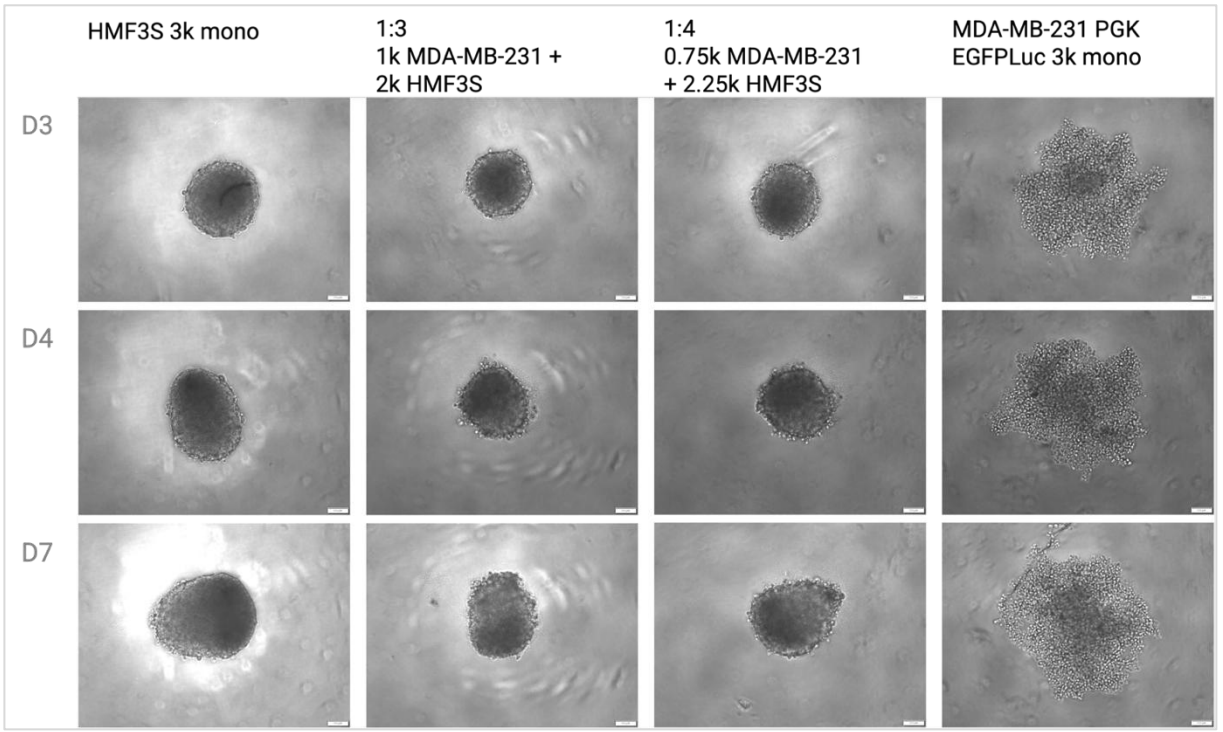

Figure 32. Representative phase contrast microscopy images of whole mono- and co-culture (ratio 1:3 and 1:4) spheroids and cellular aggregates *of MDA-MB-231 PGK eGFP Luc and HMF3S cells. Images are shown from the second independent experiment and were acquired at days 3, 4 and 7 using a 10x objective. Scale bar = 100 µm.*

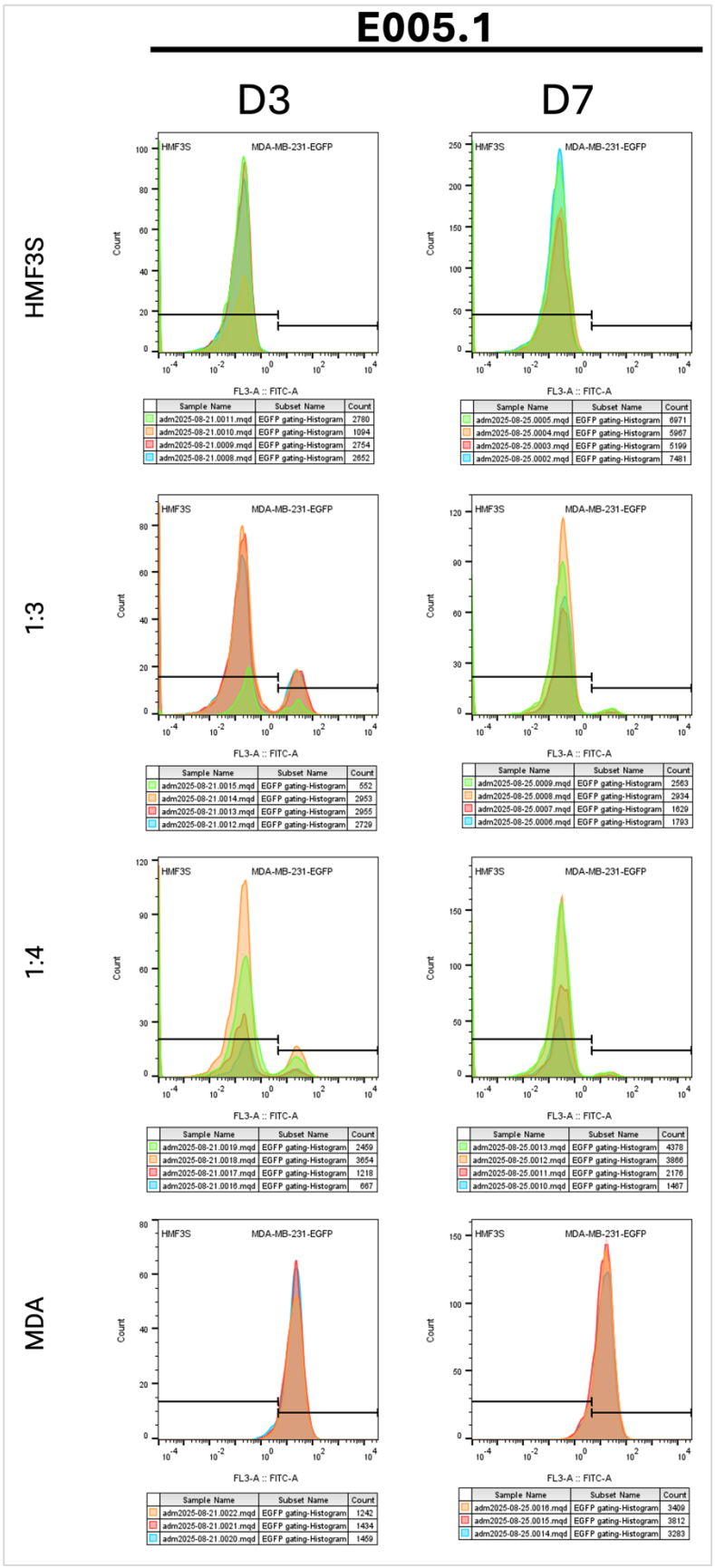

Figure 33. Individual overlay histograms of eGFP+ and eGFP- populations for the first out of 3 independent flow cytometry experiments (E005.1). *Distinct peaks in co-cultures (1:3 and 1:4) represent eGFP+ (lower intensity) and eGFP- (higher intensity) cell populations. Data are shown for each experimental condition and time point, with n = 4 for HMF3S, co-culture samples at ratio 1:3 and 1:4, and n = 3 for MDA-MB-231 PGK eGFP Luc.*

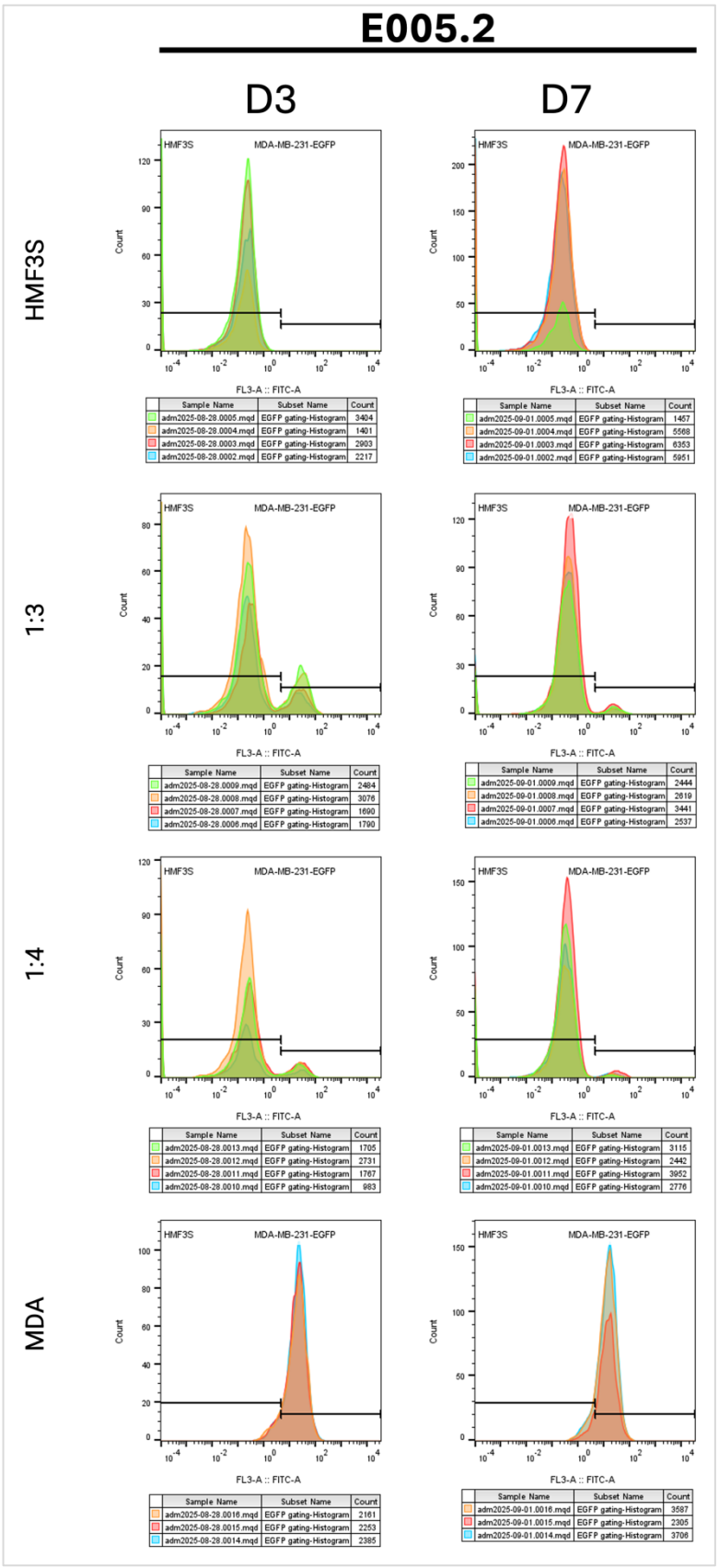

Figure 34. Individual overlay histograms of eGFP+ and eGFP- populations for the second out of 3 independent flow cytometry experiments (E005.2). *Distinct peaks in co-cultures (1:3 and 1:4) represent eGFP+ (lower intensity) and eGFP- (higher intensity) cell populations. Data are shown for each experimental condition and time point, with n = 4 for HMF3S, co-culture samples at ratio 1:3 and 1:4, and n = 3 for MDA-MB-231 PGK eGFP Luc.*

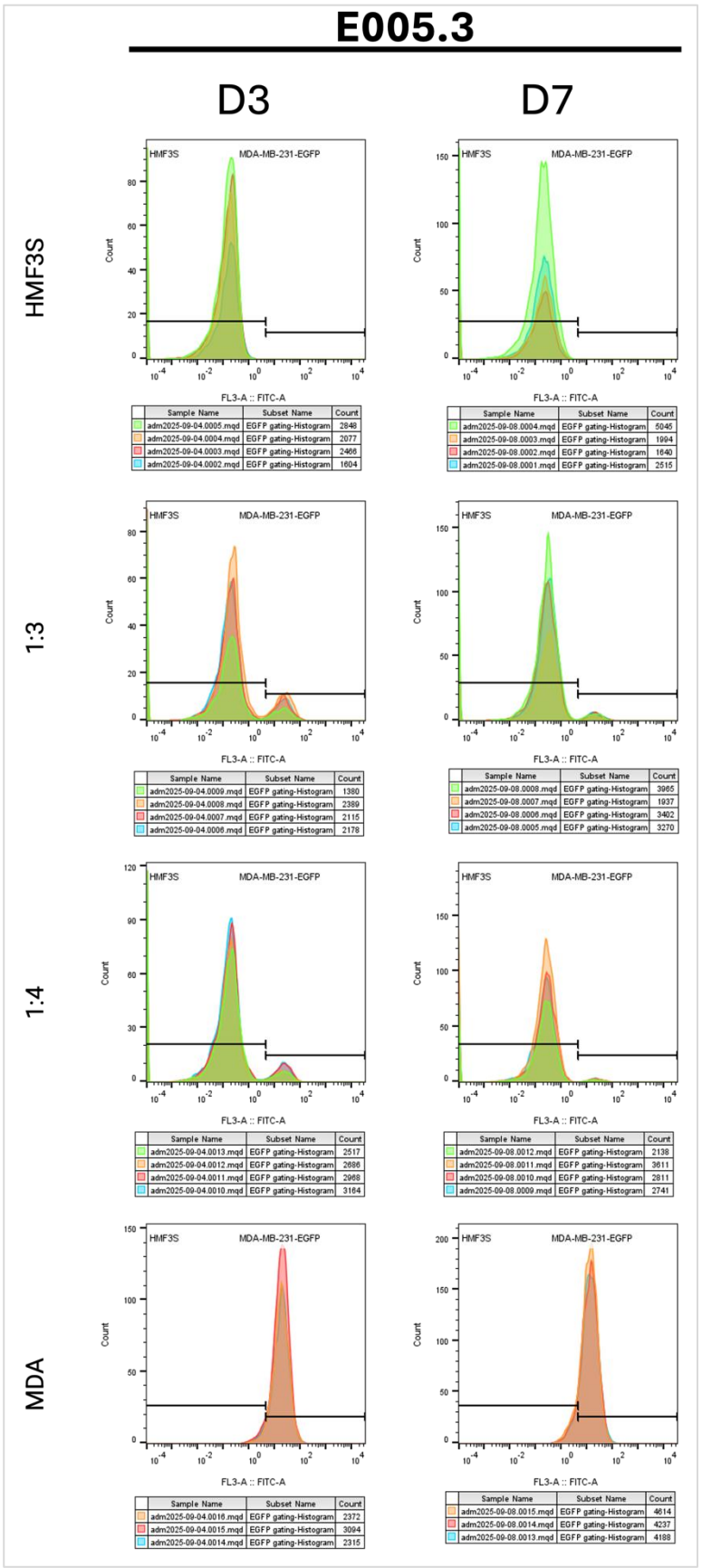

Figure 35. Individual overlay histograms of eGFP+ and eGFP- populations for the third out of 3 independent flow cytometry experiments (E005.3). *Distinct peaks in co-cultures (1:3 and 1:4) represent eGFP+ (lower intensity) and eGFP- (higher intensity) cell populations. Data are shown for each experimental condition and time point, with n = 4 for HMF3S, co-culture samples at ratio 1:3 and 1:4, and n = 3 for MDA-MB-231 PGK eGFP Luc.*

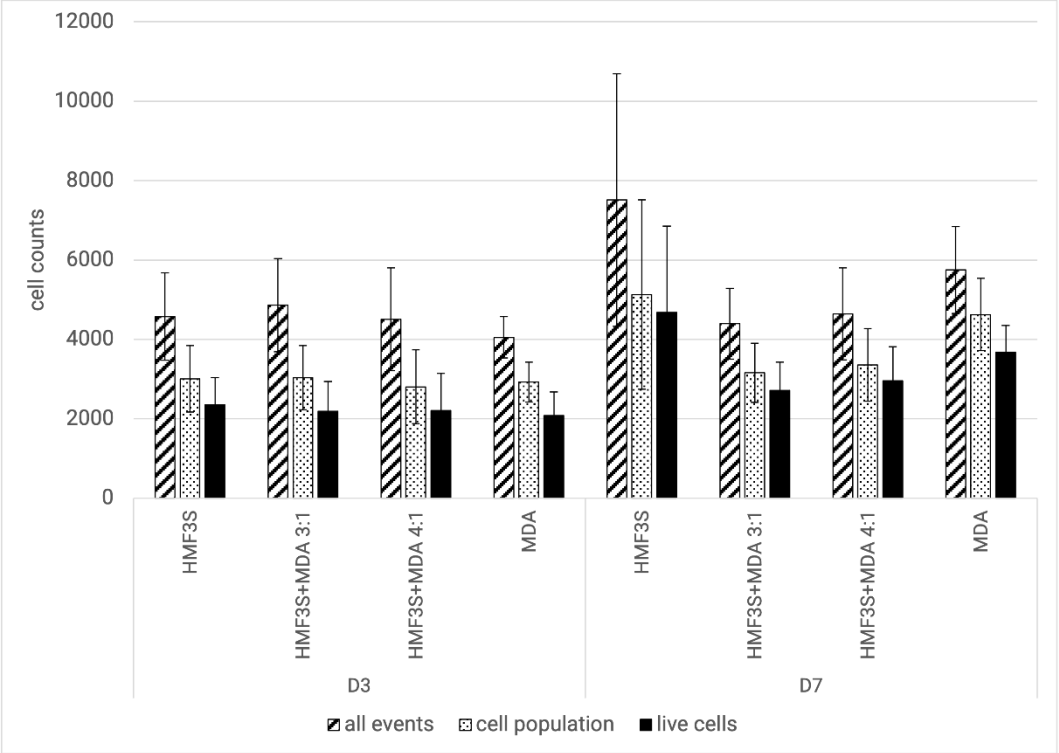

Figure 36. Flow cytometry based quantification of absolute cell counts across experimental conditions at both read-out time points *(day 3 and day 7). Bar charts show the number of all events, gated cell populations and live cells for each condition. Data are presented as mean values ± standard deviation (SD) and are displayed as absolute cell counts. Measurements were obtained from three independent experiments, with n = 12 for HMF3S, co-culture samples at ration 1:3 and 1:4, and n = 9 for MDA-MB-231 PGK eGFP Luc.*

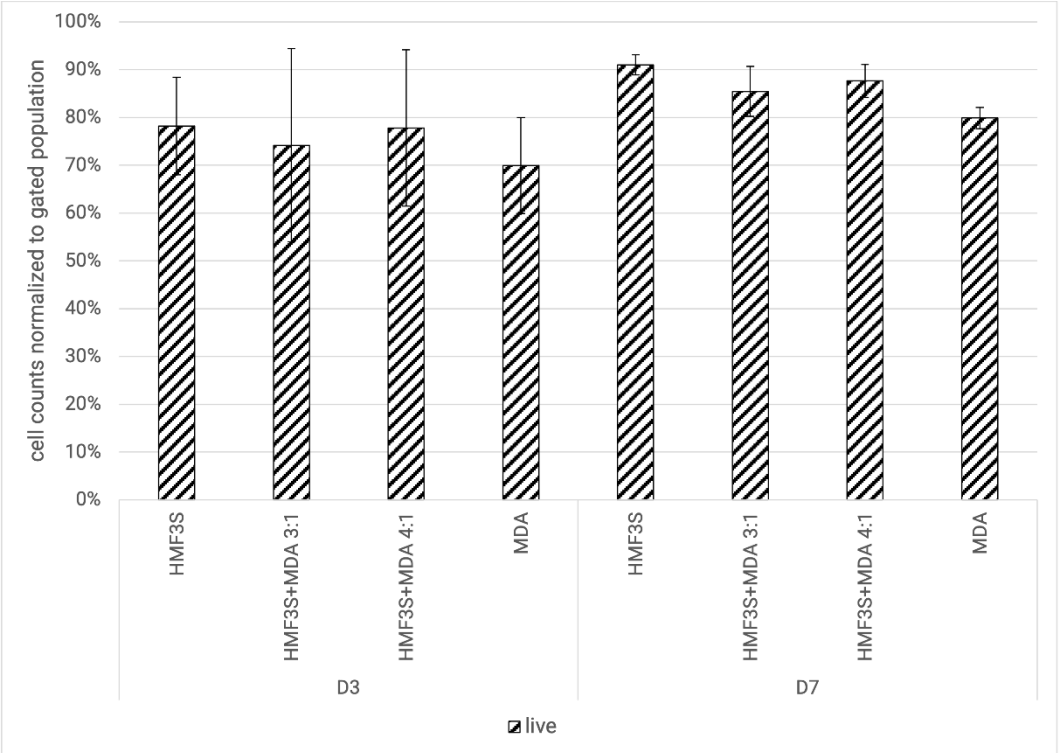

Figure 37. Flow cytometry based quantification of live cells across experimental conditions at both read-out time points *(day 3 and day 7). Bar charts show the percentage of live cells for each condition. Data are presented as mean values ± standard deviation (SD) and are normalized to the gated cell population. Measurements were obtained from three independent experiments, with n = 12 for HMF3S, co-culture samples at ration 1:3 and 1:4, and n = 9 for MDA-MB-231 PGK eGFP Luc.*

11 List of figures

12 List of tables

13 References

1. World Health Organization. Cancer. World Health Organization. Accessed 24.03.2026, https://www.who.int/en/news-room/fact-sheets/detail/cancer

2. Schwartz SM. Epidemiology of Cancer. *Clinical Chemistry*. 2024;70(1):140-149. doi:10.1093/clinchem/hvad202

3. Hanahan D, Weinberg RA. The hallmarks of cancer. *Cell*. Jan 7 2000;100(1):57-70. doi:10.1016/s0092-8674(00)81683-9

4. Hanahan D, Weinberg RA. Hallmarks of cancer: the next generation. *Cell*. Mar 4 2011;144(5):646-74. doi:10.1016/j.cell.2011.02.013

5. Garcia-Sancha N, Corchado-Cobos R, Perez-Losada J. Understanding Susceptibility to Breast Cancer: From Risk Factors to Prevention Strategies. *Int J Mol Sci*. Mar 25 2025;26(7)doi:10.3390/ijms26072993

6. World Health Organization. Breast cancer. World Health Organization. Accessed 24.03.2026, https://www.who.int/news-room/fact-sheets/detail/breast-cancer

7. Scully OJ, Bay BH, Yip G, Yu Y. Breast cancer metastasis. *Cancer Genomics Proteomics*. Sep-Oct 2012;9(5):311-20.

8. Yersal O, Barutca S. Biological subtypes of breast cancer: Prognostic and therapeutic implications. *World J Clin Oncol*. Aug 10 2014;5(3):412-24. doi:10.5306/wjco.v5.i3.412

9. Gao JJ, Swain SM. Luminal A Breast Cancer and Molecular Assays: A Review. *Oncologist*. May 2018;23(5):556-565. doi:10.1634/theoncologist.2017-0535

10. Breastcancer.org. Molecular Subtypes of Breast Cancer. Accessed 30.03.2026, https://www.breastcancer.org/types/molecular-subtypes

11. Olvera-Valencia M, Garcia-Castillo V, Ramos-Payan R, et al. Development of a reliable method for human triple-negative breast cancer organotypic culture: Improving imaging and genomic studies in 3D cultures. *J Tissue Eng*. Jan-Dec 2025;16:20417314251326668. doi:10.1177/20417314251326668

12. Asghari H, Kbari-Birgani S. Fibroblast Modulation of Invasion and Chemoresistance in Triple-Negative Breast Cancer: Insights from a Two-Cell Organoid Model. *Acta Biochimica Iranica*. 09/06 2025;doi:10.18502/abi.v3i2.19486

13. So JY, Ohm J, Lipkowitz S, Yang L. Triple negative breast cancer (TNBC): Non-genetic tumor heterogeneity and immune microenvironment: Emerging treatment options. *Pharmacol Ther*. Sep 2022;237:108253. doi:10.1016/j.pharmthera.2022.108253

14. Franchi-Mendes T, Eduardo R, Domenici G, Brito C. 3D Cancer Models: Depicting Cellular Crosstalk within the Tumour Microenvironment. *Cancers (Basel)*. Sep 14 2021;13(18)doi:10.3390/cancers13184610

15. Guo Z, Zhu Z, Lin X, et al. Tumor microenvironment and immunotherapy for triple-negative breast cancer. *Biomark Res*. Dec 31 2024;12(1):166. doi:10.1186/s40364-024-00714-6

16. Holliday DL, Speirs V. Choosing the right cell line for breast cancer research. *Breast Cancer Res*. Aug 12 2011;13(4):215. doi:10.1186/bcr2889

17. Naderi R, Gholizadeh-Ghaleh Aziz S, Haghigi-Asl AS. Evaluating the effect of Alantolactone on the expression of N-cadherin and Vimentin genes effective in epithelial-mesenchymal transition (EMT) in breast cancer cell line (MDA-MB-231). *Ann Med Surg (Lond)*. Jan 2022;73:103240. doi:10.1016/j.amsu.2021.103240

18. Kwon S, Han SJ, Kim KS. Differential response of MDA-MB-231 breast cancer and MCF10A normal breast cells to cytoskeletal disruption. *Oncol Rep*. Nov 2023;50(5)doi:10.3892/or.2023.8637

19. Huang Z, Yu P, Tang J. Characterization of Triple-Negative Breast Cancer MDA-MB-231 Cell Spheroid Model. *Onco Targets Ther*. 2020;13:5395-5405. doi:10.2147/OTT.S249756

20. Ortiz-Montero P, Londono-Vallejo A, Vernot JP. Senescence-associated IL-6 and IL-8 cytokines induce a self- and cross-reinforced senescence/inflammatory milieu strengthening tumorigenic capabilities in the MCF-7 breast cancer cell line. *Cell Commun Signal*. May 4 2017;15(1):17. doi:10.1186/s12964-017-0172-3

21. Zibara K, Awada Z, Dib L, et al. Anti-angiogenesis therapy and gap junction inhibition reduce MDA-MB-231 breast cancer cell invasion and metastasis in vitro and in vivo. *Sci Rep*. Jul 28 2015;5:12598. doi:10.1038/srep12598

22. Dominguez-Cejudo MA, Gil-Torralvo A, Cejuela M, Molina-Pinelo S, Salvador Bofill J. Targeting the Tumor Microenvironment in Breast Cancer: Prognostic and Predictive Significance and Therapeutic Opportunities. *Int J Mol Sci*. Nov 26 2023;24(23)doi:10.3390/ijms242316771

23. Moura T, Laranjeira P, Caramelo O, Gil AM, Paiva A. Breast Cancer and Tumor Microenvironment: The Crucial Role of Immune Cells. *Curr Oncol*. Feb 28 2025;32(3)doi:10.3390/curroncol32030143

24. Hu D, Li Z, Zheng B, et al. Cancer-associated fibroblasts in breast cancer: Challenges and opportunities. *Cancer Commun (Lond)*. May 2022;42(5):401-434. doi:10.1002/cac2.12291

25. Hou SY, Macfarlane SC, Gomez Torijano A, et al. Cancer-Associated Fibroblasts Move and Interact More with Triple-Negative Breast Cancer Cells and Stimulate Their Proliferation in a Hyaluronan-Dependent Manner. *Cells*. Oct 23 2025;14(21)doi:10.3390/cells14211663

26. Levental KR, Yu H, Kass L, et al. Matrix crosslinking forces tumor progression by enhancing integrin signaling. *Cell*. Nov 25 2009;139(5):891-906. doi:10.1016/j.cell.2009.10.027

27. Yuan ZY, Luo RZ, Peng RJ, Wang SS, Xue C. High infiltration of tumor-associated macrophages in triple-negative breast cancer is associated with a higher risk of distant metastasis. *Onco Targets Ther*. 2014;7:1475-80. doi:10.2147/OTT.S61838

28. Kundu M, Butti R, Panda VK, et al. Modulation of the tumor microenvironment and mechanism of immunotherapy-based drug resistance in breast cancer. *Mol Cancer*. May 7 2024;23(1):92. doi:10.1186/s12943-024-01990-4

29. Sarkar T, Dhar S, Sa G. Tumor-infiltrating T-regulatory cells adapt to altered metabolism to promote tumor-immune escape. *Curr Res Immunol*. 2021;2:132-141. doi:10.1016/j.crimmu.2021.08.002

30. Otterlei Fjortoft M, Huse K, Rye IH. The Tumor Immune Microenvironment in Breast Cancer Progression. *Acta Oncol*. May 23 2024;63:359-367. doi:10.2340/1651-226X.2024.33008

31. Elayat G, Selim A. Angiogenesis in breast cancer: insights and innovations. *Clin Exp Med*. Aug 6 2024;24(1):178. doi:10.1007/s10238-024-01446-5

32. de Heer EC, Jalving M, Harris AL. HIFs, angiogenesis, and metabolism: elusive enemies in breast cancer. *J Clin Invest*. Oct 1 2020;130(10):5074-5087. doi:10.1172/JCI137552

33. Saha T, Solomon J, Samson AO, Gil-Henn H. Invasion and Metastasis as a Central Hallmark of Breast Cancer. *J Clin Med*. Aug 8 2021;10(16)doi:10.3390/jcm10163498

34. Fico F, Santamaria-Martinez A. The Tumor Microenvironment as a Driving Force of Breast Cancer Stem Cell Plasticity. *Cancers (Basel)*. Dec 21 2020;12(12)doi:10.3390/cancers12123863

35. Park M, Kim D, Ko S, Kim A, Mo K, Yoon H. Breast Cancer Metastasis: Mechanisms and Therapeutic Implications. *Int J Mol Sci*. Jun 18 2022;23(12)doi:10.3390/ijms23126806

36. Sahai E, Astsaturov I, Cukierman E, et al. A framework for advancing our understanding of cancer-associated fibroblasts. *Nat Rev Cancer*. Mar 2020;20(3):174-186. doi:10.1038/s41568-019-0238-1

37. Zheng J, Hao H. The importance of cancer-associated fibroblasts in targeted therapies and drug resistance in breast cancer. *Front Oncol*. 2023;13:1333839. doi:10.3389/fonc.2023.1333839

38. Sarkar M, Nguyen T, Gundre E, et al. Cancer-associated fibroblasts: The chief architect in the tumor microenvironment. *Front Cell Dev Biol*. 2023;11:1089068. doi:10.3389/fcell.2023.1089068

39. Singh S, Tran S, Putman J, Tavana H. Three-dimensional models of breast cancer-fibroblasts interactions. *Exp Biol Med (Maywood)*. May 2020;245(10):879-888. doi:10.1177/1535370220917366

40. Geng X, Chen H, Zhao L, et al. Cancer-Associated Fibroblast (CAF) Heterogeneity and Targeting Therapy of CAFs in Pancreatic Cancer. *Front Cell Dev Biol*. 2021;9:655152. doi:10.3389/fcell.2021.655152

41. Ohlund D, Handly-Santana A, Biffi G, et al. Distinct populations of inflammatory fibroblasts and myofibroblasts in pancreatic cancer. *J Exp Med*. Mar 6 2017;214(3):579-596. doi:10.1084/jem.20162024

42. Yakavets I, Francois A, Benoit A, Merlin JL, Bezdetnaya L, Vogin G. Advanced co-culture 3D breast cancer model for investigation of fibrosis induced by external stimuli: optimization study. *Sci Rep*. Dec 4 2020;10(1):21273. doi:10.1038/s41598-020-78087-7

43. O'Hare MJ, Bond J, Clarke C, et al. Conditional immortalization of freshly isolated human mammary fibroblasts and endothelial cells. *Proceedings of the National Academy of Sciences*. 2001;98(2):646-651. doi:doi:10.1073/pnas.98.2.646

44. Olsen CJ, Moreira J, Lukanidin EM, Ambartsumian NS. Human mammary fibroblasts stimulate invasion of breast cancer cells in a three-dimensional culture and increase stroma development in mouse xenografts. *BMC Cancer*. Aug 19 2010;10:444. doi:10.1186/1471-2407-10-444

45. Sadras F, Stewart TA, Robitaille M, et al. Altered Calcium Influx Pathways in Cancer-Associated Fibroblasts. *Biomedicines*. Jun 16 2021;9(6)doi:10.3390/biomedicines9060680

46. Kapalczynska M, Kolenda T, Przybyla W, et al. 2D and 3D cell cultures - a comparison of different types of cancer cell cultures. *Arch Med Sci*. Jun 2018;14(4):910-919. doi:10.5114/aoms.2016.63743

47. Abuwatfa WH, Pitt WG, Husseini GA. Scaffold-based 3D cell culture models in cancer research. *J Biomed Sci*. Jan 14 2024;31(1):7. doi:10.1186/s12929-024-00994-y

48. Breslin S, O'Driscoll L. Three-dimensional cell culture: the missing link in drug discovery. *Drug Discov Today*. Mar 2013;18(5-6):240-9. doi:10.1016/j.drudis.2012.10.003

49. Frohlich E. The Variety of 3D Breast Cancer Models for the Study of Tumor Physiology and Drug Screening. *Int J Mol Sci*. Apr 12 2023;24(8)doi:10.3390/ijms24087116

50. Langhans SA. Three-Dimensional in Vitro Cell Culture Models in Drug Discovery and Drug Repositioning. *Front Pharmacol*. 2018;9:6. doi:10.3389/fphar.2018.00006

51. Edmondson R, Broglie JJ, Adcock AF, Yang L. Three-dimensional cell culture systems and their applications in drug discovery and cell-based biosensors. *Assay Drug Dev Technol*. May 2014;12(4):207-18. doi:10.1089/adt.2014.573

52. Costa EC, Moreira AF, de Melo-Diogo D, Gaspar VM, Carvalho MP, Correia IJ. 3D tumor spheroids: an overview on the tools and techniques used for their analysis. *Biotechnol Adv*. Dec 2016;34(8):1427-1441. doi:10.1016/j.biotechadv.2016.11.002

53. Pinto B, Henriques AC, Silva PMA, Bousbaa H. Three-Dimensional Spheroids as In Vitro Preclinical Models for Cancer Research. *Pharmaceutics*. Dec 6 2020;12(12)doi:10.3390/pharmaceutics12121186

54. Antoni D, Burckel H, Josset E, Noel G. Three-dimensional cell culture: a breakthrough in vivo. *Int J Mol Sci*. Mar 11 2015;16(3):5517-27. doi:10.3390/ijms16035517

55. Habanjar O, Diab-Assaf M, Caldefie-Chezet F, Delort L. 3D Cell Culture Systems: Tumor Application, Advantages, and Disadvantages. *Int J Mol Sci*. Nov 11 2021;22(22)doi:10.3390/ijms222212200

56. Weiswald LB, Bellet D, Dangles-Marie V. Spherical cancer models in tumor biology. *Neoplasia*. Jan 2015;17(1):1-15. doi:10.1016/j.neo.2014.12.004

57. Yousefnia S, Ghaedi K, Seyed Forootan F, Nasr Esfahani MH. Characterization of the stemness potency of mammospheres isolated from the breast cancer cell lines. *Tumour Biol*. Aug 2019;41(8):1010428319869101. doi:10.1177/1010428319869101

58. Imamura Y, Mukohara T, Shimono Y, et al. Comparison of 2D- and 3D-culture models as drug-testing platforms in breast cancer. *Oncol Rep*. Apr 2015;33(4):1837-43. doi:10.3892/or.2015.3767

59. Thoma CR, Zimmermann M, Agarkova I, Kelm JM, Krek W. 3D cell culture systems modeling tumor growth determinants in cancer target discovery. *Adv Drug Deliv Rev*. Apr 2014;69-70:29-41. doi:10.1016/j.addr.2014.03.001

60. Jensen C, Teng Y. Is It Time to Start Transitioning From 2D to 3D Cell Culture? *Front Mol Biosci*. 2020;7:33. doi:10.3389/fmolb.2020.00033

61. Billerhart M, Schönhofer M, Schueffl H, et al. CD47-targeted cancer immunogene therapy: Secreted SIRPα-Fc fusion protein eradicates tumors by macrophage and NK cell activation. *Molecular Therapy - Oncolytics*. 2021;23:192-204. doi:10.1016/j.omto.2021.09.005

62. Pei J, Panina SB, Kirienko NV. An Automated Differential Nuclear Staining Assay for Accurate Determination of Mitocan Cytotoxicity. *J Vis Exp*. May 12 2020;(159)doi:10.3791/61295

63. Assmann R. *Optimization of triple negative breast cancer spheroids*. 2025. https://doi.org/10.25365/thesis.79077

64. Froehlich K, Haeger J-D, Heger J, et al. Generation of Multicellular Breast Cancer Tumor Spheroids: Comparison of Different Protocols. *Journal of Mammary Gland Biology and Neoplasia*. 2016/12/01 2016;21(3):89-98. doi:10.1007/s10911-016-9359-2

65. Huang YL, Shiau C, Wu C, Segall JE, Wu M. The architecture of co-culture spheroids regulates tumor invasion within a 3D extracellular matrix. *Biophys Rev Lett*. Sep 2020;15(3):131-141. doi:10.1142/s1793048020500034

66. Mishriki S, Aithal S, Gupta T, Sahu RP, Geng F, Puri IK. Fibroblasts Accelerate Formation and Improve Reproducibility of 3D Cellular Structures Printed with Magnetic Assistance. *Research (Wash D C)*. 2020;2020:3970530. doi:10.34133/2020/3970530

67. Morán MdC, Cirisano F, Ferrari M. Superhydrophobicity Effects on Spheroid Formation, Structure, and Viability on Co-Culture Conditions. *Pharmaceuticals*. 2025;18(7):953.

68. Piwocka O, Sterzynska K, Malinska A, Suchorska WM, Kulcenty K. Development of tetraculture spheroids as a versatile 3D model for personalized breast cancer research. *Sci Rep*. Jul 28 2025;15(1):27449. doi:10.1038/s41598-025-12556-9

69. MedChemExpress. Basement Membrane Matrix GFR Product Information. Accessed 24.02.2026, https://www.medchemexpress.com/inhibitor-kit/meltrex-reduced-growth-factor-basement-membrane-matrix-phenol-red-free.html

70. Keller F. *Targeted 2D- and 3D-cell cultures reveal mechanistic effects of extracellular matrix and stromal cells on the metastatic niche formation and metabolism of cancer cells*. 2022.

71. Kleinman HK, McGarvey ML, Liotta LA, Robey PG, Tryggvason K, Martin GR. Isolation and characterization of type IV procollagen, laminin, and heparan sulfate proteoglycan from the EHS sarcoma. *Biochemistry*. 1982/11/01 1982;21(24):6188-6193. doi:10.1021/bi00267a025

72. Walzl A, Unger C, Kramer N, et al. The Resazurin Reduction Assay Can Distinguish Cytotoxic from Cytostatic Compounds in Spheroid Screening Assays. *J Biomol Screen*. Aug 2014;19(7):1047-59. doi:10.1177/1087057114532352

73. Mittler F, Obeid P, Rulina AV, Haguet V, Gidrol X, Balakirev MY. High-Content Monitoring of Drug Effects in a 3D Spheroid Model. *Front Oncol*. 2017;7:293. doi:10.3389/fonc.2017.00293

74. Badea MA, Balas M, Hermenean A, et al. Influence of Matrigel on Single- and Multiple-Spheroid Cultures in Breast Cancer Research. *SLAS Discov*. Jun 2019;24(5):563-578. doi:10.1177/2472555219834698

75. Raghavan S, Mehta P, Horst EN, Ward MR, Rowley KR, Mehta G. Comparative analysis of tumor spheroid generation techniques for differential in vitro drug toxicity. *Oncotarget*. Mar 29 2016;7(13):16948-61. doi:10.18632/oncotarget.7659

76. Cui X, Hartanto Y, Zhang H. Advances in multicellular spheroids formation. *J R Soc Interface*. Feb 2017;14(127)doi:10.1098/rsif.2016.0877

77. Vordermark D, Shibata T, Brown JM. Green fluorescent protein is a suitable reporter of tumor hypoxia despite an oxygen requirement for chromophore formation. *Neoplasia*. Nov-Dec 2001;3(6):527-34. doi:10.1038/sj.neo.7900192

78. Majety M, Pradel LP, Gies M, Ries CH. Fibroblasts Influence Survival and Therapeutic Response in a 3D Co-Culture Model. *PLoS One*. 2015;10(6):e0127948. doi:10.1371/journal.pone.0127948

79. Li Q, Chen C, Kapadia A, et al. 3D models of epithelial-mesenchymal transition in breast cancer metastasis: high-throughput screening assay development, validation, and pilot screen. *J Biomol Screen*. Feb 2011;16(2):141-54. doi:10.1177/1087057110392995

80. Bucki R, Iwamoto DV, Shi X, et al. Extracellular vimentin is sufficient to promote cell attachment, spreading, and motility by a mechanism involving N-acetyl glucosamine-containing structures. *J Biol Chem*. Aug 2023;299(8):104963. doi:10.1016/j.jbc.2023.104963

81. McInroy L, Määttä A. Down-regulation of vimentin expression inhibits carcinoma cell migration and adhesion. *Biochemical and Biophysical Research Communications*. 2007/08/17/ 2007;360(1):109-114. doi:https://doi.org/10.1016/j.bbrc.2007.06.036

82. Liu CY, Lin HH, Tang MJ, Wang YK. Vimentin contributes to epithelial-mesenchymal transition cancer cell mechanics by mediating cytoskeletal organization and focal adhesion maturation. *Oncotarget*. Jun 30 2015;6(18):15966-83. doi:10.18632/oncotarget.3862

83. Nurmik M, Ullmann P, Rodriguez F, Haan S, Letellier E. In search of definitions: Cancer-associated fibroblasts and their markers. *Int J Cancer*. Feb 15 2020;146(4):895-905. doi:10.1002/ijc.32193

84. Romano V, Ruocco MR, Carotenuto P, et al. Generation and Characterization of a Tumor Stromal Microenvironment and Analysis of Its Interplay with Breast Cancer Cells: An In Vitro Model to Study Breast Cancer-Associated Fibroblast Inactivation. *Int J Mol Sci*. Jun 20 2022;23(12)doi:10.3390/ijms23126875